University of Tennessee, Knoxville
TRACE: Tennessee Research and Creative Exchange

Doctoral Dissertations | Graduate School

12-2024

Complete Decay Spectroscopy of Chlorine Isotopes with the FRIB Decay Station Initiator

Ian C. Cox
icox2@vols.utk.edu

Follow this and additional works at: https://trace.tennessee.edu/utk_graddiss

 Part of the Nuclear Commons

Recommended Citation

Cox, Ian C., "Complete Decay Spectroscopy of Chlorine Isotopes with the FRIB Decay Station Initiator. " PhD diss., University of Tennessee, 2024.
https://trace.tennessee.edu/utk_graddiss/11344

This Dissertation is brought to you for free and open access by the Graduate School at TRACE: Tennessee Research and Creative Exchange. It has been accepted for inclusion in Doctoral Dissertations by an authorized administrator of TRACE: Tennessee Research and Creative Exchange. For more information, please contact trace@utk.edu.

To the Graduate Council:

I am submitting herewith a dissertation written by Ian C. Cox entitled "Complete Decay Spectroscopy of Chlorine Isotopes with the FRIB Decay Station Initiator." I have examined the final electronic copy of this dissertation for form and content and recommend that it be accepted in partial fulfillment of the requirements for the degree of Doctor of Philosophy, with a major in Physics.

Robert Grzywacz, Major Professor

We have read this dissertation and recommend its acceptance:

Thomas Papenbrock, Yuri Efremenko, Jason Hayward

Accepted for the Council:

Dixie L. Thompson

Vice Provost and Dean of the Graduate School

(Original signatures are on file with official student records.)

Complete Decay Spectroscopy of Chlorine Isotopes with the FRIB Decay Station Initiator

A Dissertation Presented for the

Doctor of Philosophy

Degree

The University of Tennessee, Knoxville

Ian C. Cox

December 2024

© by Ian C. Cox, 2024
All Rights Reserved.

"To improve is to change, so to be perfect is to have changed often" - Winston Churchill

Acknowledgements

I would first like to thank my advisor, Dr. Robert Grzywacz, for the enormous amount of support and guidance before, during, and after my graduate studies. Due to this, I have been able to quickly broaden my grasp of radioactive decay through multiple isotope analyses, even if they were not a part of my original research focus. Secondly, I would like to extend my appreciation for my research colleagues both at and outside of the University of Tennessee, Knoxville, specifically Dr. Zhengyu Xu for his mentorship and ability to withstand my never-ending supply of questions. Next, I would like to thank my family for instilling in me a good work ethic at a young age which has allowed me to conquer the difficult task of completing a graduate program. Most importantly, I would like to thank my wife Delaney for her immeasurable support and patience throughout my entire graduate career, even with long nights of work and numerous extended trips to Michigan and Japan for experiments.

Abstract

The main scientific goal of Radioactive ion Beam Facilities is to enable studies of exotic nuclei and thus quantify changes in nuclear structure in the short-lived nuclei with unusual numbers of protons and neutrons. Advanced detection systems are implemented to maximize detection efficiency and energy resolution to capitalize on the development of exotic isotope beams. The US Facility for Rare Isotope Beams (FRIB, East Lansing, Michigan) became operational in 2022. The first experiments at FRIB used the FRIB Decay Station Initiator (FDSi), a multi-detector system developed for measurements of exotic radioactive nuclei. FDSI combines advanced individual detectors from multiple institutions to comprehensively study decay observables.

This work is based on results from one of the earliest FDSi experiments, which enabled a complete decay spectroscopic study of the β decay of chlorine isotopes with neutron number ≈ 28. These nuclei are in a transitional region between the spherical Calcium-48 and the deformed Silicon-42, known to be located in the second island of inversion. Complementary to the previous reaction measurements, the experimental studies of Chlorine decay provide a benchmark for theoretical models as one increases the neutron-to-proton ratio.

Table of Contents

List of Tables

List of Figures

Chapter 1

Introduction

Nearly the entire mass of the atom is located in the nucleus, consisting of protons and neutrons. Combinations of protons and neutrons create different nuclei, where the overwhelming majority of known nuclei undergo radioactive decay. The decay properties of all radioactive nuclei are dependent on interactions between nucleons. Critical questions, such as how elements heavier than iron were created and what happens in nuclear reactors after fission, are directly related to the decay properties of radioactive nuclei and thus how nucleons arrange themselves and interact in the nucleus. R-process nuclei and fission products are both known for their large neutron excess leading to the possibility of β^- decay followed by neutron emission if sufficiently neutron-rich, but the study of these nuclei is exceedingly difficult due to their short lifetimes and difficulty to synthesize in a laboratory. Yet still, the study of radioactive decays of those nuclei has progressed greatly due to the improved capabilities of radioactive ion (RI) beam facilities which have pushed the discovery limits of known nuclei providing insight into many nuclear and decay properties of nuclei along with the limits at which nuclei can be created. These new generation facilities include the Facility for Rare Isotope Beams (FRIB) at Michigan State University, the New Californium Rare Isotope Breeder Upgrade (nuCaribu) at the Argonne Tandem Linac Accelerator System (ATLAS), TRIUMF, Spiral-2 at GANIL, the ISOLDE Radioactive Ion Beam Facility at CERN, the Radioactive Ion Beam Factory (RIBF) at RIKEN, and the Facility for Antiproton and Ion Research (FAIR) at GSI, all of which are pushing to measure nuclei far from stability to the point where neutrons cannot be added or where

neutrons cannot be removed, known as the neutron and proton drip lines, respectively. Many of the facilities employ different methods for producing rare isotopes, but each has dedicated detector systems focused on radioactive decay spectroscopy. The FRIB Decay Station Initiator (FDSi), located at FRIB, combines detectors from numerous institutions across the United States to comprehensively measure exotic nuclei with high sensitivity [1].

Complete β-decay spectroscopy occurs when one can measure fundamental decay properties for a single nucleus, including the half-life, neutron branching ratio, and the β-decay strength distribution for a wide, continuous range of the entire β-decay window, Q_β. The FDSi aims to achieve that by utilizing two separate implantation locations and combining high-resolution instruments with total absorption spectroscopy, capable of energy calorimetry measurements. Individual transitions can be measured via semiconductor (high-purity germanium) or scintillator ($LaBr_3$) γ-ray detectors and neutron time-of-flight detectors in the first focal plane. In the second focal plane, total absorption spectroscopy utilizes a very high γ-ray efficiency to measure many different γ-ray transitions from each state, resulting in β-decay feeding intensity measurements with high precision [2].

When moving away from stability, the decay energy grows such that complete decay spectroscopy becomes an invaluable tool to probe nuclear structure properties in both the parent and daughter nuclei. The most fundamental property of β-decay, the half-life, is entirely dependent on the so-called β-decay strength distribution, where effects such as competition between allowed and forbidden transitions determine the transition rates. In very neutron-rich nuclei, the protons and neutrons begin to fill asymmetric single particle orbitals, impacting the β-decay strength distribution. For example, reduced population of the ground states in the so-called allowed decays. In consequence, delineating the region of allowed transitions becomes paramount for being able to accurately calculate the half-life and neutron branching ratio for a β-decaying nucleus.

This work will demonstrate the value of complete decay spectroscopy for neutron-rich nuclei, specifically by measuring the decay of chlorine isotopes. In doing so, the evolution from spherical to deformed nuclei can be tracked. This chapter will outline the relevant physics models that are being used, specifically, the nuclear shell model and how it is used to study the β decays of deformed nuclei (1.1) and the mechanism of β-delayed neutron

emission (1.2). Chapter 2 details the specific physics cases for the nuclei to be studied in this work, including the impact of shell evolution and the effects of increased deformation when moving away from magic nuclei. A description of the previous results of investigated nuclei in the region will be provided. Chapter 3 elaborates on the FDSi experimental setup used, including all of the detector systems that were included. The analysis procedure is described in Chapter 4 for each FDSi detector used in the experiment, including the particle identification , ion-implantation, γ, and neutron detectors. Experimental results are presented in Chapter 5 for chlorine isotopes, along with a discussion of the results and comparisons to shell model calculations presented in Chapter 6.

1.1 Emergence of the shell effects in atomic nuclei

Similar to electrons in atoms, it was found that specific numbers of nucleons generate local discontinuities in nuclear binding energies at specific proton and neutron numbers. These numbers, first postulated by Elsasser, were coined as "magic" numbers, occurring at 2, 8, 20, 28, 50, 82, and 126 [3, 4]. One can implement a harmonic oscillator potential for nucleons to try to predict different excited states for the nucleons. Major shells, N, are then created on the basis $N = 2(n-1) + l$, where $n = 1, 2, 3, ...$ is the principal quantum number and $l = 0, 1, 2, 3, 4, ...$ is the orbital angular momentum quantum number [5, 6]. The number of degenerate protons (or neutrons) in an orbital would then be determined by $2(2l+1)$, replicating some smaller magic numbers, specifically 2, 8, and 20. Maria Goeppert Mayer, and independently Haxel, Jensen, and Suess, built upon this by adding a spin-orbit coupling term, $\vec{l} \cdot \vec{s}$, related to the spin quantum number $s = \pm 1/2$, reproducing gaps in the energy levels that replicate the magic numbers not initially seen from just the harmonic oscillator potential[7, 8]. Combining these terms, one has the total angular momentum, $j = l + s$. With this, the degeneracy of each state can then be found by, $d = 2j + 1$. A prime example of spin-orbit splitting creating magic nuclei is ^{48}Ca, which has $Z = 20$ and $N = 28$. The nucleus is nearly stable, with a half-life of 2.5×10^{19} years [9], and is one of the lightest doubly-magic nuclei resulting from spin-orbit splitting. Figure 1.1 shows the consequences of the spin-orbit splitting, with a large spacing between the $0f_{7/2}$ and $1p_{3/2}$ orbitals known

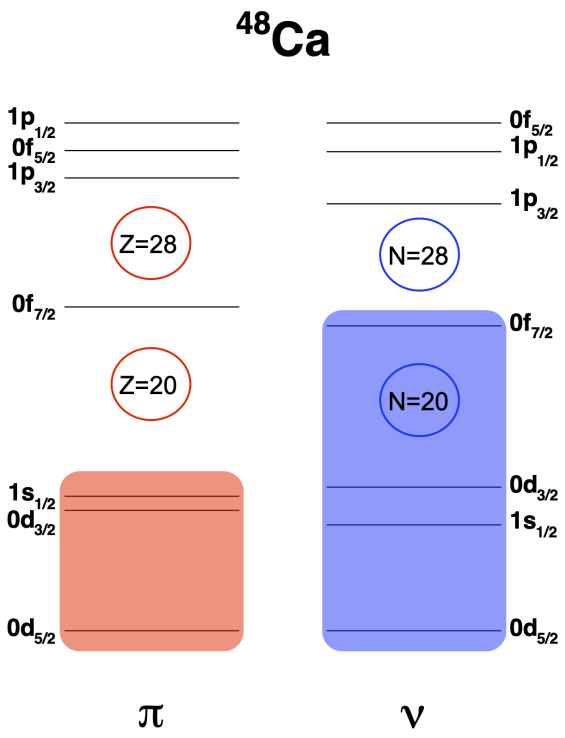

Figure 1.1: Orbitals for ^{48}Ca, where the protons (π) fill up the *sd*-shell shown as the red block consisting of the $d_{5/2}$, $d_{3/2}$, and $s_{1/2}$ orbitals and the neutrons (ν) occupy up to the $f_{7/2}$ orbital, shown as the blue block on the right.

as the $N = 28$ shell gap. The separation between the $f_{7/2}$ orbital and the $d_{3/2}$ or $s_{1/2}$ orbitals forms the $Z = 20$ shell gap and is a result of using the Woods-Saxon potential and spin-orbit interaction for nucleons. Magic nuclei, and those nearby, have a simple structure; therefore they make the ideal cases for testing theoretical models.

The classic shell model assumed that nuclei are spherical, but it was observed that straying further from the magic numbers allows for nuclei to become deformed. Taking a different approach, A. Bohr, B. Mottelson, and later S. Nilsson aimed to describe the rotational aspects of nuclei, including how nucleons can act collectively, which can, for example, shorten the lifetimes of excited states [10]. This led to the formulation of the deformed shell model, enabling calculations of single particle energies in deformed potentials with cylindrical symmetry for certain nuclei [11]. All nuclei are described by a deformation parameter, δ described by Equation 1.1, such that increased deformation

can cause nuclear vibrations specific to symmetry axes, given as $\omega_\perp$ and ω_z are oscillator frequencies perpendicular to and along the z-axis, respectively, and ω_0 is the frequency along the axis of symmetry [11]. From this, $\delta > 0$ represents prolate deformations, and $\delta < 0$ represents oblate deformations.

$$\delta = \frac{\omega_\perp - \omega_z}{\omega_0} \tag{1.1}$$

For the deformed shell model states, the degeneracy due to angular momentum, l, changes into degeneracy based on the projection of the angular momentum onto the z-axis, m_l [11]. In this formalism, a $d_{5/2}$ level, which can be occupied by 6 nucleons, would split into 3 different states with spins $I = 1/2, 3/2$, or $5/2$. Depending on the deformation, oblate or prolate, the energy of these states can switch, where for oblate nuclei the high-spin states are at lower excitation energies, while the opposite is true for prolate deformations. An example of this effect can be seen in Figure 1.2, not only for $d_{5/2}$ orbitals but other nearby levels as well. In the figure, gaps in energy levels lower, and for sufficiently deformed nuclei, become nonexistent, eliminating the magicity of that particular shell closure. For large deformations, new gaps form between energy levels, creating subshell closures or new magic numbers [12, 13, 14].

The quadrupole deformation parameter is reported as β_2. The shape of nuclear ground-state expressed in a spherical-harmonics expansion is shown in Equation 1.2[15]. In the equation, Y_l^m is the spherical harmonics, and $r(\theta, \phi)$ is the radius vector.

$$\beta_{lm} = \sqrt{4\pi}\frac{\int r(\theta,\phi) Y_l^m(\theta,\phi) d\Omega}{\int r(\theta,\phi) Y_0^0(\theta,\phi) d\Omega} \tag{1.2}$$

While deformed nuclei are thought to prefer cylindrical shapes, such as oblate and prolate, triaxial deformation can also occur. In triaxial deformation, the ellipsoidal deformation parameter and the non-axiality angle, β and γ, respectively, are used. In both representations of the deformation, larger β values indicate more deformed nuclei, but when γ approaches $60°$, then the nucleus is oblate, whereas when $\gamma \approx 0°$ the nucleus is prolate, and in-between the nucleus is considered to be triaxial. If γ is not reported, then the sign of β_2 is used to determine the shape, just like with δ.

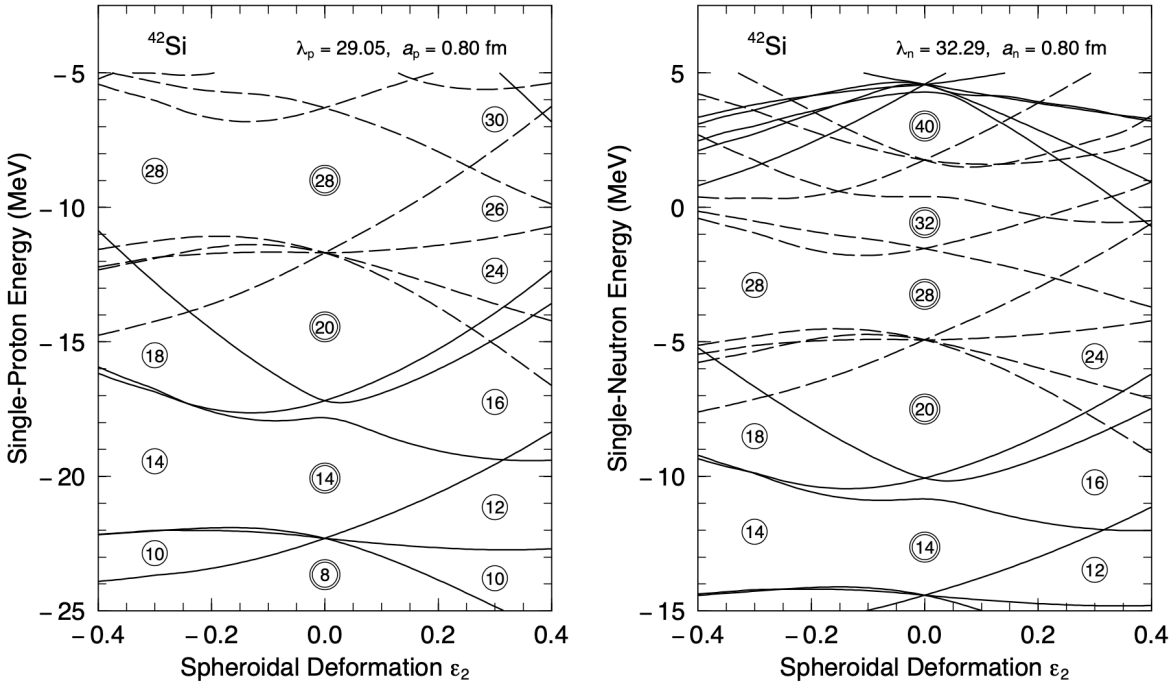

Figure 1.2: An example of Nilsson diagrams for protons and neutrons for ^{42}Si, from Ref. [15].

Electromagnetic transitions can connect excited states within a nucleus by either emitting a γ-ray or an electron [10]. Due to the electromagnetic multipole operators being spherical tensors, zero-coupled products can be formed that are rotationally invariant [16]. In the case of $E2$ electromagnetic transitions, the reduced $E2$ matrix elements within the electric quadrupole operator, $\mathcal{M}(\mathrm{E2})$, connect two states, I_r and I_s, $\langle I_s||\mathcal{M}(E2)||I_r\rangle = \langle I_s||\mathrm{E2}||I_r\rangle$ [17, 16]. The triaxial deformation parameters (β, γ) can then be calculated by obtaining the rotationally invariant products of the quadrupole operators [17, 16]. Equation 1.3 shows how to calculate the deformation parameters, where Z is the number of protons in the nucleus, r_i is the position of the i^{th} proton, and R is the nuclear radius in fm.

$$\begin{aligned}
\mathcal{M}(\mathrm{E}l, m) &= \sum_{i=1}^{Z} r_i^l Y_l^m(\theta_i, \phi_i) \\
Q^2 &= \sqrt{5}[\mathcal{M}(\mathrm{E2}) \times \mathcal{M}(\mathrm{E2})]_0 \\
Q^3 \cos 3\delta &= -\sqrt{\frac{35}{2}}[[\mathcal{M}(\mathrm{E2}) \times \mathcal{M}(\mathrm{E2})]_2 \times \mathcal{M}(\mathrm{E2})]_0 \\
q_0 &= \frac{3}{4\pi} Z R^2 \\
\beta &= \frac{\sqrt{Q^2}}{q_0} \\
\gamma &= \arccos(Q^3 \cos 3\delta) \frac{180^\circ}{3\pi}
\end{aligned} \tag{1.3}$$

1.2 β Decay

The most common form of decay for unstable nuclei is β decay, which was first discovered by Ernest Rutherford in 1899 [18]. Yet further development of β-decay theory would not come until 1934, when Enrico Fermi introduced a four-fermion interaction, including the postulate of the existence of the neutrino [19]. On the neutron-rich side of the chart of nuclides, Figure 1.3, β^- decay is the dominant decay. Historically, the Fermi model postulated the interaction to occur at a point. Later within the Standard Model, the weak interactions, such as in β-decays, are explained as being mediated by intermediate vector bosons [20], specifically the $W^\pm$ and Z^0 bosons with masses 80.4 GeV and 91.2 GeV, respectively. Constrained by the uncertainty principle, the heavy bosons make the interaction distance very small, $\approx 10^{-16}$ cm [20], justifying a point-like approximation for the transition. In β^-

decay, the W^- boson is used to transform an up quark into a down quark, while emitting an election (β particle) and an anti-neutrino. On the scale of nuclei, this means turning a neutron into a proton with the same byproducts. For a nucleus with mass A, protons Z, and neutrons N, the transition would be,

$$A(N, Z) \rightarrow A(N - 1, Z + 1) + e^- + \overline{\nu_e} \tag{1.4}$$

Here $\overline{\nu_e}$ is the electron anti-neutrino, conserving energy, spin, and lepton number in the decay. The energy of the decay is described as Q_β, and can be calculated as the mass difference between the two involved nuclei,

$$Q_{\beta^-} = [M(Z, N) - M(Z + 1, N - 1)]c^2 \tag{1.5}$$

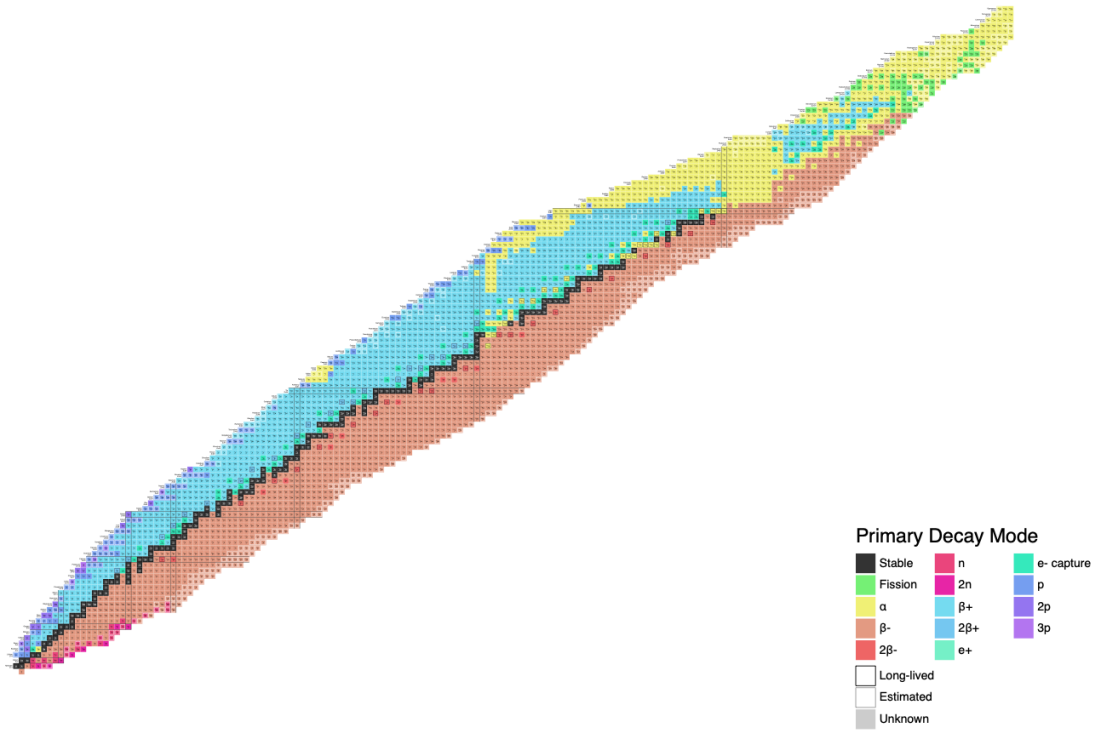

Figure 1.3: The chart of nuclides showing decay mode, with most neutron rich nuclei decaying via β^- decay [21].

1.2.1 Weak Interaction Transitions

In weak interactions, the two most probable transitions are Fermi and Gamow-Teller (GT), forming the so-called *allowed* decays. The Fermi operator is given as,

$$F^{(\pm)} = \sum_a \tau_{\pm,a}, \quad \tau_- = \begin{pmatrix} 0 & 0 \\ 1 & 0 \end{pmatrix} \text{ and } \tau_+ = \begin{pmatrix} 0 & 1 \\ 0 & 0 \end{pmatrix} \tag{1.6}$$

and the Gamow-Teller operator is,

$$(GT)_i^{(\pm)} = \sum_a \sigma_{i,a}\tau_{\pm,a}. \tag{1.7}$$

Where τ is the isospin operator and σ is the Pauli spin operators. Allowed β-decays are characterized by the emission of $l = 0$ leptons relative to the nucleus [22]. Fermi transitions are defined by having no change in the angular momentum, whereas GT transitions can have a spin change of $\Delta j = 0, \pm 1$, except for $J = 0 \rightarrow J = 0$ transitions that would violate angular momentum conservation rules[20]. Decays with leptons emitted with $l > 0$ are classified as forbidden. First forbidden (FF) decays occur with an angular momentum change of $L = 1$, then $L = 2$ for second forbidden decays, etc. For odd forbidden decays, $L = 1, 3, ...$, there is also parity change, $\Delta\pi = 1$ [20].

The total decay half-life can be given as a sum of all partial half-lives in a decay,

$$\frac{1}{t_{1/2}} = \sum_k \frac{1}{t_{1/2}^{(k)}}. \tag{1.8}$$

Where each partial half-life represents the transition from an initial state, i, in the parent nucleus to the final state, f, in the daughter nucleus, and can be experimentally measured through the β-decay feeding intensity I_β to a particular state,

$$t_{1/2}^{(k)} = \frac{t_{1/2}}{I_\beta^{(k)}}. \tag{1.9}$$

The partial half-life is then related to the β-decay strength, S_β,

$$S_\beta = \frac{1}{f t_{1/2}^{(k)}} \approx \frac{\overline{d\sum_j |M_\beta(E_j)|^2}}{dE} D^{-1}\mathrm{s}^{-1}\mathrm{MeV}^{-1}. \tag{1.10}$$

Here, $M_\beta(E_j)$ represents the allowed and forbidden β matrix elements near the final energy E of the daughter nucleus [23], $D = 6163.4 \pm 3.8$ s is the vector coupling constant, and f is the Fermi integral [22, 19] and can be written for allowed transitions as,

$$f = \int_1^{E_0} F(Z,\varepsilon)\sqrt{\varepsilon^2-1}\varepsilon(E_0-\varepsilon)^2 d\varepsilon, \quad \varepsilon = \frac{E_e}{m_e c^2}, \quad E_0 = \frac{E_i - E_f}{m_e c^2} \tag{1.11}$$

E_e is the total energy of the emitted lepton, E_i and E_f are the energies of the initial and final nuclear states, respectively. Lastly, the total half-life can be calculated using equation 1.12 [24]. Where the axial-vector coupling constant $g_A = 1.26$, vector coupling constant $g_V = 1$, and E_i is the β decay transition energy. Lastly, γ is the width of individual excitation and κ is related to the forbiddenness of the decay, such that $\langle\kappa_{J=0,1}\rangle = 1$ for GT and non-unique F decays and $\langle\kappa_{J=2}\rangle = f_1/f$ for unique FF decays and f_1 is calculated as in Ref. [22] Equation 7.160.

$$\frac{1}{t_{1/2}} = D^{-1}\left(\frac{g_A}{g_V}\right)^2 \int_0^{Q_\beta} f(Z+1, E_i) \sum_n \langle\kappa_J\rangle S(E_i,\gamma) dE_i \tag{1.12}$$

The β matrix elements allow for a direct connection between the decay strength distribution and the initial parent state and final daughter states. Thus, the selective nature of GT transitions allow for a unique probe of nuclear wavefunctions using the β-decay strength distribution.

1.2.2 β-Delayed Neutron Emission

In exotic neutron-rich nuclei, large asymmetries in the neutron-to-proton ratio are followed by large Q_β windows and a reduction of the neutron separation energy, S_n. Following β^- decay, delayed neutron emission can become energetically available when the resulting excited state lies above the neutron separation energy. The probability of neutron emission, P_n, is given in Equation 1.13 from [24], with B_n being the neutron separation, S being the strength

function, and $P_{if}(j^{\pi}_{i,f}, E_n)$ being the neutron emission probability between two states.

$$P_n = t_{1/2} D^{-1} (\frac{g_A}{g_V})^2 \int_{B_n(Z+1)}^{Q_\beta} dE_i f(Z+1, E_i) \sum_n \langle \kappa_J \rangle S(E_i, \gamma) P_{if}(j^{\pi}_{i,f}, E_n) \tag{1.13}$$

When the neutron separation energy is very large, there are fewer neutron unbound states for the β-decay to feed, leading to a lower probability of neutron emission. In the opposite case, when the neutron separation energy is very small, there is a possibility to feed states in the daughter which are above the neutron separation energy of the granddaughter, leading to the possibility of two-neutron emission. It is predicted that as one extends farther from stable nuclei, 3 and 4 neutron emission becomes possible. Eventually, one would reach the point where the neutron separation energy is so low that the nucleus is not bound. This is known as the neutron drip-line and is the limit of neutron-rich nuclei which can be studied. Figure 1.4, shows a general schematic for the β^- decay of a very neutron-rich nucleus. Due to various factors, such as selection rules and level density, a neutron unbound state in the emitter has the ability to emit a γ-ray, leading to neutron-γ competition. Also, for β-delayed emission of two neutrons, the deexcitation of high lying two neutron unbound states can proceed via the emission of one or two neutrons. These types of competition are generally described well by the statistical model [25], and are not the focus of this work.

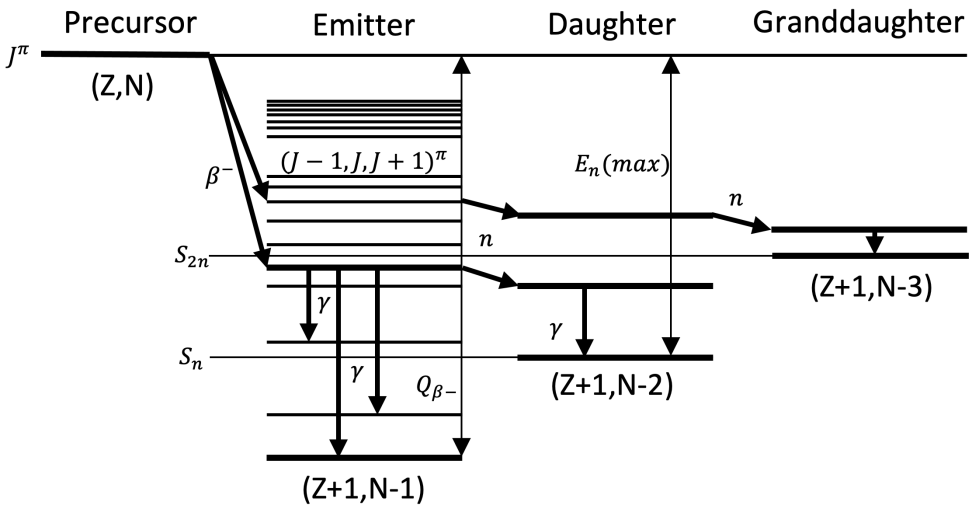

Figure 1.4: Schematic of β-delayed neutron emission, with the possibility of 2 neutron emission, with S_n being the 1 neutron separation energy and S_{2n} being the two neutron separation energy. Q_{β^-} represents the entire decay window for the precursor, which transitions to states with $(J-1, J, J+1)^\pi$ in a Gamow-Teller transition.

Chapter 2

Motivation For Studying Chlorine Decays

New heavy-ion fragmentation facilities, such as FRIB at Michigan State University, FAIR at GSI, and RIBF at RIKEN, have been able to produce very exotic nuclei. Robust models are needed to be able to predict the behavior of nuclei near the drip lines, created in stellar evolution, and created during fission. Accurate models are needed to understand the origin of the universe and how to safely control nuclear reactors. This work studies neutron-rich nuclei in a transitional region from spherical nuclei to deformed nuclei, while removing protons for nuclei with 28 neutrons. Specifically, the chlorine isotopes, with ^{45}Cl shown as the green star in Figure 2.1, can provide insight into how nuclear structure changes when nuclei become more deformed as they are situated equidistant from the spherical ^{48}Ca and the deformed ^{42}Si.

The region around ^{42}Si is called the "second island of inversion," based on the observation of $3/2^-$ ground states attributed to the occupation of neutrons in the $1p_{3/2}$ orbital occurring at a lower energy than the expected $7/2^-$ states from the $0f_{7/2}$ orbital neutrons [26]. Thus, the original orbital picture determined at ^{48}Ca for spherical nuclei, shown in Figure 1.1, is inverted for the $p_{3/2}$ and $f_{7/2}$ orbitals in ^{42}Si. Islands of Inversion and how they impact nuclear shell structure are discussed more in Section 2.1. Along with the structure changes for neutrons below ^{48}Ca, there are also changes in the proton orbitals when filling the neutron $f_{7/2}$ orbital between $N = 20$ and $N = 28$ nuclei. Changes in the proton shell structure

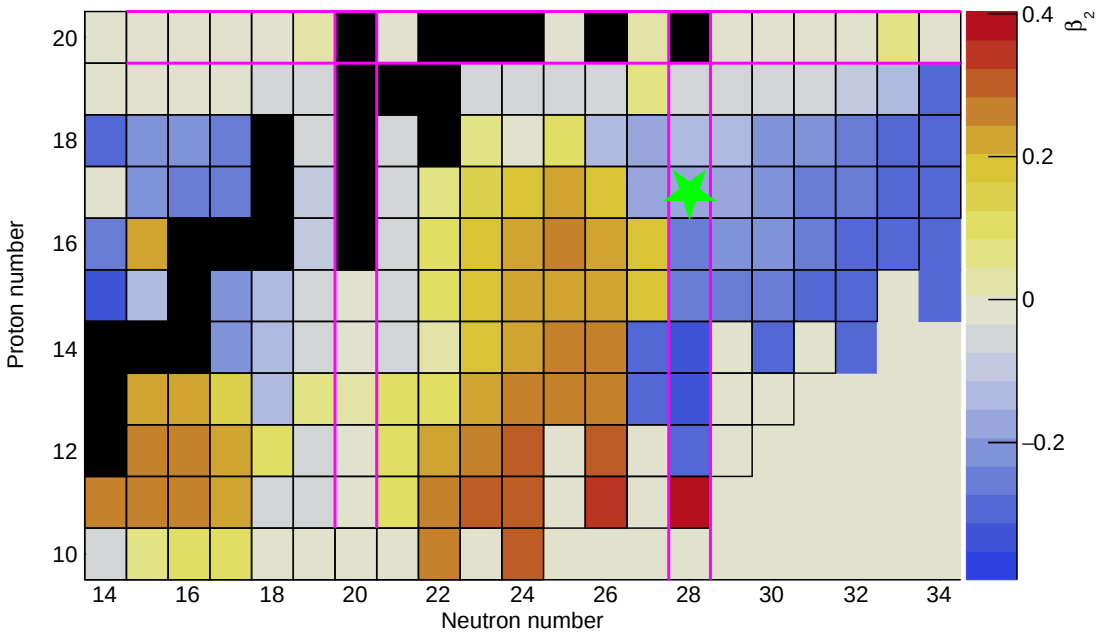

Figure 2.1: The predicted deformation, β_2, for nuclei with $Z \leq 20$ according to Finite Range Droplet Model (FRDM) calculations [15]. Here, the darker blue squares correspond to more oblate deformed nuclei, while red squares are prolate deformed nuclei. The green star represents the location of ^{45}Cl, and the pink lines highlight the traditional magic numbers of $Z, N = 20$ and $N = 28$.

resulting from the tensor force are discussed further in Section 2.2. To gain a full insight into what is happening in this region, the SDPF-MU shell model interaction [27, 28] is employed to calculate nuclear properties and allow for insight into the wavefunctions for specific nuclear states. This allows for a more complete understanding of how and why nuclear orbitals shift when changing the number of protons or neutrons for non-spherical nuclei while being able to make predictions for nuclear properties that have not yet been measured.

2.1 Islands of Inversion

When transitioning throughout the chart of nuclides, nucleon interactions affect the location of orbitals, leading to the changing or the disappearance of magic numbers. One early example of this follows the $N = 20$ shell gap, created in the nuclear potential and separating the $d_{3/2}$ neutrons from the $f_{7/2}$ neutrons [6], away from doubly-magic ^{40}Ca into lighter, more

neutron-rich isotones. Mass measurements of sodium isotopes showed an increase in S_{2n} near $N = 20$ [29], while β-decay measurements of sodium isotopes were able to identify a reduced 2^+ state in magnesium isotopes near $N = 20$ [30]. These nuclear properties helped identify the region of deformation near $N = 20$, which was unable to be captured using simple shell model calculations limited to the *sd* orbitals. Watt et al. were able to expand shell model calculations to include the $f_{7/2}$ orbitals to better predict the binding energies of neutron-rich nuclei [31]. Later, Poves and Retamosa [32], followed by Warburton, Becker, and Brown [33], were able to show that the $N = 20$ region of deformation was dominated by ground-state configurations with 2 neutrons in the $f_{7/2}$ orbital, leading to an inversion of the intruder, $2p - 2h$, configurations with $0p - 0h$ configurations, and thus the region was termed the *Island of Inversion*. Further work has been done to establish the evolution of neutron orbitals for $N = 20$ isotones [34, 35, 36].

A similar loss of magicity started to be seen along the $N = 28$ isotones below ^{48}Ca, with an isomer in ^{43}S resulting from the $3/2^-$ state being below the $7/2^-$ state [26], followed by a measured reduction of the neutron f orbital spin-orbit splitting [37]. The $N = 28$ shell gap was found to be collapsed in ^{42}Si, with the 2^+ state being at 770 keV [38]. Large Scale Shell Model (LSSM) calculations have since been employed to explain the reduction of the neutron $p_{3/2}$ orbital relative to the neutron $f_{7/2}$ orbital. For this, the SDPF-MU interaction was developed to use the monopole component of the V_{MU} interaction [39] for the *sd* and *pf* orbitals [27]. Utsuno et al. were then able to show that the inclusion of the tensor force is required to accurately reproduce ^{48}Ca spectroscopic factors, along with correct energy levels and $B(E2)$ values for neutron-rich sulfur and silicon isotopes [27]. Along with this, it was found that silicon isotopes can be susceptible to mixing between the $0d_{5/2}$ and $1s_{1/2}$ orbitals of the same magnetic moment, $m = \pm 1/2$ when increasing deformation [27]. Thus, the deformation along $N = 28$ is a result of mixing between the proton $0s_{1/2}$ and $1d_{5/2}$, and similarly neutron $0f_{7/2}$ and $1p_{3/2}$, orbitals causing degeneracy due to the tensor force [27]. This effect is called a Jahn-Teller-type effect since the deformation is due to the degeneracy of nuclear levels [40]. Using the formalism described earlier in Equation 1.3, the deformation for $N = 28$ isotones is calculated using the SDPF-MU interaction and shown in Figure 2.2. Overall, as the number of protons is reduced, the deformation β_2 increases

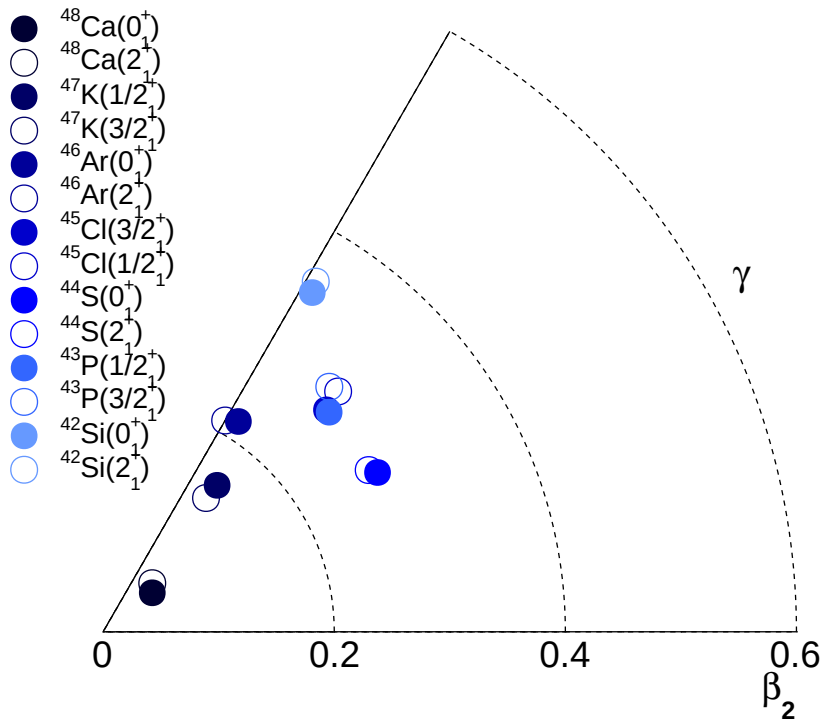

Figure 2.2: Calculated deformation parameters using the SDPF-MU interaction for $N = 28$ isotones from spherical ^{48}Ca to deformed ^{42}Si. The ground states are shown as the solid circles, while the first excited states are shown as the open circles.

to the point where ^{42}Si is deformed and strongly oblate, $\gamma \approx 60°$, as would be expected due to the protons occupying states of $m = \pm 5/2, \pm 3/2$ and neutrons occupying states of $m = \pm 7/2$. ^{44}S on the other hand, exhibits tri-axiality, $\gamma \approx 30°$, in agreement with the two regions of minima in the potential-energy surfaces for ^{44}S, where one is triaxial and the other is prolate deformed [27]. While the SDPF-MU interaction does well to describe some of the nuclear properties seen at the $N = 28$ island of inversion, more experimental data is needed to further probe the interaction.

2.2 Protons in the *sd* Shell

Calcium ($Z = 20$) is a special element, in that has two isotopes that are considered to be "doubly-magic," $^{40}Ca_{20}$ and $^{48}Ca_{28}$, yet the increase in the number of neutrons from $N = 20$ to $N = 28$ creates large differences in the shell structure for these two isotopes. One specific

difference is the change in separation between the $2s_{1/2}$ and $1d_{3/2}$ orbitals, which can be observed by measuring the corresponding $1/2^+$ and $3/2^+$ states in calcium and potassium ($Z = 19$) nuclei. Yntema and Satchler performed the ^{40}Ca(d,^{3} He)^{39}K reactions and identified positive parity states, attributed to holes in the $s_{1/2}$ or $d_{3/2}$ orbitals [41]. Following the (d,^{3} He) experiments, Bansal and French were able to identify the need for a term that captures the interaction between positive parity holes and the $f_{7/2}$ orbital [42]. Using this new term, they were able to calculate the excitation of $d_{3/2}$ hole states in titanium isotopes between $N = 20$ and $N = 28$ [42]. Later, experiments by Doll et al. [43] and Yntema [44] finished measuring the $1/2^+$ and $3/2^+$ states in odd-mass potassium isotopes from reactions on calcium isotopes. Using the known levels, Pellegrini was able to establish the trend of a decrease in spacing between the $1/2^+$ and $3/2^+$ levels, culminating in the $1/2^+$ state being lower than the $3/2^+$ state in ^{47}K [45].

Otsuka et al. progressed the theory further with the addition of a tensor force resulting from meson exchange processes, and coined the term shell evolution to be generalized for all nuclei [46]. As nucleons are added into an orbital, the single particle energy of other orbitals can then be affected. The effect, including the monopole effect, is termed the effective single-particle energy (ESPE) and represents mean effects from the other nucleons on a nucleon in a specified single-particle orbit [47]. Specifically, in the case of neutrons in an orbital l', with $j'_> = l' + 1/2$, an attraction is seen with protons of $j_< = l - 1/2$ and a repulsion of $j_>$ protons [46]. Applying this to calcium isotopes with $N > 20$, as done in Ref. [46], the monopole interaction between $d_{3/2}$ protons and $f_{7/2}$ neutrons is attractive, while $d_{5/2}$ protons are repelled by $f_{7/2}$ neutrons. Due to $s_{1/2}$ orbitals being unaffected by the tensor force [46], it is useful to plot the $d_{5/2}$ and $d_{3/2}$ orbitals relative to the $s_{1/2}$ orbital for a specific nucleus, as shown in Figure 2.3 for potassium (solid markers and lines) and chlorine (open markers and dashed lines) isotopes. As the $f_{7/2}$ orbital is filled, the $d_{3/2}$ orbital goes down and the $d_{5/2}$ orbital goes up. This in turn shrinks the gap between the $d_{3/2}$ orbital and the $s_{1/2}$ orbital to the point where at $N = 28$ they are degenerate. A good example of this is the measurement of the ground state of odd potassium ($Z = 19$) isotopes from $N = 20$ to $N = 28$, which is $3/2^+$ up until ^{47}K which instead has a $1/2^+$ ground state [48, 49]. Up until the $N = 28$ isotope, the $d_{3/2}$ proton hole dominates as the ground state, but, as predicted

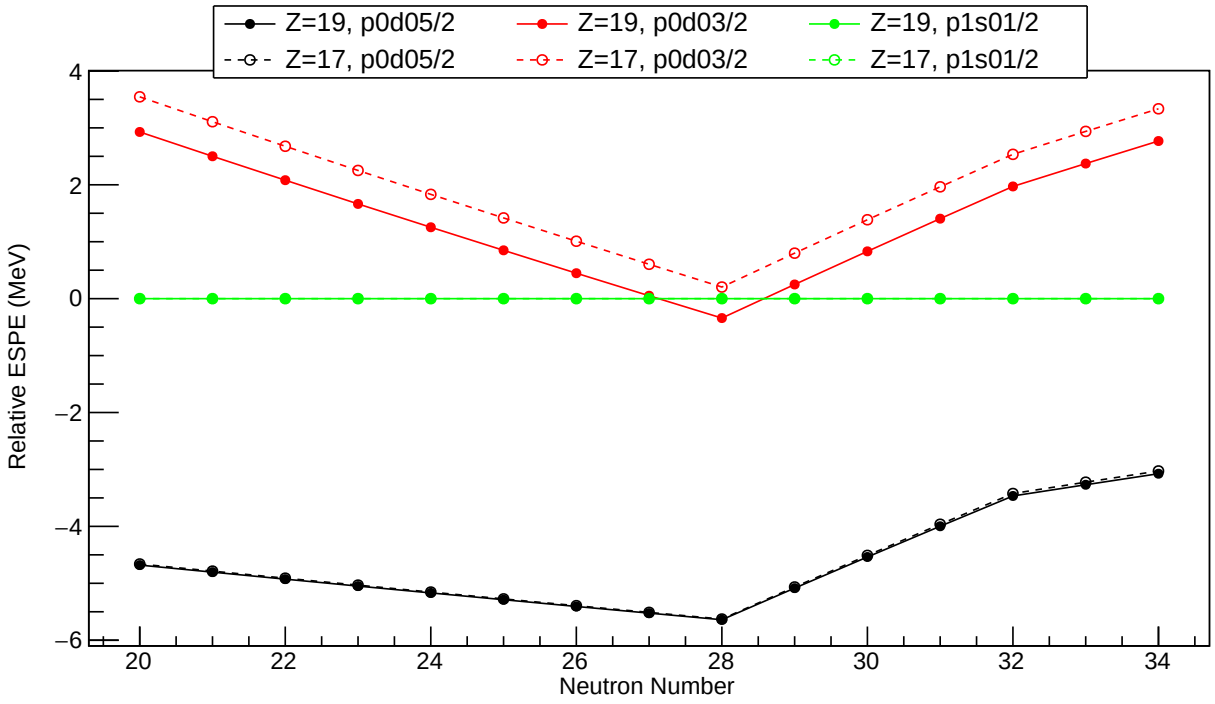

Figure 2.3: The effective single-particle energies (ESPE) for proton $d_{3/2}$ and $d_{5/2}$ orbitals in potassium (solid markers and lines) and chlorine (open markers and dashed lines) isotopes relative to their own proton $s_{1/2}$ orbitals.

by Otsuka, the $d_{3/2}$ and $s_{1/2}$ orbitals become degenerate to the point where $s_{1/2}$ holes are favored for the ground state of ^{47}K. The $1/2^+$ ground state persists for ^{49}K, but in ^{51}K the ground state reverts to $3/2^+$. When looking at the ESPEs from the SDPF-MU interaction, Figure 2.3, for the proton $d_{3/2}$ and $d_{5/2}$ orbitals relative to the $s_{1/2}$ orbital, there is a clear effect from the tensor force to the point that the $d_{3/2}$ orbital decreases below the $s_{1/2}$ orbital in potassium. While the trend agrees with the ground and excited state measurements of potassium isotopes, ESPEs do not directly correspond to the location of states in specific nuclei. Instead, entire collectivity must be included to properly calculate states. This is exemplified in the ESPEs for chlorine isotopes, Figure 2.3, where the $d_{3/2}$ orbitals do not quite reach the $s_{1/2}$ orbitals like the potassium isotopes. Still, the competition between the $3/2^+$ and $1/2^+$ states in chlorine isotopes highlights the impact of the tensor force. It can also be noted that relative to the $s_{1/2}$ proton orbitals, the $d_{5/2}$ remains unchanged when comparing potassium and chlorine isotopes due to the $d_{5/2}$ orbital being full for both $Z = 19$ and $Z = 17$, thus the same tensor force is applied to the $d_{5/2}$ orbital when filling the $f_{7/2}$

neutron orbital. The $d_{3/2}$ orbital, on the other hand, has fewer protons in chlorine than in potassium, resulting in a smaller tensor force predicted by the interaction.

Chlorine isotopes differ from potassium in that the ground state becomes $1/2^+$ earlier at $N = 24$ before reverting to $3/2^+$ at $N = 28$. This is shown by the recently measured decay of ^{45}Cl, where the β-decay feeding is better characterized by a $3/2^+$ ground state for ^{45}Cl compared to the prediction of $1/2^+$ [50]. The $3/2^+$ and $1/2^+$ states are nearly degenerate, with only 127 keV separation [51], yet predictions from the shell model are less accurate with the $3/2^+$ state being > 300 keV above the $1/2^+$ state, compared to 127 keV below it. Figure 2.4 shows the difference between the first $3/2^+$ and $1/2^+$ states in potassium (black) and chlorine (red) isotopes, with the experimental values from Refs. [52, 53, 54, 55, 56, 57, 51, 58, 59, 60, 61, 62] as the solid points and SDPF-MU predictions as the dashed lines. The overall experimental trend of inversion between the $3/2^+$ and $1/2^+$ states in both potassium and chlorine is replicated well by the SDPF-MU calculations, even though the location of the exact nucleus can be wrong. This is most notably seen in the gap between the measured and calculated difference between the $3/2^+$ and $1/2^+$ states in ^{45}Cl.

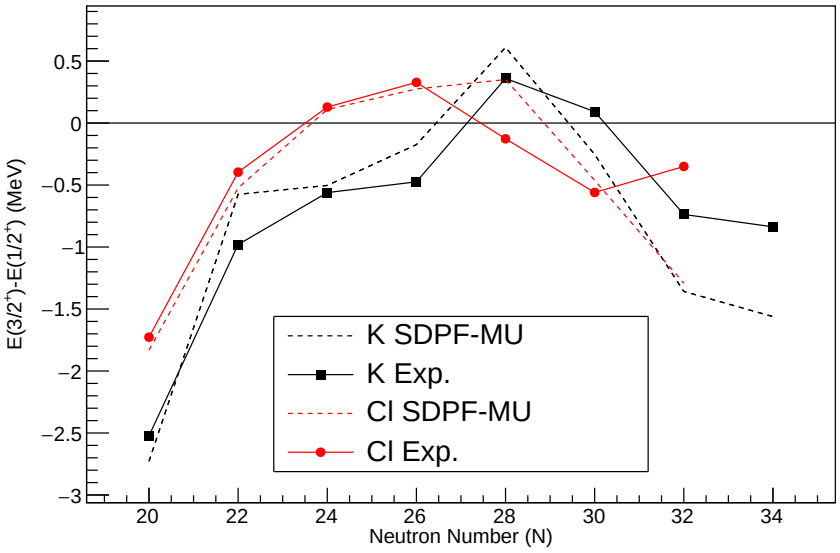

Figure 2.4: The difference between the first $3/2^+$ and $1/2^+$ states in potassium (black) and chlorine (red) isotopes with neutron numbers $20 \leq N \leq 34$. The dashed lines correspond to differences calculated by the SDPF-MU interaction.

2.3 Evolution of the $Z = 20$ Shell Gap

In the SDPF-MU interaction, the $N, Z = 20$ shell gaps are maintained or modified by the monopole interaction, V_{mu} [27]. SDPF-MU merges the USD interaction [63] for the *sd* shell to the GXPF1B interaction [64] for the *pf* shell. Spectroscopic factors for *sd* proton hole states in ^{47}K were used to demonstrate the need for the tensor force and benchmark the SDPF-MU interaction for proton shell gaps [27]. Yet as one moves south of calcium isotopes by removing protons, states which have protons in the *pf* shell are pushed higher up, thus becoming more difficult to access. The $Z = 20$ shell gap is thus more difficult to probe and less benchmarked in neutron-rich nuclei. β^- decay provides the unique ability to access these excited states, as *pf* neutrons can transition to *pf* protons via the Gamow-Teller transitions. By studying the high-lying excited states in the daughter nucleus, one can gain information about the location of the *pf* orbitals based on the decay strength to relevant states.

Theoretically, the evolution of the $Z = 20$ shell gap along $N = 28$ nuclei can be viewed through the ESPEs, similarly to what was done earlier for the $d_{3/2}$ and $s_{1/2}$ orbitals in the *sd* shell. Figure 2.5 shows the prediction for the $Z = 20$ shell gap when moving to more neutron-rich nuclei along $N = 28$, south of ^{48}Ca. As one moves to lower Z nuclei, the interplay between the $\pi d_{3/2}$ and $\pi s_{1/2}$ orbitals becomes increasingly volatile, shown by their crossings at $Z = 18$ and again below $Z = 15$. As mentioned earlier, this is largely due to the interactions between $d_{3/2}$ protons and $f_{7/2}$ neutrons. Higher up, the $\pi f_{7/2}$ orbitals remain relatively constant with respect to the *sd* orbitals, and thus the $Z = 20$ shell gap is constant, yet after the second crossing of the $\pi d_{3/2}$ and $\pi s_{1/2}$ orbitals below $Z = 15$, the shell gap shrinks before steadying. Furthermore, the highest lying $p_{1/2}$, $p_{3/2}$, and $f_{5/2}$ orbitals begin to fall relative to the *sd* before flattening at $Z = 16$. The true nature of the movement of these particles relative to each other remains unknown until more measurements can be performed.

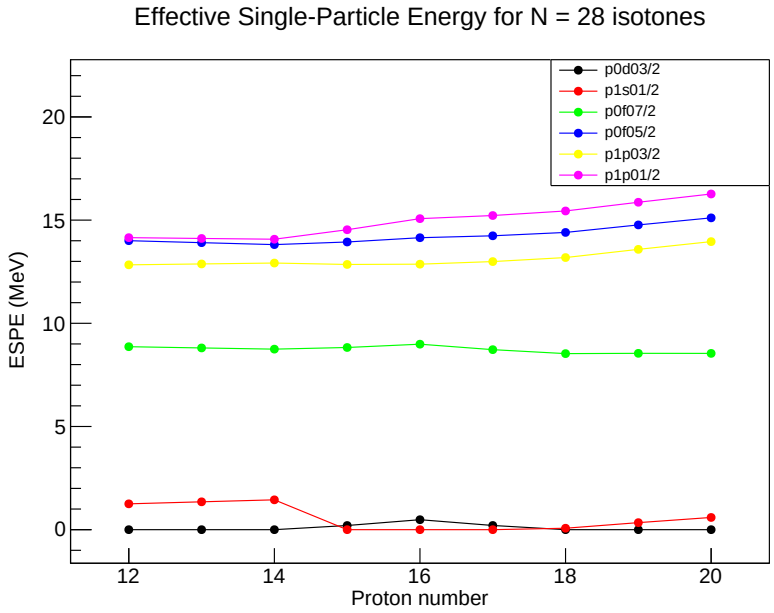

Figure 2.5: The ESPEs for proton pf orbitals with respect to the $s_{1/2}$ and $d_{3/2}$ orbitals for $N = 28$ nuclei with 20 or less protons, demonstrating the evolution of the $Z = 20$ shell gap below ^{48}Ca. All ESPEs here are relative to the lowest orbital in the $pf + s_{1/2} + d_{3/2}$ model space.

2.4 Previous Measurements of Argon Isotopes

The $N \approx 28$ argon isotopes have been studied extensively. First measurements of ^{44,45,46}Ar were performed by Sorlin et al. at GANIL, where β events of ^{44,45,46}Cl were measured in coincidence with neutrons to measure the half-lives and neutron branching ratios were extracted [65, 66]. The β-decay half-lives of ^{46,47}Cl were later reported by Grevy et al. [67, 68], with the first γ-rays in ^{44,45}Ar from the β-decays of ^{44,45}Cl, respectively, being reported in Refs. [67, 69] and the resulting levels shown in Figure 2.6. In their work, Mrázek et al. were able to identify states in ^{44}Ar up to 5.6 MeV populated in the β-decay of ^{44}Cl or the β-delayed neutron emission of ^{45}Cl, along with states in ^{45}Ar populated by the β-decay of ^{45}Cl up to 4.3 MeV and neutron bound states in ^{46}Ar populated by the β-decay of ^{46}Ar up to 8 MeV alongside 4 neutron unbound states as far as 2 MeV above the neutron separation energy [69]. These early β-decay measurements were crucial in being able to identify a large amount of excited states in argon isotopes which can be connected to the β-decaying ground states of chlorine isotopes. Around the same time, an experiment was performed

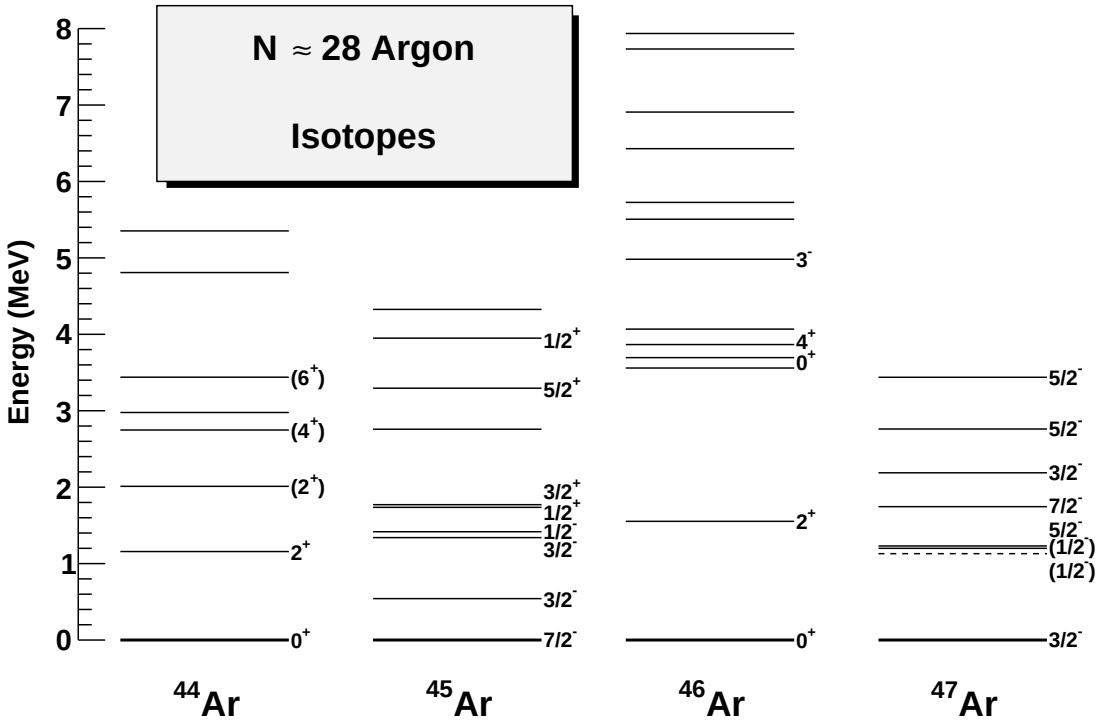

Figure 2.6: Known level schemes for argon isotopes with $N = 26 - 29$ measured across many experiments that are discussed in the text. The dashed line in ^{47}Ar represents the 1130 keV state observed by Gaudefroy, et al., but not by following experiments.

by Dombrádi et al. using fragmentation of ^{48}Ca to identify low-lying states in the argon nucleus, some of which agreed with states identified in β-decay and others which has not previously been identified [70]. States that had not been seen in β-decay were then able to be distinguished as having negative-parity and higher spins. Along with this, the 542 keV transition was identified as an E2 γ-transition connecting the $7/2^-$ ground state to the $3/2^-$ state with a lifetime of 340^{+320}_{-150} ps [70]. A higher energy neutron removal reaction from ^{46}Ar allowed for the confirmation of the spin-parties for the ground and first excited state to be $7/2^-$ and $3/2^-$, respectively [71]. Transfer reactions by Gaudefroy et al. and Lu et al. cross-examined ^{45}Ar through the ^{44}Ar$(d,p)^{45}$Ar and ^{46}Ar$(p,d)^{45}$Ar reactions, respectively. The (d,p) reaction was able to provide spectroscopic factors to negative parity states in ^{45}Ar and corresponding angular momentum values [72]. Along with this, shell model calculations for states in ^{45}Ar were found to be significantly more fragmented than corresponding negative parity hole states in ^{47}Ca [72]. The increase in particle-hole excitations as part of the

wave-functions for low-lying states helped to confirm the loss of the $N = 28$ magicity that was also seen using the ^{46}Ar$(d,p)^{47}$Ar reaction to probe single-particle energies above the $N = 28$ shell gap [37]. The (p,d) reaction, on the other hand, measured positive parity states in ^{45}Ar which were created through deeper neutron hole configurations [73]. Specifically, the degenerate 1.7 MeV states were identified to be positive parity states coming from neutron holes in the $s_{1/2}$ and $d_{3/2}$ orbitals, resulting in a $1/2^+$ and $3/2^+$ state with a significant spectroscopic factors [73]. The 3.3 MeV state was also seen in the reaction but did not have a large spectroscopic overlap with the ground state of ^{46}Ar, even though it was strongly fed in the β-decay measurements of ^{45}Cl. The β-decay of ^{45}Cl was most recently measured by Bhattacharya et al. [50], where a longer half-life was measured along with excited states agreeing with Mrazek. It was found that the most intense γ-ray transitions were a result of feeding to the 3.3 MeV state, leading to the deduction of ^{45}Cl having a $3/2^+$ ground state. This was validated using γ-ray intensities compared with shell model calculations using the FSU interaction [50].

After the β-decay studies of ^{46}Cl, states in ^{46}Ar were measured through various reaction techniques or Coulomb excitation, many of which were able to measure the first 2^+ excited state [74, 75, 76, 70, 77, 78]. During the early measurements, there was a discrepancy observed in the location of the first excited states, where some measurements placed it at 1570 keV [76, 70, 79], while others centered around 1552 keV [69, 74, 75, 77, 78, 80, 81, 82]. Since the majority of measurements, including decay studies, place the 2^+ state at 1552 keV, it will be referenced at the location throughout this work. Early measurements using Coloumb excitation were able to measure the reduced transition strength for the first excited state to be $B(E2\uparrow) = 193(39)e^2\text{fm}^4$ [75] and $B(E2\uparrow) = 218(31)e^2\text{fm}^4$ [78]. The lifetime of the 2^+ state in ^{46}Ar was deduced to be $t_{1/2} = 0.8^{+0.3}_{-0.4}$ ps, corresponding to a significantly larger $B(E2\uparrow) = 570^{+335}_{-160}e^2\text{fm}^4$ [80]. Calinescu et al. repeated the Coulomb excitation measurement and found agreement with the earlier data, $B(E2\uparrow) = 216(22)e^2\text{fm}^4$ [79]. Comparisons with various shell model calculations show a prediction of a larger $B(E2)$, in agreement with Mengoni, but disagreeing with the Coulomb excitation measurements. Nowak et al. relate the $B(E2)$ measurements to time-dependent Hartree-Fock-Bogoliubov calculations, which agree with the smaller $B(E2)$ values pointing towards moderate deformation and

collectivity in ^{46}Ar, which is expected in a semi-magic nucleus [82]. Discrepancies such as this highlight the shifting landscape transitioning away from a spherical region towards a deformed region. The measurement of a possible second 0^+ state in ^{46}Ar and comparison with DWBA calculations showed the excitations that are related to the deformation along $N = 28$ [82].

The first excited state measurements of ^{47}Ar were made by Gaudefroy, et al. at SPIRAL-GANIL, using the reaction $^{46}\mathrm{Ar}(d,p)^{47}\mathrm{Ar}$ [37]. This measurement found 4 states below the neutron separation energy and was able to assign angular momentum values to the states, 0 keV with $l = 1$, 1130 keV with $l = 1$, 1740 keV with $l = 3$, and 3335 keV with $l = 3$. Comparisons with shell model calculations led to the J^π assignments, $3/2^-, 1/2^-, 7/2^-$, and $5/2^-$, respectively [37]. The single neutron coupling to ^{46}Ar allowed for the calculation of single-particle energies for the neutron $p_{3/2}$, $p_{1/2}$, and $f_{5/2}$ orbitals, with the conclusion that the $N = 28$ shell gap is reduced by 330(90) keV compared with ^{49}Ca, due to a reduction in the spin-orbit splitting [37]. Shortly after this first measurement, ^{47}Ar was studied using deep inelastic scattering at GANIL, allowing for some different states to be populated [83]. Once again, the ground state was reported to be $3/2^-$ and the first excited state to be $1/2^-$, but the location of the first excited state is in slight disagreement. Instead, Bhattacharyya, et al. reported the first excited state to be at 1200 keV, with a second excited state at 1234 keV and $J^\pi = 5/2^-$ [83]. After this, the $7/2^-$ state is in agreement at 1747 keV and the last reported state at 2190 keV. Comparisons with shell model calculation illuminated a large fraction of particle-hole excitations across the $N = 28$ shell gap, corresponding to strong quadrupole interaction between protons in the sd shell and neutrons in the pf shell [83]. Winkler et al. continue the investigation of the $N = 28$ shell gap using the Coulomb excitation of ^{47}Ar and measuring the mixed M1-E2 γ-transition between the $5/2^-$ and $3/2^-$ states, yielding $B(E2; 3/2^- \rightarrow 5/2^-) = 137(17)e^2\mathrm{fm}^4$ [84]. Similar to ^{46}Ar, the $B(E2)$ strength value measured through Coulomb excitation is lower than the shell-model predictions [84]. The most recent measurement by Gade, et al., performed at the NSCL used both 1-neutron pickup of ^{46}Ar and 1-proton knockout of ^{48}K [85]. The two different production methods allowed for different states to be populated, where the neutron pickup strongly favored higher-lying $5/2^-$ states, shown by an increased spectroscopic factor to these

states. The proton knockout instead favored the lower-lying states and $3/2^-$ states, where both reactions were in good agreement with SDPF-MU and SDPF-U calculations [85].

Even though there have been many measurements of argon isotopes near $N = 28$, one unifying feature between all of the measurements is the lack of a β-feeding measurement. This work focuses on filling the deficiency using the combined FDSi two-focal plane system for both neutron-bound and unbound states. The results from the β-decay measurements can then be compared alongside the plethora of other measurements to provide a complete picture of the structure of argon isotopes near $N = 28$, and the shell evolution in the region. Figure 2.7 shows the available Gamow-Teller (green) and First Forbidden (purple) transitions for chlorine isotopes, connecting numerous different excited state configurations in an argon isotope to the parent chlorine nucleus. Specifically, the dark green lines differentiate the $pf \rightarrow pf$ GT transitions which would leave the residual argon isotope in a highly excited state, compared to the light green $sd \rightarrow sd$ GT transitions populating lower excited states. Due to a large fragmentation of the ground state wave functions for chlorine isotopes, it is expected that the $\nu p_{3/2}$ orbitals could contribute to the decay.

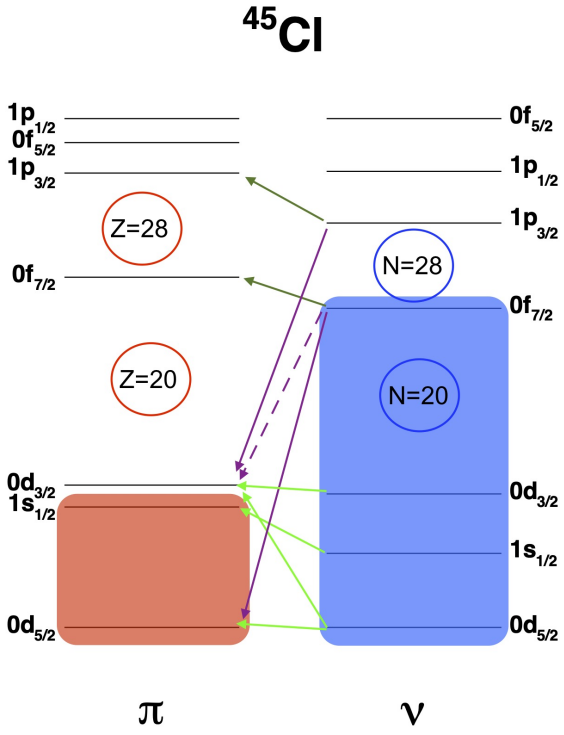

Figure 2.7: Schematic for available Gamow-Teller (green) and First Forbidden (purple) transitions for Chlorine isotopes. The lighter green lines demonstrate the possible $sd \rightarrow sd$ transitions, while the darker green lines demonstrate the $pf \rightarrow pf$ transitions. The dashed purple line shows the First Forbidden Unique transition for $\nu f_{7/2}$ to $\pi d_{3/2}$, which is rare.

Chapter 3

Experiment

3.1 FRIB

The Facility for Rare Isotope Beams (FRIB) is located at Michigan State University in East Lansing, Michigan. Previously the National Superconducting Cyclotron Laboratory (NSCL), FRIB improved upon the Coupled Cyclotron Facility with a new superconducting Radiofrequency Quadrupole (RFQ) linear accelerator (linac) for primary beams before colliding with a target [86]. Primary ion beams begin at the Electron Cyclotron Resonance (ECR) ion source, where the desired element is sent to the linac [86], shown on the right in Figure 3.1. The facility is designed to reach a maximum beam power of 400 kW on target, corresponding to beam energies $>$ 200 MeV/nucleon for primary beams ranging from H to ^{238}U allowing for the creation of thousands of new isotopes [86]. For experiment E21069, led by W. J. Ong, the primary beam energy for ^{82}Se was 165 and 215 MeV/nucleon for parts a and b, respectively. These increases in beam energy corresponded to an upgrade from 1 kW to 10 kW beam power between parts a and b.

Once accelerated by the linac, the beam of ions is delivered to the production target system, shown as yellow in the middle of Figure 3.1. The target consists of ^{9}Be disks, for a total thickness of 3.811 mm, rotating in a heat sink, where a hole in the heat sink allows for the beam to only interact with the target [88, 89]. After the projectile collides with the target, many different nuclei are created via the fragmentation process and transported through the multistage Advanced Rare Isotope Separator (ARIS) [89, 90]. Beginning with

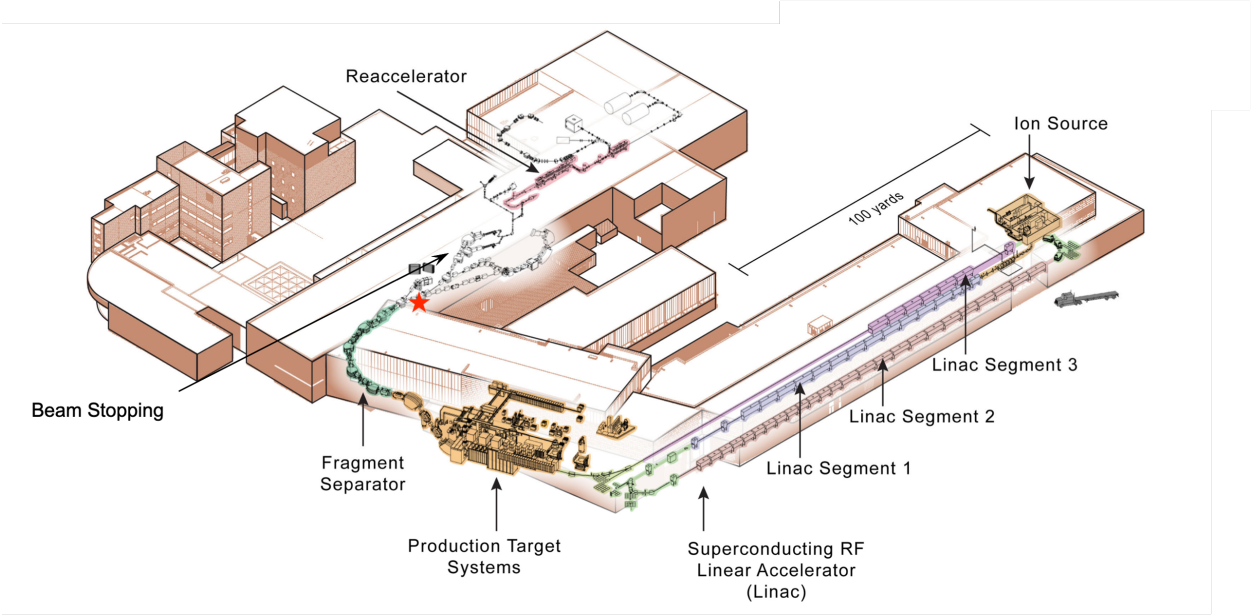

Figure 3.1: Schematic layout for the Facility for Rare Isotope Beams (FRIB) [87]. The red star indicates the location of FDSi for the first FRIB experiments.

the pre-separator, the beam is bent vertically for the first stage of purification, while imposing a momentum compression to better match the phase space acceptance properties of the second and third stages [90]. The separator selects radioactive isotopes based on their mass-to-charge ratio (A/Q) using various dipole (bending) magnets, wedges (to create dispersion), and quadrupole (refocusing) magnets. Mass selection slits are placed throughout the beamline for isotope purification. After the third ARIS stage, nuclei are transported to desired experimental stations or the reaccelerator (REA). The red star in Figure 3.1 shows the initial location of the FRIB Decay Station Initiator, situated in the transfer hall.

3.2 FDSi

The FRIB Decay Station Initiator (FDSi) uses a collection of detectors from various institutions around the United States. These detectors can then be situated in different arrangements around two different implantation locations for radioactive ions coming from ARIS. The implantation location closest to the separator consists of detectors that are used for discrete spectroscopy, such as germanium clover detectors for measuring gamma rays or scintillator time of flight detectors for measuring neutrons. The setup is shown in Figure 3.2,

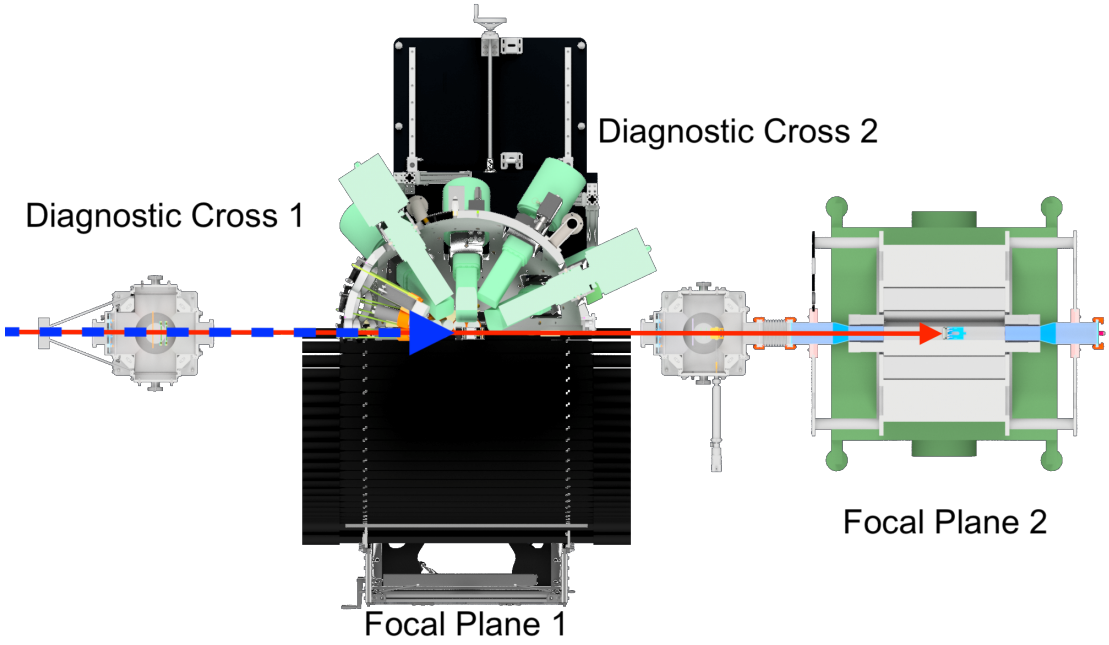

Figure 3.2: A sliced drawing of the FDSi setup, showing both the first focal and second focal planes, left and right respectively. Here the beam comes from the left to implant in the various focal planes as desired.

where the gamma array utilizes the top hemisphere of the implantation location, and the neutron array is situated in the bottom hemisphere of the first focal plane. Presently, the second focal plane consists solely of the total absorption spectrometer, with the future ability to alternatively use a ^{3}He neutron counter.

3.2.1 First Focal Plane

The cocktail beam arrives at FDSi from the left, as shown by the solid red and dashed blue lines, before reaching the first diagnostic cross which is used for particle identification, shown on the far left of Figure 3.2. Inside the cross, the beam traverses through a plastic scintillator followed by a rotating degrader and 2 silicon pin detectors. The plastic scintillator is used in conjunction with an upstream scintillator for time of flight measurements which are related to a nuclei's mass-to-charge ratio through the Lorentz force [91]. The subsequent pin detectors measure the energy loss of ions, which is proportional to the charge allowing for proper ion identification based on the Bethe-Bloch formula [91]. After the ions are identified in the first diagnostic cross they either implant into the first implant detector or continue to the second

focal plane which also has its own diagnostic cross also consisting of a plastic scintillator and 2 pin detectors.

Implant Detector

High-energy radioactive ion beams require an implant detector with a high effective-Z, to stop the nuclei and subsequently measure their decay [92]. Cerium doped Yttrium Orthosilicate, Y_2SO_5(Ce), was chosen for this experiment due to its effective-Z of 39, high density ($\rho = 4.5\text{g/cm}^3$), fast decay time ($t_d = 50 - 70\text{ns}$), and its non-hygroscopic nature, allowing it to be segmented [93]. The 5 mm thick YSO consisted of an array of 48x48 1x1mm segments, allowing for millimeter position resolution [94]. The light produced by the YSO scintillator is measured by a Hamamatsu H12700B-10 multi-anode photomultiplier (MAPMT) [95]. When using the MAPMT, the light being measured must be spread across multiple different anodes, allowing for the reconstruction of the initial location with high position resolution. Due to a finite MAPMT size, light can escape to the side of the MAPMT, remaining undetected, causing "edge effects" where the reconstructed location is miscalculated to be closer to the center than the real location of light generation. To counter edge effects, the YSO scintillator is coupled to a 24x24 segmented and tapered light guide, forcing the image from the scintillator away from the edges for more efficient light collection and thus avoiding edge effects. The entire detector assembly is wrapped in Teflon and electrical tape to ensure no outside light can reach the MAPMT. The MAPMT consists of an 8x8 array of PMTs, yielding a total of 64 anode signals along with 1 common dynode, used for timing. The 64 anode channels are sent to a Vertilon Anger-Logic board which uses a resistor network to reduce the 64 channels to 4 channels [96]. These 4 channels are then used to calculate the position of the event using Equation 3.1.

$$\begin{aligned} x_{\text{pos}} &= \frac{(V_1 + V_2) - (V_3 + V_4)}{\sum_{i=0}^{4} V_i} \\ y_{\text{pos}} &= \frac{(V_1 + V_4) - (V_3 + V_2)}{\sum_{i=0}^{4} V_i} \end{aligned} \tag{3.1}$$

Before being sent to the data acquisition (DAQ), the 5 signals from the implant detector are split into two branches, low and high gain. The low gain branch is used for ion implant

signals which occur with approximately 1 GeV of total energy deposited into the scintillator. Therefore, these signals are very large and either are deposited straight into the DAQ or are attenuated before the DAQ. Along with this, the DAQ channel is set to "low gain" for a voltage input range of 0-4 volts. The high gain branch, on the other hand, is amplified by a factor of 10 after being split and is then sent into a "high gain" channel in the DAQ. This high gain channel takes in signals from 0-1 volts. This creates a total factor of 40 between the high gain and low gain signals in the data analysis and is pivotal for being able to measure implantations and β-decays, which occur in the $\sim$ MeV range.

Around the YSO implant detector are 2 plastic veto detectors, one in front of the YSO (1 mm thick) and one in the rear of the implant detector box (5 mm thick). These detectors have custom silicon photomultiplier readouts coupled to the scintillators with Norland UV cure [97] on each side for possible left-right sensitivity. As shown in Figure 3.3, the front veto is used to help track incoming heavy ions, while also being able to measure, and if necessary reject, β-decays that leave the implant detector. The rear veto, on the other hand, is used solely to reject ions that travel through the implant detector and create a signal in the plastic so that the signals in the YSO are not mistaken for implantation events.

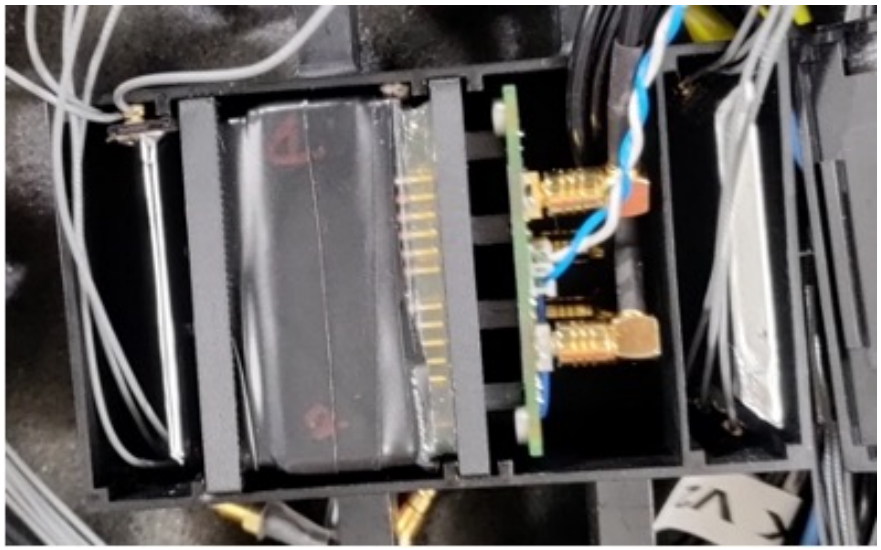

Figure 3.3: The implantation box, housing a 1 mm plastic front veto (left), followed by the YSO implant detector (middle), and a 5 mm plastic rear veto (right) at the end of the box.

Germanium Detectors

Semiconductor detectors, such as silicon detectors or high-purity germanium (HPGe) detectors create electron-hole pairs when electrons are excited across the band gap of the crystal due to charged particles or γ-radiation [98]. The electron and hole then traverse the remainder of the crystal via an electric field allowing for the electrical current to be measured [98]. Waiting for the electron-hole pairs to drift across the semiconductor material creates a slower response, but provides excellent energy resolution. Therefore, when discrete transitions between states in the same nucleus emit specific γ-rays, they can be precisely identified by HPGe clover detectors consisting of 4 individual crystals. For this experiment, 11 such clover detectors were employed and situated in the DEcay Germanium Array initiator (DEGAi) hemisphere around the first implant detector. Each clover consists of 4 HPGe crystals, yielding a total of 44 detectors. The array of clovers is shown as green detectors on the upper side of Focal Plane 1 in Figure 3.2.

$LaBr_3$ Detectors

Excited states in nuclei have lifetimes that vary drastically. Following a decay, germanium detectors are ideal for measuring longer lifetimes ($>$ 10 ns), but for shorter lifetimes different γ-ray detectors are needed. The $LaBr_3$ scintillator is fast and has enough resolution to measure discrete γ-ray transitions with lifetimes $>$ 400 ps [99]. For the first two FRIB experiments, 15 $LaBr_3$ detectors were constructed by coupling a 2" (diameter and thickness) cylindrical Saint-Gobain $LaBr_3$(Ce) crystal to a Hamamatsu photomultiplier for the Hybrid Array of Gamma Ray Detectors (HAGRiD) [100]. The detectors were mounted in DEGAi, with 11 upstream from the implant detector and 4 situated below the implant detector, shown as the grey detectors with orange mounts in Figure 3.2.

Neutron Detection

The NEXTi (NEutron detector array with Xn Tracking Initiator) system consists of 88 scintillating bar detectors in the medium VANDLE (Versatile Array of Neutron Detectors at Low Energy) bar size [101, 102]. Each bar uses a $3 \times 6 \times 120\text{cm}^3$ EJ-200 scintillator [103]

coupled to two Hamamatsu scintillators [95], one on each end of the bar. The 88 bars were arranged into a double wall, where the first set of detectors was located 90 cm away from the center of the implantation detector, and the second was located directly behind the first with a radius of 96 cm. Each detector is run in a triple coincidence mode, requiring a signal from both PMTs along with the β (start) detector.

3.2.2 Second Focal Plane

The second focal plane of FDSi is the site of the Modular Total Absorption Spectrometer (MTAS) [2]. This detector system consists of 24 NaI bars with a photomultiplier tube on each end, for gamma and neutron detection. MTAS is specifically designed to have a very high efficiency, allowing for the measurement of β-decay feeding to different excited states which can de-excite in a multitude of paths. Oftentimes, the de-excitation of highly excited states is fragmented, yielding many different γ-rays that can be missed using clover detectors with good energy resolution. Accurately determining the feeding distribution is pivotal in being able to properly reconstruct the full decay of a specific nucleus. This experiment employed a new segmented central module, allowing for more discrimination between multiple low-energy γ-ray transitions and a single higher-energy transition [104].

Implant Detector for MTAS

For the first MTAS experiment at a fragmentation facility, a new implant detector was needed which could measure both high-energy implants after stopping them and low-energy decay signals. While a traditional scintillator-based implant detector, such as the one used in the first focal plane, is the simplest solution, the cylindrical center with a 2" diameter of MTAS did not allow for a square 2" MAPMT to fit. Due to this geometrical constraint, a new detector had to be designed and constructed. The scintillator-based design was kept, but instead of a MAPMT, a Sensl J-series 8x8 silicon photomultiplier (SiPM) array [105] was coupled to the scintillator. Similar to the first focal plane, a 48x48 segmented YSO scintillator was used with a thickness of 5 mm. After the scintillator light diffusers spread the light generated by the highly segmented scintillator before the coupled SiPM array. For

these square materials to fit inside the central module, the corners were removed. Cutting the corners of the SiPM array led to a loss of 13 SiPMs, for an active total of 51 SiPM detectors in the array. The signals were read out through a Vertilon SIB464-2208 interface board which split each SiPM signal into a raw and 10x attenuated signal [96]. Additionally, to prevent saturation of SiPMs due to the intense light output from the YSO during implantation events, tinted foil was added to reduce the amount of light detected by the SiPM array. A higher threshold for decay signals resulted from the tinting. The full detector is shown in Figure 3.4, including it being mounted to a 3D-printed holder, which allows for insertion into MTAS and extraction from inside MTAS.

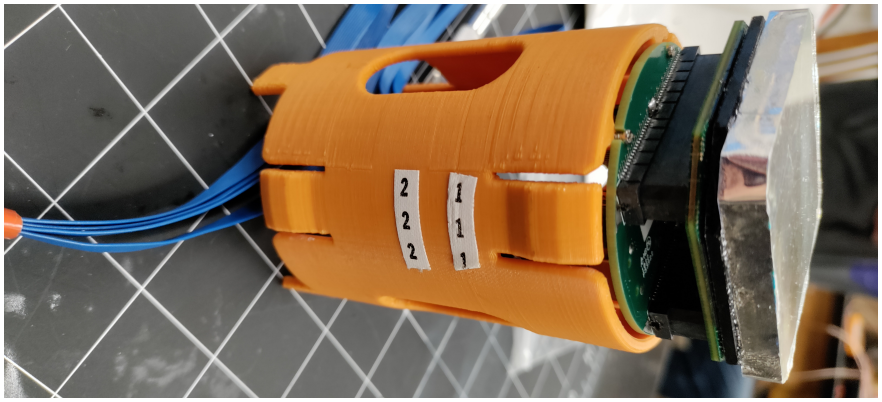

Figure 3.4: A photo of the MTAS implant detector, with the YSO scintillator (silver) coupled to a 2 mm tinted glass diffuser, and the diffuser coupled to the SiPM array. The readout board is then connected to the back of the array and mounted on the orange 3D-printed holder for insertion into and extraction from MTAS.

Chapter 4

Analysis

4.1 Particle Identification

Particles received from the ARIS separator must be properly identified on an event-by-event basis. The proton number (Z) of ions to be implanted is measured through the energy loss in silicon detectors, while the mass-to-charge ratio (A/Q) is measured through the time of flight of ions traveling through the separator. These two quantities allow for specific nuclei to be separated, as shown in Figure 4.1 which includes an energy loss calibration from the silicon detector. Initially, ^{54}Sc was used to anchor the particle identification, as it can easily be located through ion-γ coincidences due to the isomeric first excited state ($E_\gamma = 110$ keV and $t_{1/2} = 2.77\mu s$).

Discrete shifts in the time-of-flight calculations were encountered on a run-by-run basis, corrected, and aligned to a single time of flight for each ion. After this time-of-flight, t, alignment, and calibration of the pin detector energy, E_p, allows for the extraction of the atomic number for ions passing through the diagnostic cross. Equation 4.1 outlines the process for calibrating the pin detector, where parameters a_i and b_i are dependent on the separator settings.

$$\begin{aligned} Z' &= a_0 + \frac{a_1 E_p^{a_2}}{a_3 + a_4 t} \\ Z &= b_2 Z'^2 + b_1 Z' + b_0 \end{aligned} \tag{4.1}$$

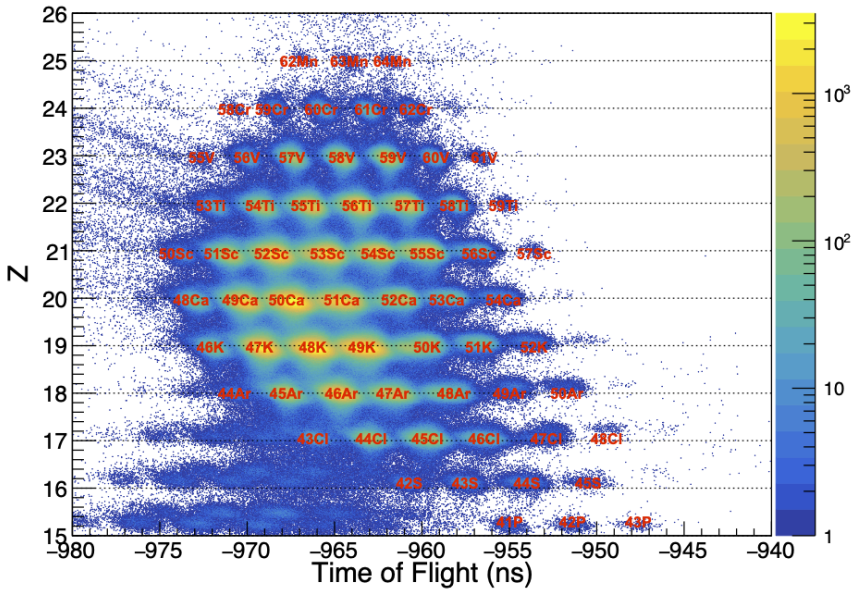

Figure 4.1: The particle identification plot for the first part of the e21069 experiment merged from multiple different beam settings. Z is determined from the energy loss in a pin detector and the time of flight is determined from the time between an upstream scintillator and a scintillator in the diagnostic cross before the pin detector.

Charged particles in a magnetic field move under the influence of the Lorentz force. Ions traveling through the ARIS magnetic spectrometer behave relativistically due to their large energies after fragmentation. The magnetic rigidity, $B\rho$, can then be related to the mass, Am_0 where m_0 is the atomic mass unit, and charge, Q, of an ion traveling through the magnetic field, as shown in Equation 4.2 [106]. Lighter ions, such as those studied in this work, are fully stripped ions after fragmentation, giving $Q = Z$.

$$B\rho = \frac{A}{Q} m_0 c \beta \gamma, \quad \beta = \frac{S}{tc}, \quad \gamma = \frac{1}{\sqrt{1-\beta^2}} \tag{4.2}$$

Rewriting, the mass-to-charge ratio can be written in relation to the time of flight, t for the ion to travel the path of specified length, S.

$$\frac{A}{Q} = \frac{B\rho}{m_0 c} \frac{\sqrt{t^2c^2 - S^2}}{S} \tag{4.3}$$

4.1.1 LISE++ Simulations

To estimate the anticipated beam rate and implantation energies for various ions, the LISE++ program [107] was used to calculate beam properties for desired ions. Properties of interest include ion transmission, ion implantation rate, ion range in materials, and ion total kinetic energy (TKE). Some of these attributes can be measured using the current FDSi setup, such as ion transmission and implantation rate, whereas others are currently unable to be directly measured. For instance, the implantation depth inside the YSO implant detector is unknown, but ranging out measurements can be done to stop ions short of implanting, or letting ions pass through the scintillator without implanting to help calibrate LISE calculations for the ion implantation depth. Along with this, LISE++ predictions of the ion TKE are used to determine the quenching factor due to the light creation in the scintillation-based implant detector. This will be discussed later.

4.2 Implant-β Detector

As discussed earlier in subsection 3.2.1, the two-branch system for splitting signals from the YSO detector is pivotal for being able to measure both high-energy ion implantations along with subsequent decays, but this is not always enough. Additionally, the YSO scintillator exhibits light quenching for heavy ions, where the light output created from heavy ion implantations is not linearly proportional to the total kinetic energy of the ion as it is implanting. Figure 4.2 demonstrates the light quenching from many different ions including ^{24}O and a range from ^{45}S to ^{58}V, measured at FRIB in the span of 2 experiments. The implantation energy is extracted linearly from the light yield of ^{60}Co γ-rays and does not match the simulated implantation energy calculated by LISE++ due to the light quenching.

To optimize the data acquisition before an experiment, the light quenching for desired ions must be estimated. This can be done using Birk's formula, Equations 4.4, such that the stopping power, dE/dx, can be found through the Bethe-Bloch formula, Equation 4.5 [98, 108] or calculated at different energies for various materials using the Stopping and Range

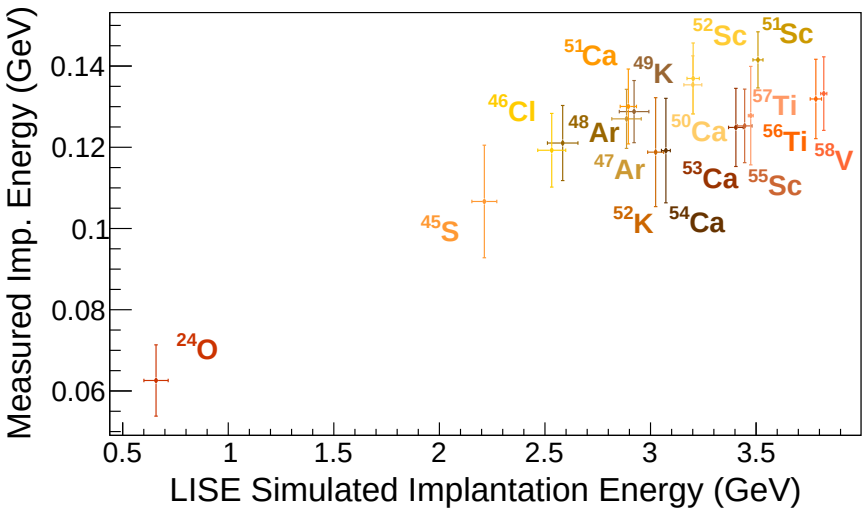

Figure 4.2: Comparison between the expected ion implantation energy vs the measured ion energy, demonstrating the light quenching from the YSO scintillator.

of Ions in Materials (SRIM) [109].

$$\frac{dL}{dx} = \frac{S(dE/dx)}{1 + kB(dE/dx)} \tag{4.4}$$

$$-\frac{dE}{dx} = 4\pi r_0^2 z^2 \frac{m_e c^2}{\beta^2} NZ \left(\ln\left(\frac{2m_e c^2}{I}\right) - \ln(1-\beta^2) - \beta^2 \right) \tag{4.5}$$

Koba et al. modified the original Birk's formula into a new equation for the scintillation efficiency, Equation 4.6, which can be used to extract the light yield for an ion of a specific energy, assuming the correct Birks parameters, a and b, and known.

$$\frac{dL}{dE} = \frac{a}{1 + b(dE/dx)} \tag{4.6}$$

Up to this point, these parameters have not been determined for YSO scintillator detectors. To do so, an average value approximation was used, where the quenching factor determined experimentally is an average resulting from some average distribution of energy loss for implanting ions. The scintillation efficiency, taken as the reciprocal of the quenching factors with respect to the average energy loss for heavy ions predicted by SRIM, is then fit with Equation 4.6. The resulting Birk's parameters for YSO were determined to be $a = 0.122$ and

$b = 6.87 \times 10^{-4}$ [110]. Thus, using previous experimental data we can predict the quenching factors for ion implantations at large energies.

4.2.1 Half-life Determination

The YSO implant detector is used to measure both ion implantation and β-decay events. Implantation events are qualified as events that have a large energy signal in the YSO, a valid particle identification (discussed earlier), and no energy deposition in the rear ion veto. Decay events, on the other hand, are qualified as events that have a smaller energy signal in the YSO and no signals from any of the upstream detectors (the pins or plastic timing detectors). The plastic front veto can be used to further remove β-decay events which leave the YSO and create a signal in the front plastic. Each event that is qualified as a β-decay is then correlated with all ion events within a specific time window and correlation radius, defined in Equation 4.7 with x_β and y_β being the β-decay coordinates, while x_i and y_i are the implant coordinates.

$$r = \sqrt{(x_\beta - x_i)^2 + (y_\beta - y_i)^2} \tag{4.7}$$

Figure 4.3 demonstrates the ion implantation acceptance and rejection based on the correlation radius, black circle, from the qualified β decay, shown as the black dot. In this case, since the blue dot is inside the correlation radius, it is accepted as a possible ion, while the red dot is outside and rejected.

The time difference between the ion implant events and the β-decay events is then used to extract the half-life, $t_{1/2}$, of the radioactive nucleus. The histogram of time differences can then be fit using the Bateman equation [111]. For exotic chlorine isotopes, $P_{0,1,2}$ decay channels all contribute to the half-life determination. Figure 4.4 shows the possible decay chains which include possible β-delayed neutron emission from the parent (Z), daughter ($Z-1$), and granddaughter nuclei ($Z-2$). In the case of β-delayed single neutron emission, one would follow the first black arrow from ${}^{A}Z \rightarrow {}^{A}(Z-1)$ followed by transitioning along the red line to ${}^{A-1}(Z-1)$, which is the P_{0n} daughter.

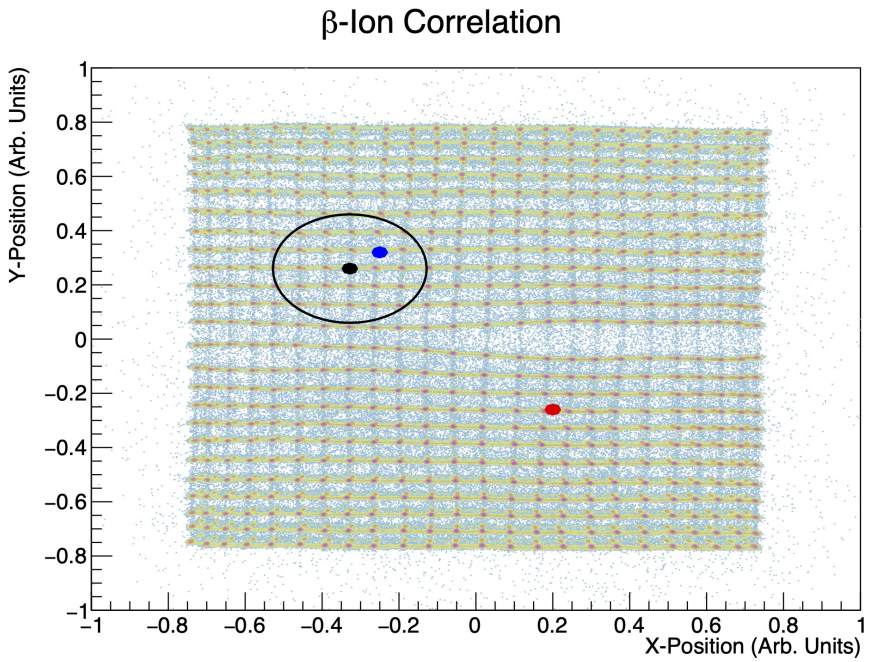

Figure 4.3: β-Ion correlation diagram, where the β decay, the accepted ion implantation, and rejected ion implantation are shown as the black, blue, and red dots, respectively. The black circle shows the maximum accepted correlation radius.

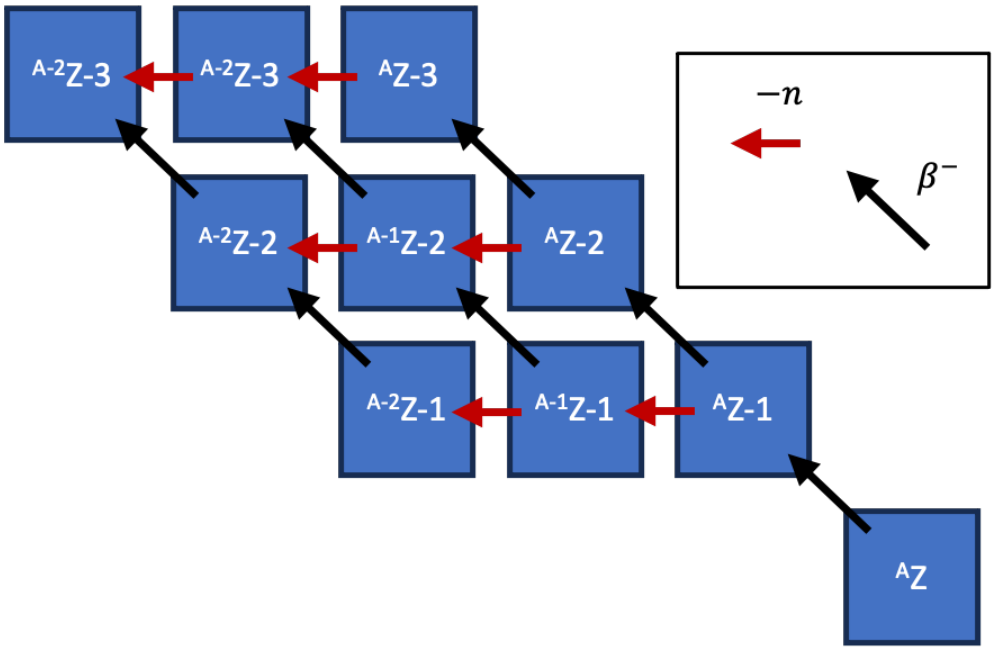

Figure 4.4: Possible decay chain for a neutron rich exotic nucleus where β^- decay (black arrow) can be followed by neutron emission (red arrow).

4.3 Analysis of HPGe Data

Due to the compact nature of clover detectors, γ-rays can scatter between the individual crystals and leave partial energy deposition in each affected crystal. Add-back techniques are used to counter this process by summing the energies from each crystal in a clover during an event. This allows for the full energy of the γ-ray to be reconstructed. Furthermore, DEGAi places clover detectors next to each other, allowing for scattering between crystals in different clover detectors. The Angular Addback method is then used to account for this scattering between clovers by mapping each crystal with both a θ and ϕ angle relative to the implant detector and summing crystals that are within a specific angular range. For this analysis, the cutoff was set to 30°.

The clover γ-ray detection efficiency curve was based on simulations and scaled to match experimental data in Refs. [112, 113]. Specifically, the transitions at 224 and 401 keV from ^{32}Na [112] were used for benchmarking at low energies and the 1495 keV transition, whose γ-intensity following β-decay is known from Ref. [113], benchmarked the curve at higher energies. Figure 4.5 shows the full curve, which peaks at low energies and has an overall detection efficiency of 3.6% at 1 MeV when using the angular add-back correction.

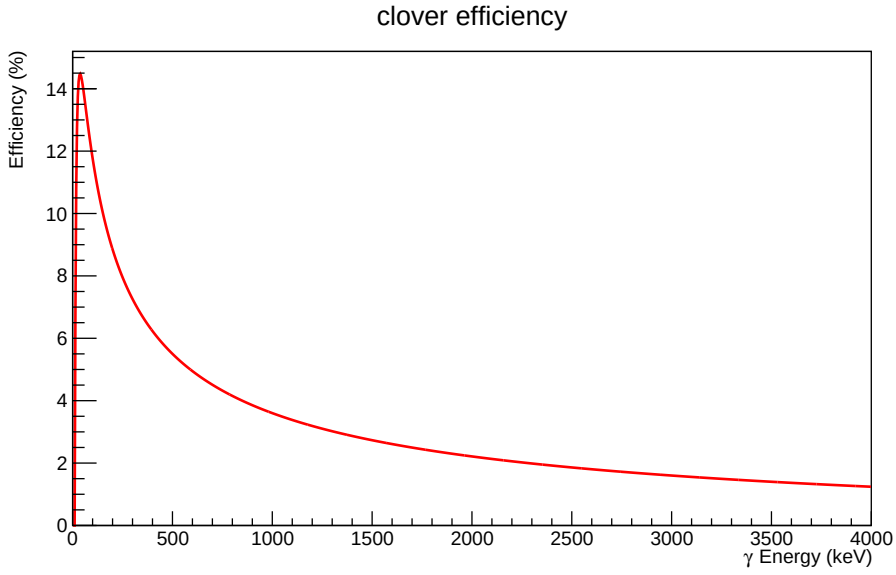

Figure 4.5: The detection efficiency curve for γ-ray detection using the 2π DEGAi hemisphere consisting of 11 clover detectors. More details are in the text.

4.4 Analysis of $LaBr_3$ Detectors

For fast timing measurements, the polynomial constant fraction discrimination (poly-CFD) algorithm [114] was used to extract high-resolution timing from the trace of a $LaBr_3$ signal. The poly-CFD algorithm requires further correction based on the energy of the signal as well as a ru-dependent correction. The energy-dependent correction is used to correct "walking," where a polynomial fit is used to characterize the dependence and correct. Different latching times for each detector also need a correction based on each run. Figure 4.6(left) demonstrates this issue, where each detector has multiple different peaks corresponding to prompt $\beta - \gamma$ signals for different runs. Once the run and walk corrections are implemented, all of the $LaBr_3$ events can be combined to look at the time difference between a single $LaBr_3$ signal and a β detection in the YSO detector, shown in Figure 4.6(right). Each γ-transition following a β-decay which has a lifetime shorter than the timing resolution of the system will produce a "prompt" peak, following a Gaussian distribution with a time difference centered at 0 ns. States with a significant lifetime, on the other hand, will produce a tail on the right of the peak, where the γ-ray emission is delayed. A few transitions that have this tail component are shown in Figure 4.6(right).

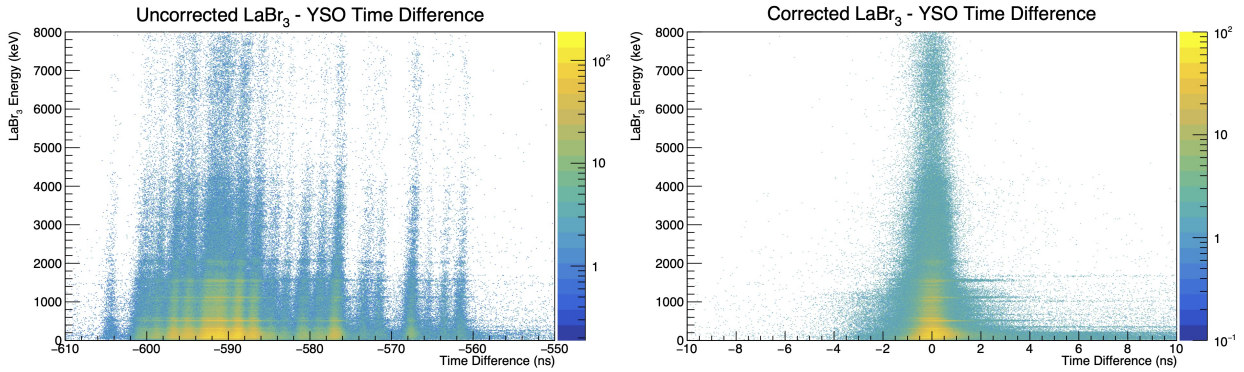

Figure 4.6: (Left) Uncorrected time difference between $LaBr_3$ and YSO detectors, plotted against each individual $LaBr_3$ detector. (Right) Corrected time difference between $LaBr_3$ detectors and the YSO detector, plotted against the $LaBr_3$ energy to identify γ-ray transitions from excited states with a measurable lifetime.

4.5 MTAS Data Analysis

4.5.1 MTAS Calibration

During the experiment gain matching is performed on each of the MTAS PMTs so that they perform similarly. The gain matching procedure uses sources to roughly align known γ-ray energies to the equivalent raw energy bin from the data acquisition. Still, an added second-order correction is needed to properly calibrate all of the individual modules, especially at higher energies. Table 4.1 shows the sources and corresponding γ-ray energies (E_γ) used for the secon-order calibration. After the calibration data was taken, experimental conditions changed causing gain shifts for each of the detectors. The gain shifts were assumed to be linear, therefore an additional correction for each detector was made for each run. Multiple background lines were tracked, shown as the energies with a dagger in Table 4.1, and corrected to match their calibrated energy.

4.5.2 Modeling the MTAS Response

The large amount of NaI used in MTAS allows for very high partial-γ absorption, where the γ-ray scatters in the detector without leaving a full energy deposition. By measuring the partial-γ energy along with when there is a full energy deposition, MTAS can increase its overall efficiency. To accurately describe the detector response to γ-ray and β emission, simulations were carried out in Geant4 [115] for each possible decay path following a β-decay.

Table 4.1: Sources and corresponding γ-ray energies (E_γ) used for calibrating the MTAS detector. Energies with a dagger (†) were used for tracking gain drifts during online runs.

Source	E_γ (keV)
^{109}Cd	88.
Pair Production	511.†
^{137}Cs	662.
^{60}Co	1173.
^{60}Co	1332.
^{40}K	1460.†
^{208}Tl	2614.†

The expected response to a possible decay path is then known for each of the 24 detectors in MTAS and can be used to fit experimental data. Simulations were also used to model β-decay feeding to neutron unbound states which result in the emission of a neutron and possibly γ-rays as well. An example of the simulated 662 keV γ-ray from the β-decay of ^{137}Cs is shown in Figure 4.7 as the black line.

The output from the MTAS Geant4 simulation does not accurately reflect the detector energy resolution. Due to this, additional post-processing is needed to broaden the width of peaks produced in the simulation and to calibrate the simulation to the expected energy. Using the source γ-rays listed in Table 4.1, the width of peaks can be measured at different energies for each individual detector. These measured widths are then folded into the simulation result for an accurate detector response, shown in Figure 4.7 as the red line.

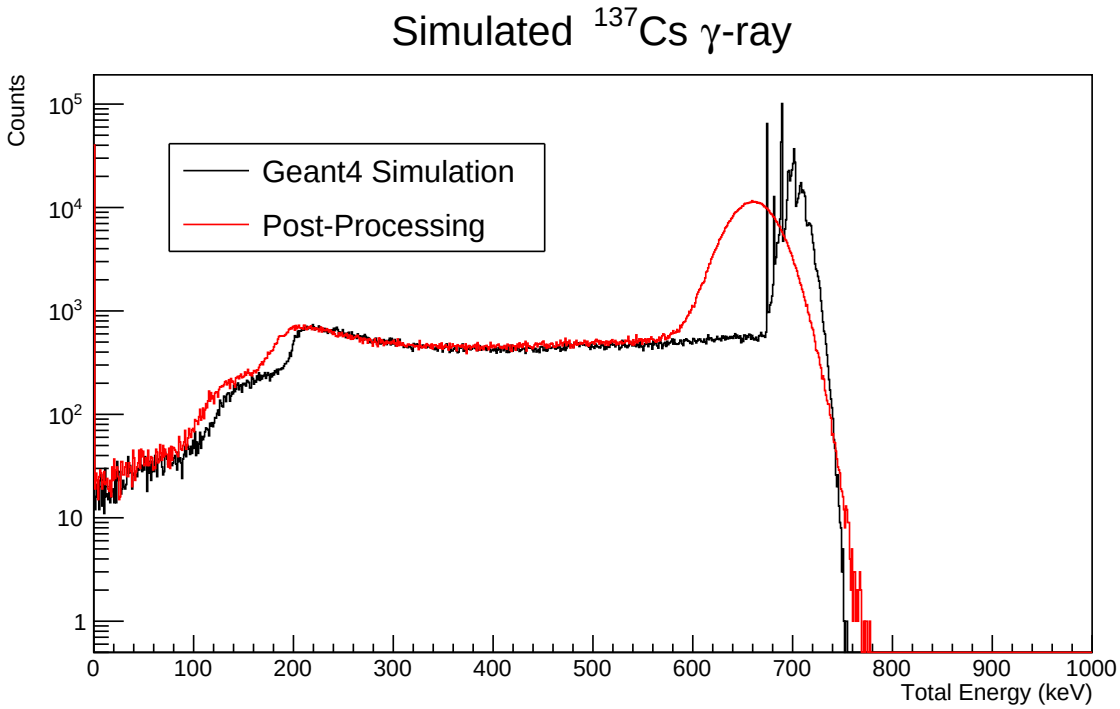

Figure 4.7: Comparison of raw Geant4 simulations of the MTAS response (black) to the 662 keV γ-ray emitted after the β-decay of ^{137}Cs and the post-processed simulation data for the same transition in MTAS (red).

4.5.3 MTAS Spectra Deconvolution

To best deconvolute the MTAS spectra, a Bayesian-based iterative algorithm is used to fit numerous response functions to the experimental data. Introduced by Shuai et al. [116], the algorithm fits response functions to experimental sum spectra and coincidence spectra, where the number of total spectra included can be extended as needed. The key advantage of the Bayesian algorithm is exploiting the iterative process by using parallel and/or GPU processing to simultaneously fit a large number of spectra relatively quickly. Below is a description of the algorithm following the basis described in the appendix of Ref. [116].

The deconvolution is first based on the assumption that the experimental data d_i can be regarded as a linear combination of the simulated response functions for each decay path, R_{ia}, weighted by some scale factor, s_a.

$$d_i = \sum_{a=1}^{M} R_{ia} s_a, \quad a = 1, ..., M \tag{4.8}$$

Here, the index i represents one of the energy bins used in the deconvolution and M is the total number of response functions included in the fit. Thus, d_i is the total number of counts in an individual energy bin. By solving for all of the scale factors, the feeding intensities can be calculated,

$$I_a = \frac{a_a}{\sum_{a=1}^{M} s_a}, \quad a = 1, ..., M \tag{4.9}$$

The β-decay feeding intensities to each excited state can then be calculated by summing the feeding intensities for each path that fed the same level. For the iterative algorithm, we start with a set of positive nonzero values, $s_a^{(r=0)}$, where r is the iteration. From here we use the equations,

$$s_a^{(r+1)} = \frac{1}{\sum_{k=1}^{N} R_{ka}} \sum_{i=1}^{N} \frac{R_{ia} s_a^{(r)} d_i}{\sum_{b=1}^{M} R_{ib} s_b^{(r)}}, \quad a = 1, ..., M \tag{4.10}$$

To fit the 2-dimensional coincidence spectra, we can use the experimental spectra, $d_i \rightarrow d'_{ij}$, where i might be for the energy deposited in the central module and j is the total energy

sum for the event. The 2D equivalent of Equation 4.10 would be,

$$s_a^{(r+1)} = \frac{1}{\sum_{k=1}^{N}\sum_{l=1}^{N} R'_{kla}} \sum_{i=1}^{N}\sum_{j=1}^{N} \frac{R'_{ija} s_a^{(r)} d'_{ij}}{\sum_{b=1}^{M} R'_{ijb} s_b^{(r)}}, \quad a = 1, ..., M \tag{4.11}$$

Lastly, since $s = \frac{a}{b} = \frac{c}{d} = \frac{a+c}{b+d}$ for $b, d \neq 0$, we can fit the 1D and 2D spectra, or any other spectra, simultaneously to constrain γ-multiplicities and uncertainties [116].

Uncertainty Analysis

When running at ISOL facilities, such as CARIBU or the Holifield Radioactive Ion Beam Facility, MTAS experiments were able to have minimal random background in coincidence with the β-trigger detector. This experiment, on the other hand, is the first use of MTAS at a fragmentation facility, where randomly correlated β decay events are a consequence of other desired ions in the separator acceptance to be studied. Due to this, the background counts can be large and need to be taken into account. To properly distinguish the decays of interest from the background data, a time-since-implant gate, dT, is used to subtract the random background, with $dT < 0$, from the random and real events, with $dT > 0$. From this, all further spectra have error bars which are taken into account. To quantify the statistical error, each energy bin in the negative time is randomly sampled in a Gaussian distribution with $\mu_i = n_i$ being the experimental value and $\sigma_i = \sqrt{n_i}$ being the error bar. Here, n_i is the number of counts in the ith bin. Each fit was then run 500 times to determine the effect statistical effect on the fit.

4.6 VANDLE Neutron Detector

4.6.1 Principles of neutron Time-of-Flight detection

Neutrons emitted after β-decay are non-relativistic, therefore, their kinetic energy, E_n, can be measured classically using their time-of-flight (ToF). This is shown in Equation 4.12, where $m_n = 939.6\text{MeV}/c^2$ is the mass of the neutron, l is the distance between the β-decay and the detected neutron, and t is the time-of-flight between the β-decay signal from the

YSO (start signal) and the VANDLE bar (stop signal).

$$E_n = \frac{1}{2} m_n v^2, \quad v = \frac{l}{t} \tag{4.12}$$

$$\left(\frac{\Delta E}{E}\right)^2 = \left(\frac{2\Delta t}{t}\right)^2 + \left(\frac{2\Delta l}{l}\right)^2 \tag{4.13}$$

The neutron energy resolution (ΔE) is resultant from the uncertainty of measuring the distance the neutron traveled (Δl) and the uncertainty of the time of flight for the neutron (Δt), shown in Equation 4.13. The limiting factor in the distance uncertainty is the position resolution of the VANDLE bar. To overcome this limitation, the uncertainty in the time of flight must be minimized for high-resolution measurements, thus high-resolution timing algorithms are implemented for both the YSO detector and the VANDLE bars. Like the previously discussed $LaBr_3$ detectors, poly-CFD algorithm [114] is used to extract timing from traces taken on both the start and stop detectors. Corrections were done bar by bar and run by run to ensure that each detector was time-aligned.

4.6.2 VANDLE Response Function Simulations

To accurately characterize the response of VANDLE to different neutron energies during FDSi experiments, simulations were performed by S. Neupane using Geant4 [115] with varying mono-energetic neutrons, with a resultant response in ToF and efficiency for the neutrons. The response is then fit with a Lorenzian plus 3 exponentials function, shown in Equation 4.14 as $f(x)$ where x is the ToF. The Lorentzian function is broken up into a left and right allowing for different widths, and the variables for the function are listed in Table 4.2 along with a fit of the function to a Geant4 simulated 1.5 MeV neutron is shown in Figure 4.8. The fit is used to determine the amplitude, A, for a peak and the centroid of the peak, x_0. Additionally, each parameter listed in Table 4.2 can be dependent on the time of flight, up to a second-order polynomial. This gives the 0th, 1st, and 2nd order subsets of each parameter, such that a parameter p can be written as, $p = p^{(0)} + p^{(1)}x + p^{(2)}x^2$.

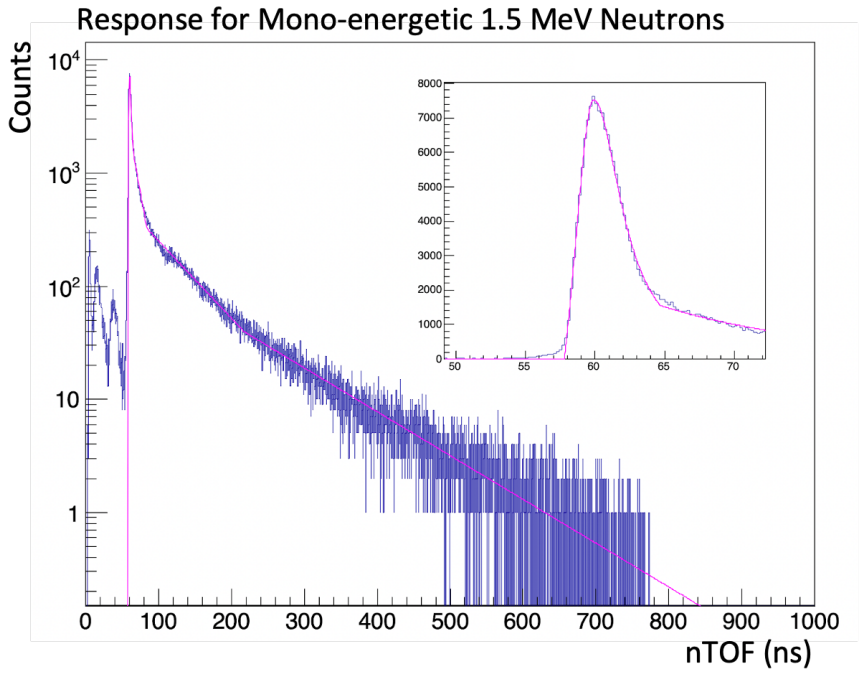

Figure 4.8: Simulated response function from Geant4, fit using the Lorentzian plus 3 exponential function formulated in Equation 4.14.

Table 4.2: Parameters for the NEXTi neutron response function.

Name	Variable	0th	1st	2nd
Lorentz FWHM/2 right	σ_r	0.22803	0.01493	2.3027×10^{-4}
Lorentz FWHM/2 left	σ_l	0.1502	7.6617×10^{-3}	1.5351×10^{-4}
Offest	o	0.030078	-8.3044×10^{-5}	
Exponential constant	k_1	0.15862		
	k_2	0.020581	-2.2709×10^{-5}	4.1209×10^{-6}
	k_3	0.017365		
Tail Offset	d_1	3.1700	-0.027571	7.851×10^{-5}
	d_2	6.608	0.12026	
	d_3	107.19		

$$
\begin{aligned}
gv &= \frac{x - x_0}{\sigma_r} \\
f(x) &= \frac{A}{N}(gv \leq 0)\left(\frac{o+1}{1+(gv\sigma_r/\sigma_l)^2} - o\right) \\
&+ \frac{A}{N}(0 < gv \leq (k_1+d_1))\frac{1}{1+(gv)^2} \\
&+ \frac{A}{N}((k_1+d_1) < gv \leq (k_2+d_2))\left(\frac{e^{k_1^1+k_1 d_1}}{1+(k_1+d_1)^2)}\right)e^{-k_1 gv} \\
&+ \frac{A}{N}((k_2+d_2) < gv \leq (k_3+d_3))\left(\frac{e^{k_1(k_1+d_1)-(k_1-k_2)(k_2+d_2)}}{1+(k_1+d_1)^2}\right)e^{-k_2 gv} \\
&+ \frac{A}{N}((k_3+d_3) < gv)\left(\frac{e^{k_1(k_1+d_1)-(k_1-k_2)(k_2+d_2)-(k_2-k_3)(k_3+d_3)}}{1+(k_1+d_1)^2}\right)e^{-k_3 gv}
\end{aligned}
\tag{4.14}
$$

The normalization, N, is given by Equation 4.15.

$$
\begin{aligned}
t_0 &= e^{-d_2 k_1 - k_2(k_3+d_3+k_1)} \\
t_1 &= -k_1 e^{d_1 k_1 + k_1^2 + k_2^2 + k_2 d_2} \\
t_2 &= (k_1 - k_2)e^{d_1 k_1 + k_1^2 + k_2(k_3+d_3)} \\
t_4 &= \tan^{-1}(k_1 + d_1) \\
t_5 &= -\sigma_l\sqrt{o} + (1+o)\sigma_l \tan^{-1}(o^{-0.5}) \\
N &= \frac{\sigma_r}{1+(k_1+d_1)^2}\left(\frac{t_0(t_1+t_2)}{k_1 k_2} + \frac{t_3}{k_3}\right) + \sigma_r t_4 + t_5
\end{aligned}
\tag{4.15}
$$

4.6.3 Neutron Detector Calibration

Verification of the response function was performed using the neutron spectrum from β-delayed neutron emission of ^{49}K. Fitting the curve with known neutron energies from Ref. [117] allows for slight changes to the response function parameters, yielding the values found in Table 4.2. The result is shown in Figure 4.9, where the final response function does well to describe the known neutron spectrum. Furthermore, to ensure that the results were consistent with previously measured data, the decay strength from the fit is compared against data used to calibrate the ISOLDE Decay Station Neutron Detector (INDiE) during

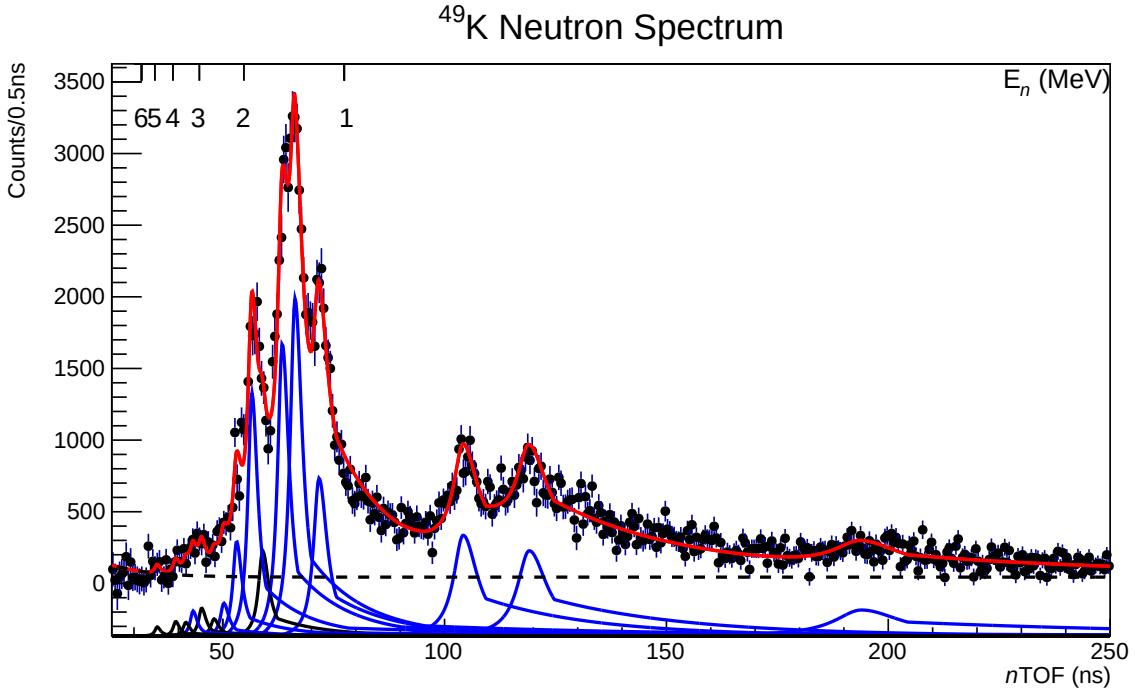

Figure 4.9: Deconvolution of the neutron time-of-flight spectrum from the β-decay of ^{49}K, used to calibrate the FDSi neutron response function.

experiment IS609 at the ISOLDE Decay Station, where the deconvolution is reported in Ref. [118]. Figure 4.10 shows the agreement between the two measurements, verifying the FSDi response function.

The ^{49}K calibration also benchmarked the efficiency curve extracted from the simulations. Figure 4.11 shows that the array has a peak efficiency of near 20% at 500 keV, with a sharp decline for lower energies, but a much slower drop off for increasing energies.

4.6.4 Neutron Time-of-Flight Deconvolution

The neutron spectrum deconvolution process is used to fit the neutron spectrum with the response function described earlier, such that the β-decay feeding intensities to neutron unbound states in the P_{1n} daughter can be measured along with the ability to measure the branching ratio of neutron emission from neutron unbound states to excited states in the P_{1n} daughter. This analysis used the deconvolution method developed by Z. Y. Xu, et al. [119] and further extended in Ref. [120]. γ-rays measured in coincidence with neutrons allows

for a multi-graph fit, where neutron-γ spectra are gated on specific γ-transitions in the P_n daughter are fit alongside the total spectra which includes the n-γ peaks measured in the gated spectra scaled up by the efficiency of the DEGAi clover array at the γ-ray energy.

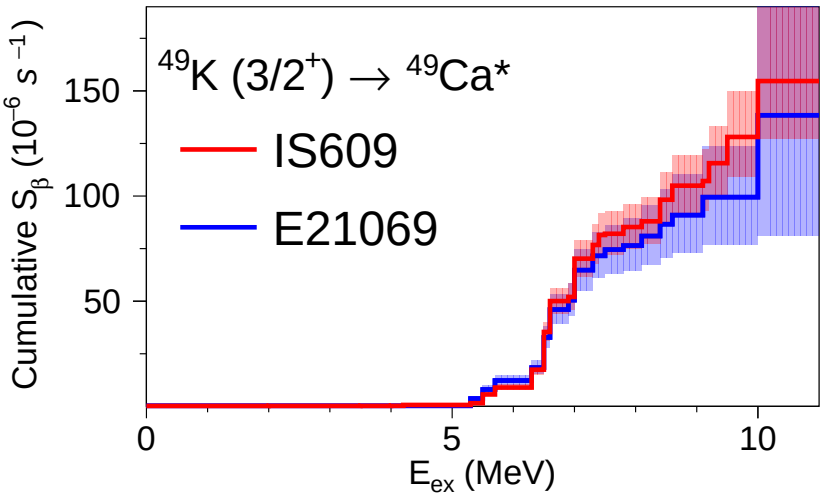

Figure 4.10: Comparison of the β-decay strength distribution of ^{49}K measured by the Isolde Decay Station (red) and FDSi (blue).

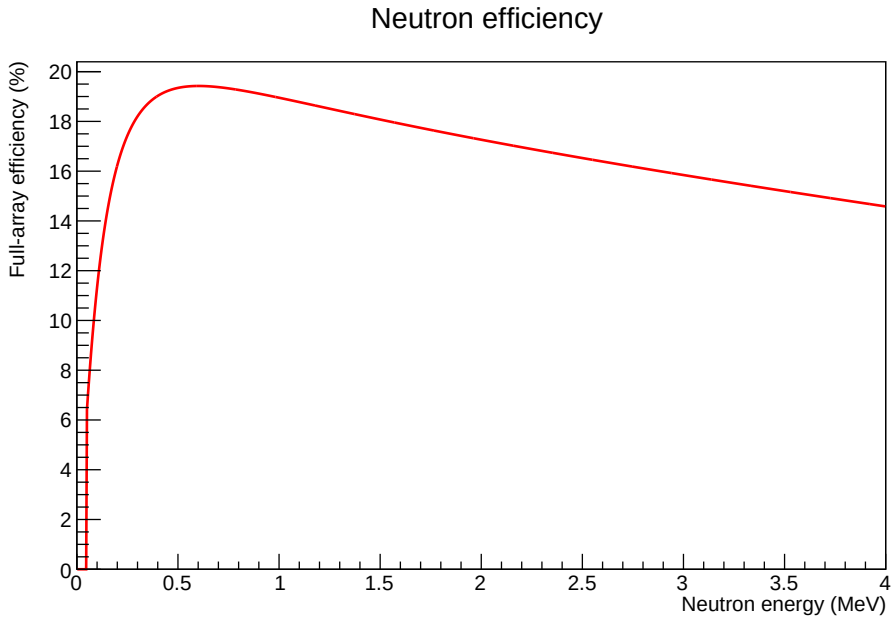

Figure 4.11: Simulated neutron detection efficiency curve the the NEXTi array at FDSi.

Chapter 5

Results

5.1 Decay of ^{44}Cl

The half-life of ^{44}Cl, shown in Table 5.1 and Figure 5.1, was determined to be $t_{1/2} = 672 \pm 34$ ms and $t_{1/2} = 681 \pm 20$ ms using implant-β correlations in the second focal plane and first focal planes, respectively. The two focal planes yield independent, but consistent, measurements which agree with the measurements by Winger, et al. of $t_{1/2} = 640 \pm 40$ms [62] and $t_{1/2} = 672 \pm 18$ms [121], while disagreeing with the value of $t_{1/2} = 434 \pm 60$ms reported by Sorlin, et al. [66], which only had 465 β-decay events.

Due to the large amount of background and low neutron branching ratio, previously determined to be $< 8\%$ [66], the complete feeding intensities were determined using only MTAS. The individual γ-ray transitions were previously reported by Mrazek [69] and Winger [121], which alongside those measured in the first focal plane were used to help

Table 5.1: Measured half-life values for ^{44}Cl in both focal planes compared with previous literature values. The number of β-decays, N_β, in the analysis window of 2000 ms since the implantation is also reported for each focal plane.

$t_{1/2}$ (ms)	Reference	N_β
681 ± 20	E21069B FDSi FP1	66037
672 ± 34	E21069B FDSi FP2	45933
434 ± 60	Sorlin, et al. [66]	
640 ± 40	Winger, et al. [62]	
672 ± 18	Winger, et al. [121]	

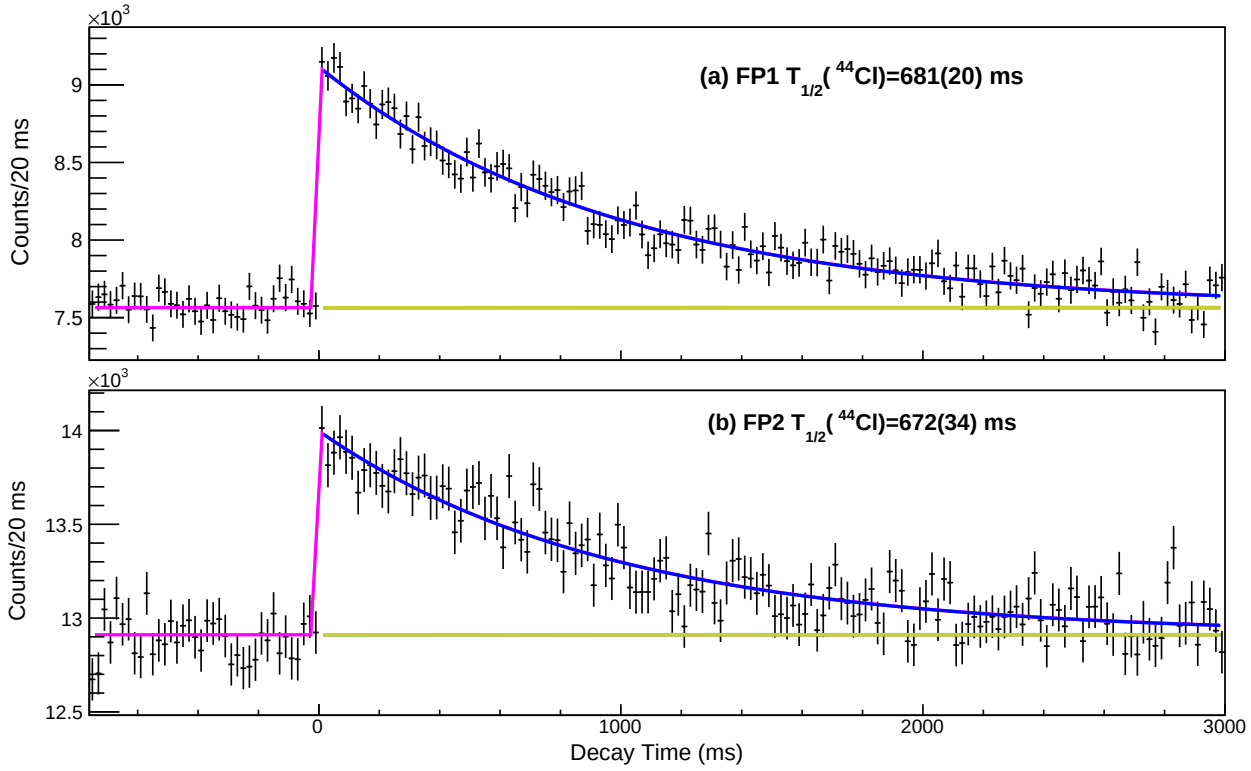

Figure 5.1: Decay curves from e21069b for ^{44}Cl in the first (a) and second (b) focal planes.

guide the deconvolution of the MTAS data. Figure 5.2 shows the combined statistics of e21069a and e21069b for the individual γ-transitions measured using the DEGAi clover array, where the γ-intensities agree with the previously reported values. The most intense transition is located at 1158 keV, representing the de-excitation of the first 2^+ state in ^{44}Ar. Also prominent is the transition at 853 keV between the proposed second 2^+ at 2010 keV and the first excited state. This is confirmed in Figure 5.3 by gating on the 1158 keV transition to find the 853 γ-ray in coincidence, while the 2010 keV transition is not in coincidence.

The total absorption spectrum from MTAS is shown in Figure 5.4, where the response for feeding to each excited state in ^{44}Ar is shown with a varying color from purple to green. Previous measurements only reported β-decay feeding to states below 6 MeV, even though the neutron separation energy is at 8.734 MeV [122]. For newly proposed states above 6 MeV, decay paths are proposed which have the ability to go through previously reported levels. Due to the resolution of MTAS at high energies, these new states are quasi-states that can represent a density of states rather than discrete levels. There is evidence for strong β-feeding to states between 4 and 6 MeV, represented by the strong peaks in Figure 5.4,

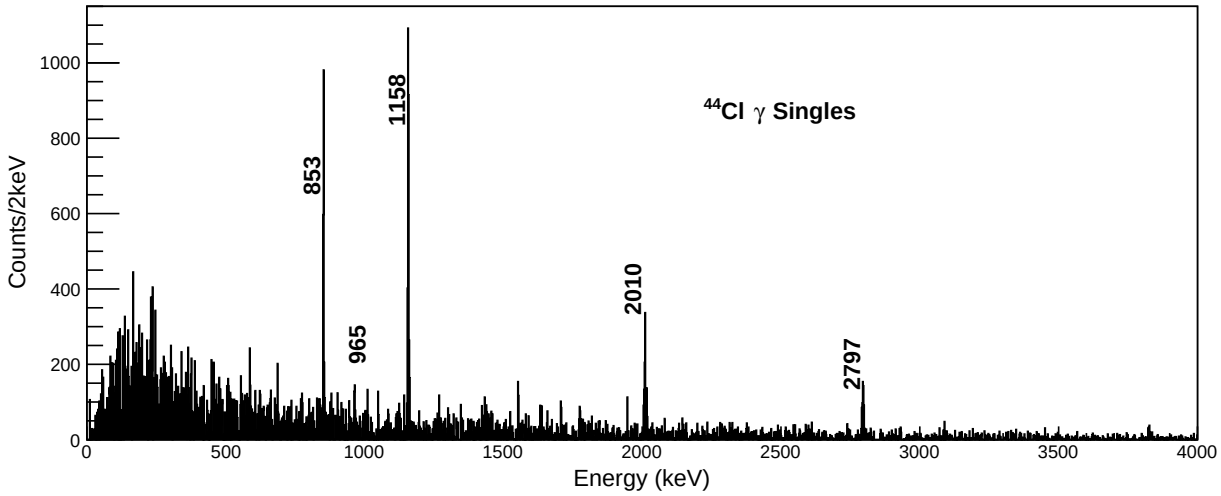

Figure 5.2: Combined statistics from e21069a and e21069b of individual γ-ray energies measured in the first focal plane using the DEGAi clover detector array.

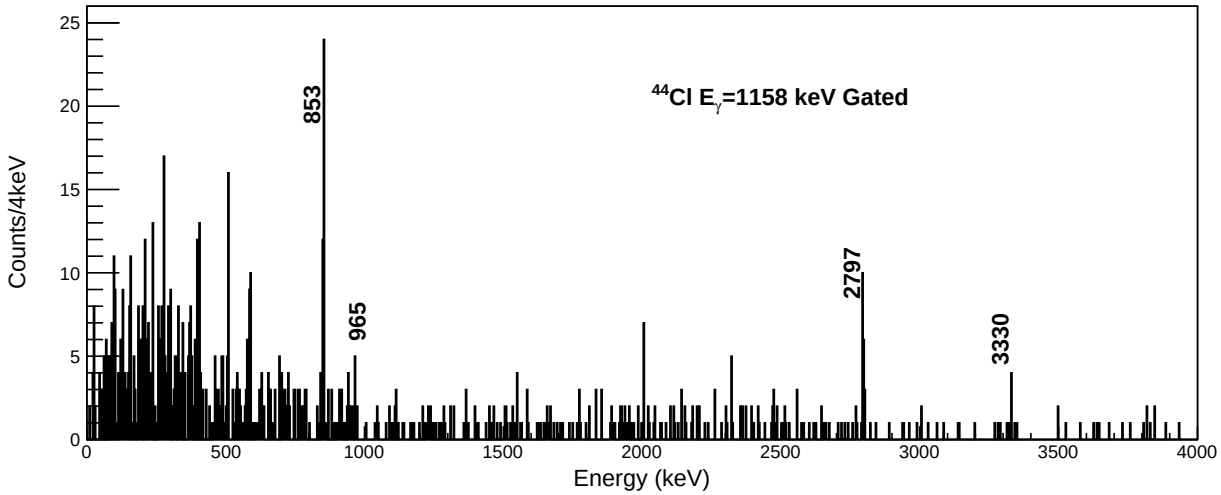

Figure 5.3: Combined statistics from e21069a and e21069b of individual γ-ray energies measured in the first focal plane using the DEGAi clover detector array in coincidence with another γ-ray with $E_\gamma = 1158$ keV.

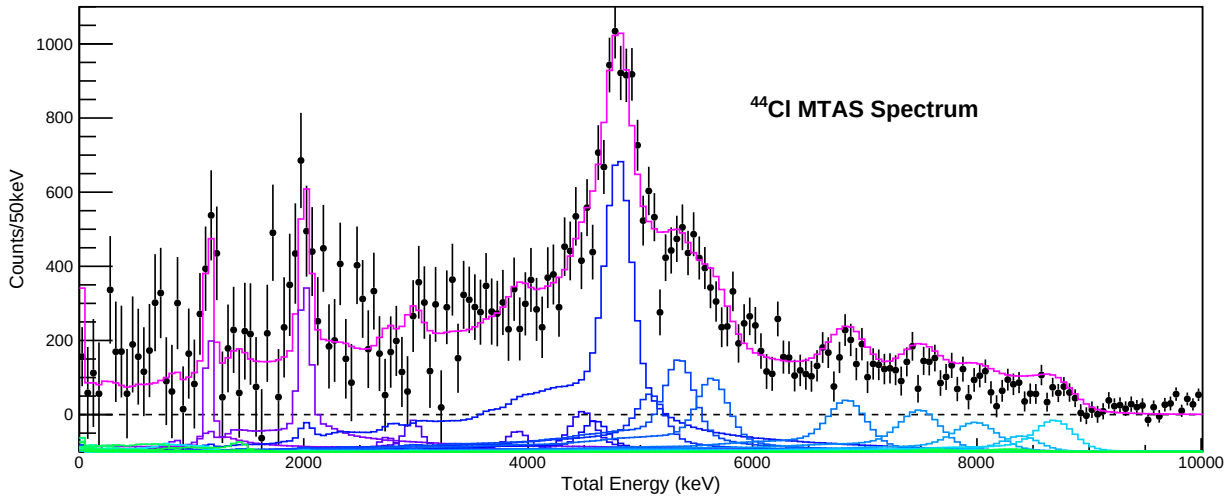

Figure 5.4: The negative-time subtracted MTAS total sum deconvolution for the decay of ^{44}Cl from e21069b using known states below 6 MeV and new states above. The pink line is the total fit, with the purple to green lines shown the response for the feeding to different states. State feeding lines have been shifted down 100 for illustrative purposes.

specifically for the state at 4808 keV. When gating the total sum spectrum on when there is a single 2010 keV γ-ray in the central ring, Figure 5.5, one finds that the states at 4808 keV have a strong cascade through the second 2^+ state. Similarly, the states slightly above 4808 also follow a similar cascade, while those below disappear in the coincidence spectrum indicating different paths to the ground state.

The unique ability to measure the complete decay feeding in MTAS allows for a better understanding of the decay pattern for exotic nuclei. While similar to previously reported feeding patterns, the decay scheme for ^{44}Cl, shown in Figure 5.6, pushes nearly to the end of the Q_β window, with diminishing statistics in the neutron unbound region. The largest differences when comparing to the previously reported feeding intensities from Winger [121] come from lower feedings to the 1158 and 2010 keV 2^+ states and the 4808 keV state. This is due to the inclusion of newer states which have cascades contributing to the γ-intensity for the lowest two states, where if the highly excited states are missed, the β-feeding intensity appears higher to lower states. The cumulative decay strength for ^{44}Cl can be seen in Figure 5.7, where the 4808 keV state is seen as a significant step in the curve. This strong decay feeding is a characteristic of Gamow-Teller transitions, indicating that the state likely has $J^\pi = 1^-, 2^-$, or 3^-. This assignment would be in disagreement with the postulation

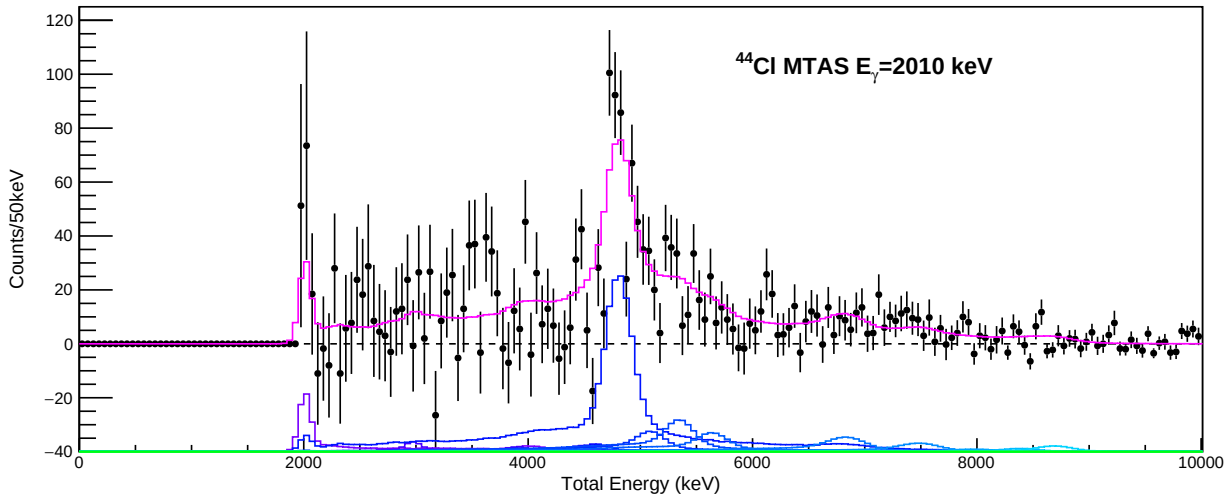

Figure 5.5: The MTAS total sum spectrum gated on states which are in coincidence with a 2010 keV γ-ray in the central ring. This represents states above 2010 keV which are populated in β-decay and cascade through the proposed second 2^+ state before reaching the ground state.

of 2^+ by Bhattacharya [50], where the state was seen to be populated after the β-delayed neutron emission of ^{45}Cl.

5.2 Decay of ^{45}Cl

The half-life of ^{45}Cl was determined using both a Bateman equation fit, described earlier in section 4.2.1, including all daughter decays, with the result shown in Figure 5.8 for e21069A. For decays in coincidence with γ-rays, such as $E_\gamma = 542$ keV corresponding to the first excited state in ^{45}Ar, a simple exponential+background can be used, shown in Figure 5.9. Table 5.2 presents the measured half-life alongside previously measured values. While previous literature values can vary, the value in this work agrees well with the weighted average.

γ-rays measured using the DEGAi clover array over the course of experiments e21069A and e21069B are shown in Figure 5.10, where the most intense line is at 542 keV, between the $3/2^-$ first excited state to the $7/2^-$ ground state. Gating on this intense line, one is able to find higher lying levels that decay through the $3/2^-$ state. An example of this is the 3295 keV state, which has a transition to the ground state shown in Figure 5.10, and multiple

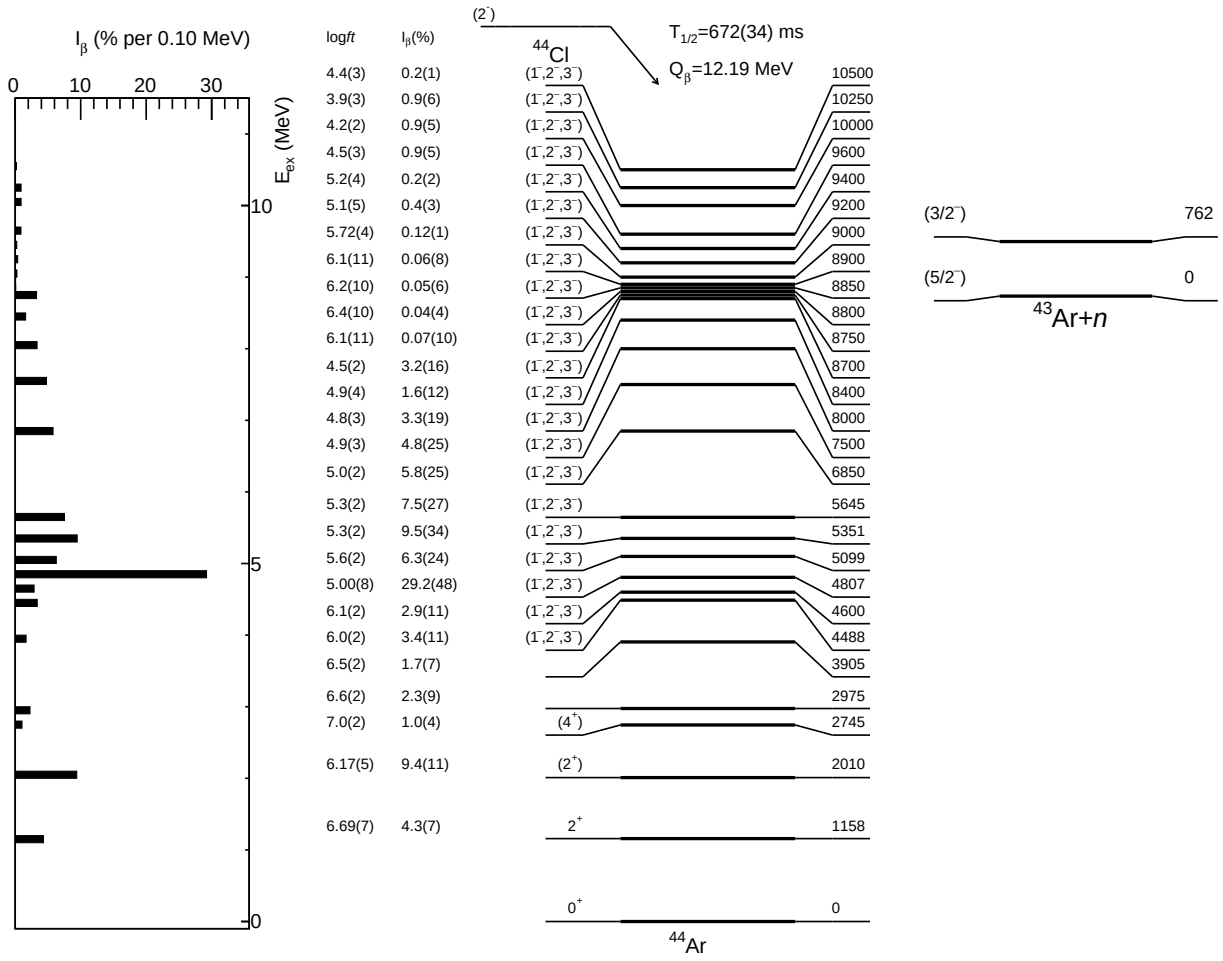

Figure 5.6: The decay scheme for ^{44}Cl as measured by MTAS.

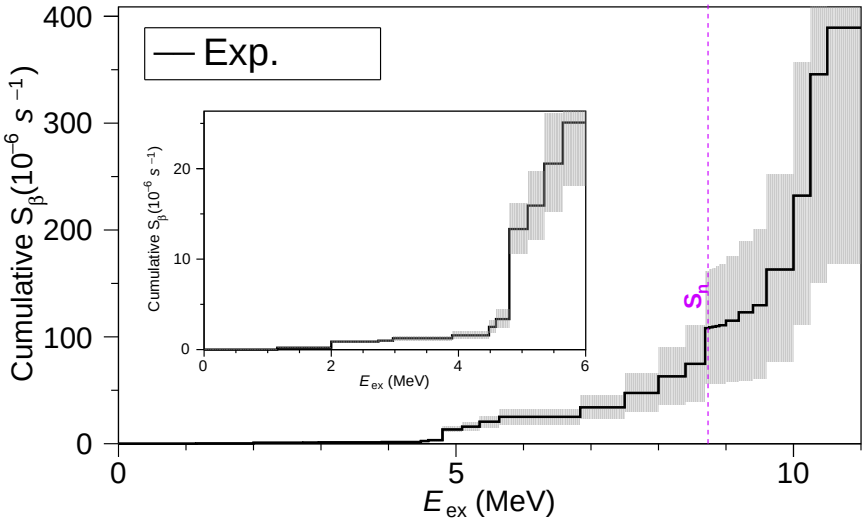

Figure 5.7: The cumulative β-decay strength for ^{44}Cl, with the inset plot zoomed into the range of previous β-decay measurements, < 6 MeV. The neutron separation energy, $S_n = 8.73$ MeV is shown as the purple dashed line.

Table 5.2: Measured half-life values for ^{45}Cl in both focal planes compared with previous literature values. The number of β-decays, N_β, in the analysis window of 1500 ms since the implantation is also reported for each focal plane.

$t_{1/2}$ (ms)	Reference	N_β
451 ± 14	E21069A FDSi FP1	131405
439 ± 9	E21069combined FDSi FP1	282806
439 ± 15	E21069B FDSi FP2	72756
400 ± 43	Sorlin, et al. [66]	
420 ± 30	Winger, et al. [62]	
513 ± 36	Bhattacharya, et al. [50]	

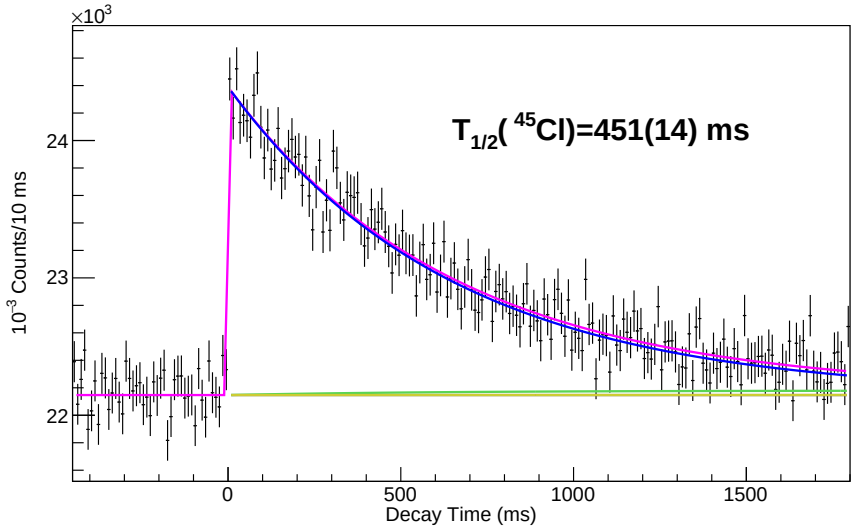

Figure 5.8: Decay curve for ^{45}Cl fit using the Bateman equation.

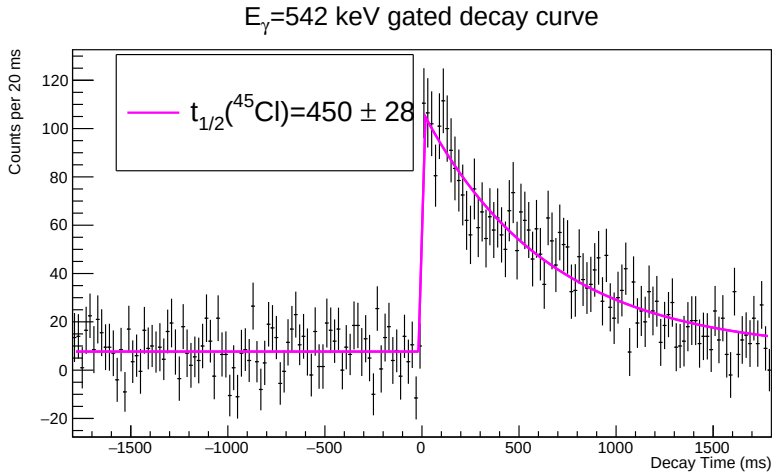

Figure 5.9: Decay curve for ^{45}Cl gated by the 542 γ-transition associated with the first excited state in ^{45}Ar.

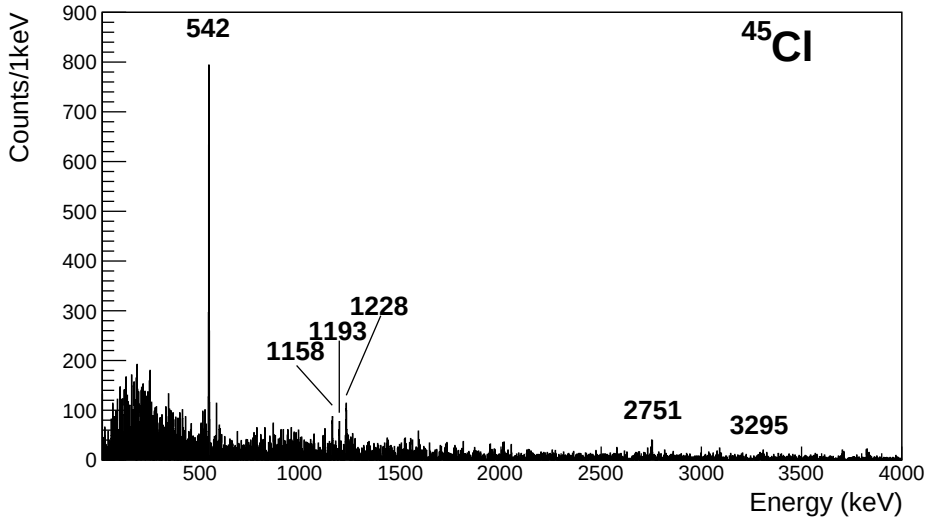

Figure 5.10: The negative-time subtracted HPGe discrete γ-ray spectrum for ^{45}Cl.

routes that transition through the first excited state. These decay branches are shown by the 2752 and 1524 keV transitions in the gated spectrum shown in Figure 5.11, going through the 542 and 1771 keV states, respectively. At higher energy in Figure 5.11, a new transition is seen at 4516 keV, representing the de-excitation from a state at 5058 keV.

With more neutrons inside a nucleus comes a higher probability of neutron emission following β-decay. ^{45}Cl has previously been measured to be a β-delayed neutron emitter, but corresponding neutron energies are unreported. The energy of these neutrons is measured with the NEXTi array via the time-of-flight method, and the time-of-flight spectra are shown in Figure 5.12. The top panel (a) shows the neutron singles, while the lower two panels are gated on γ-rays with E_γ = 1158 and 2011 keV, respectively. These are the lowest two excited states in ^{44}Ar, which can be populated following neutron emission from ^{45}Ar. The γ-gated neutron time-of-flight spectra are fit simultaneously with the neutron singles spectrum to determine which neutrons are a result of β-decay feeding to unbound states, as described in section 4.6.4. Neutrons that feed higher lying states in ^{44}Ar are considered in this deconvolution, such that if the states de-excite through lower excited states, such as the 2^+ state, they are considered in the fit for that state as well. This can be seen by the green (neutrons feeding to the 3rd or higher excited states) and black (neutrons feeding the second excited state) peaks accompanying the blue (neutrons feeding the first excited states) peaks

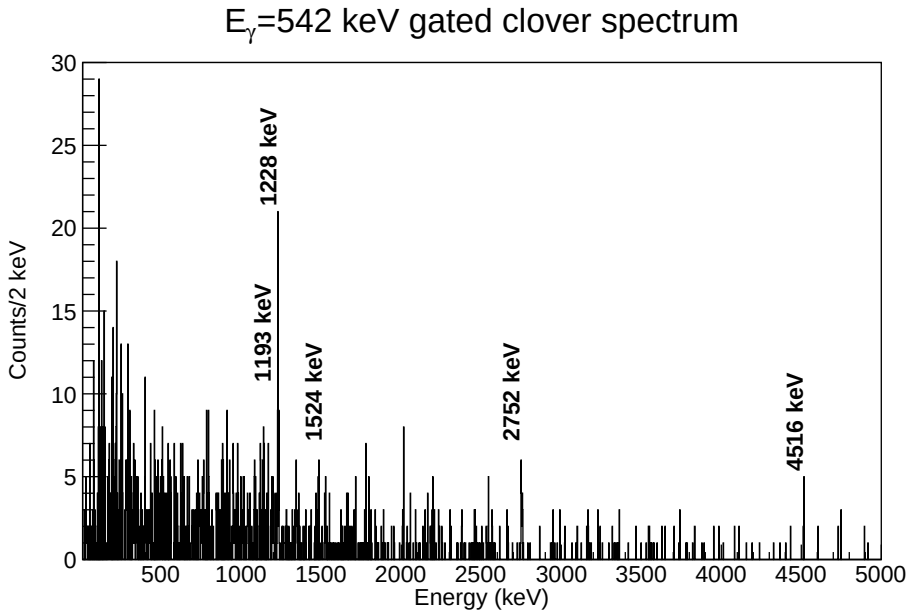

Figure 5.11: The 542 keV-gated clover γ-ray spectrum. A transition is able to be seen at 4516 keV, indicating a new state at 5058 keV. The vertical line indicates the location of the neutron separation energy, $S_n = 5168$ keV.

in the 1158 keV gated neutron spectrum, Figure 5.12(b). Lastly, the red peaks are only seen in the singles spectrum, Figure 5.12(a), because they represent decays to the ground state of ^{44}Ar and thus would not be in coincidence with any γ-rays.

In the neutron spectrum, the most intense peak is near 1 MeV, corresponding to a transition to the ground state of ^{44}Ar from a quasi-resonance in ^{45}Ar at 6210 keV. Higher-lying excited states populated in β decay yield neutrons in feeding both the ground state and excited states, where the first excited state is favored by neutron emission over the second excited state. This is shown by the stronger blue peak at 1.5 MeV in Figure 5.12(b) compared to the smaller black peaks.

To measure the β-decay feeding below the neutron separation energy and below the neutron detection threshold in NEXTi, total absorption spectroscopy is utilized. Figure 5.13 shows the result of the 2D-deconvolution plotted on the energy sum, where each color represents the total feeding to a state and the pink line represents the overall total fit. Neutron unbound states measured by NEXTi were included in the deconvolution, where their β-decay feeding intensities were fixed to match the intensities measured in the first focal plane. States with neutron energies below the NEXTi neutron detection threshold

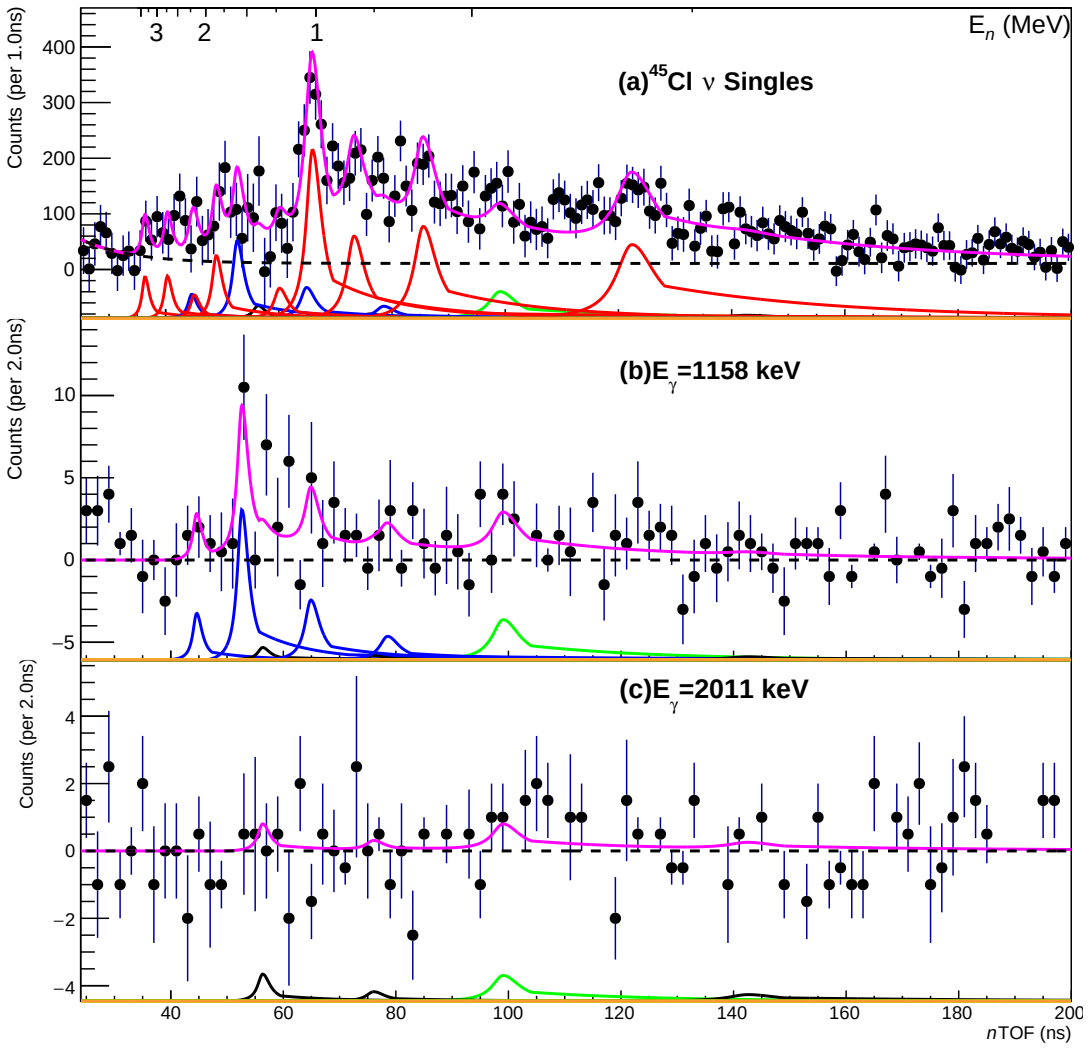

Figure 5.12: Deconvoluted neutron time-of-flight spectrum for ^{45}Cl. (a) represents the ungated neutron-TOF spectrum, (b) are neutrons in coincidence with a 1158 keV γ-ray transition corresponding the the de-excitation of the first 2^+ state in ^{44}Ar, and (c) are neutrons in coincidence with a 2011 keV γ-ray transition from the second excited state in ^{44}Ar. The red peaks show neutrons going to the ground state of ^{44}Ar, the blue peaks show neutrons which go to the first excited state, the black peaks show neutrons going to the second excited state, and the green peaks are for neutrons going to any higher excited state in ^{44}Ar.

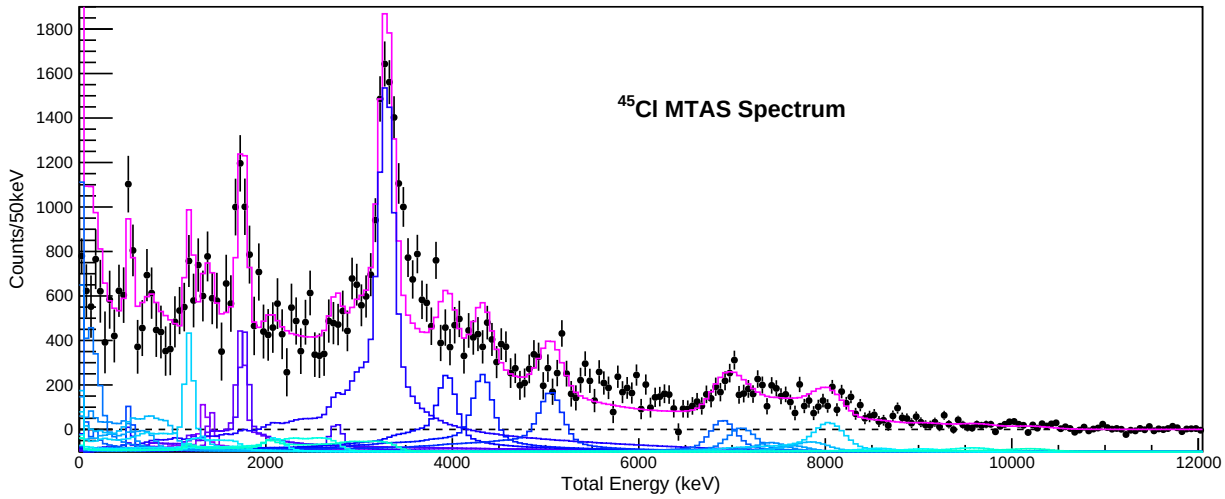

Figure 5.13: The negative-time subtracted MTAS total sum deconvolution using known states and a new state at 5058 keV, and neutron unbound states determined by VANDLE. The fit was performed over a range of 0 to 11 MeV.

were fit unconstrained due to the reliability of MTAS to measure low-energy neutrons. A quasi-resonance at 5250 keV, less than 100 keV above the neutron separation energy, is seen in the MTAS total spectrum shown in Figure 5.13, and another low energy neutron is seen to be in coincidence with the 1158 keV γ-ray measured by the inner module in MTAS, shown as the peak above 8 MeV in Figure 5.14. Due to the Compton scattering of high energy γ-rays, strongly fed states below S_n can also be seen, specifically a new state at 5058 keV, which can also be seen in the total spectrum and 542 keV gated spectrum, shown in Figure 5.15. Also in the total energy spectrum gated on the 542 keV γ-ray in the central module, strong feeding can be seen to the doublet just below 1.8 MeV and the state at 3.3 MeV. This agrees well with the γ-rays measured by DEGAi.

The high efficiency of MTAS makes it ideal for identifying neutron-γ competition for unbound states in a β-decay daughter nucleus. Due to the $3/2^+$ ground state in ^{45}Cl, high-lying states in ^{45}Ar which are fed through β-decay are assumed to be populated via Gamow-Teller decay. This forces the populated states to have either $1/2^+$, $3/2^+$, or $5/2^+$ spin and parities. These states can then be easily connected to the $3/2^-$ first excited state in ^{45}Ar via an E1 transition. This is especially shown for the 5058 keV state which decays through the 542 keV state. By gating on the 542 keV single γ-transition in MTAS, one can

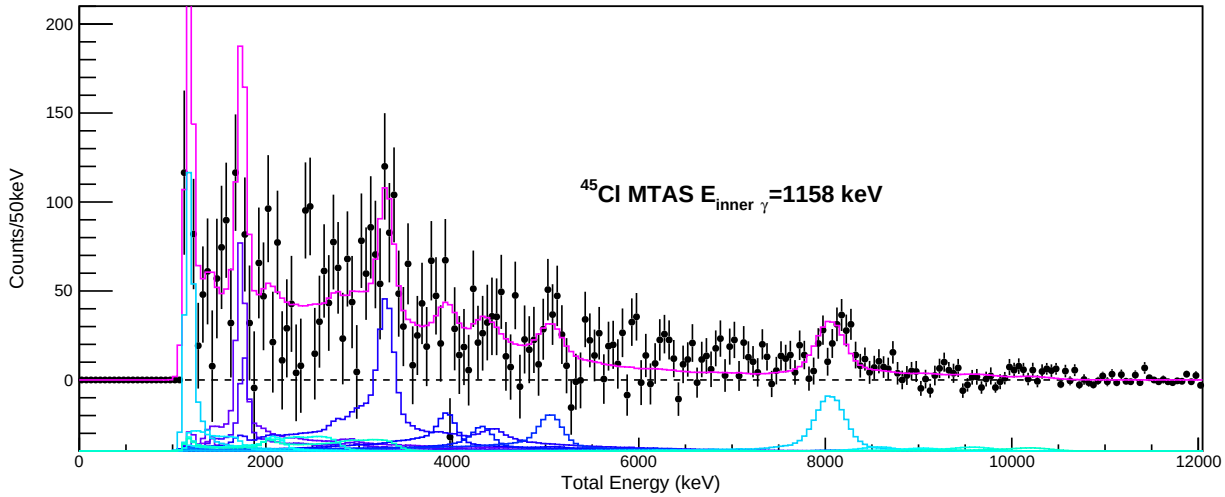

Figure 5.14: The 1158 keV-gated total sum spectrum from MTAS. There is a clear peak above the neutron separation energy, signifying a low energy neutron in coincidence with the first excited state in ^{44}Ar. This neutron is otherwise undetected in VANDLE.

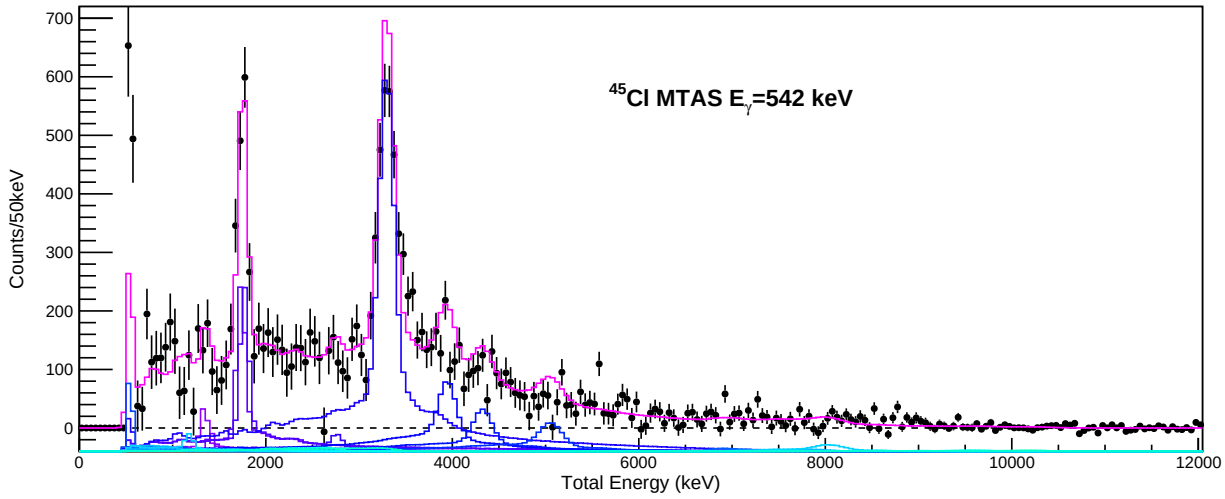

Figure 5.15: The 542 keV-gated total sum spectrum from MTAS. No states are able to be identified above S_n indicating that neutron-γ competition is not seen with this amount of statistics.

investigate the states that decay through the first excited state. Figure 5.15 shows the gates sum spectrum, where there are no clear states above S_n.

The β-feeding intensities to the 10 bound excited states in ^{45}Ar along with the 10 quasi-resonances above S_n are shown in Figure 5.16. The known or expected spin-parities are also listed with the log ft values for the decays. It can be seen that the most intense decay feeding is to the 3295 keV, $5/2^+$ state, which then decays via multiple different paths to the $7/2^-$ ground state. Intense feeding to the $5/2^+$ state is indicative of a $3/2^+$ ground state for ^{45}Cl, opposing the previously assumed $1/2^+$ ground state predicted by shell model calculations. There is also significant feeding near S_n to the 5058 keV state and to neutron unbound states above 5400 keV. With an undetectable amount of neutron-γ competition, the neutron branching ratio, $P_n = 37 \pm 13\%$, is larger than previously reported values of $24 \pm 4\%$ [66] and $28 \pm 9\%$ [123]. Compared to recent FDSi work, the larger P_n in this work is due to the new measurement of low energy neutrons, specifically those in coincidence with the first excited state in ^{44}Ar, which were previously undetected due to the detection threshold of NEXTi. Using the newly measured log ft values, one can extract the β-decay strength distribution, where the cumulative S_β distribution is shown in Figure 5.17. The main features of the distribution are the strong feeding the the 3.3 MeV state and a significant feeding to neutron unbound states.

5.3 Decay of ^{46}Cl

The first measurements of the β-decay of ^{46}Cl were performed at GANIL, with reported half-lives shown in Table 5.3 and β-delayed γ-rays and neutron unbound states from Ref. [69]. The half-lives measured at FDSi, also shown in Table 5.3 and in Figure 5.18, are self-consistent between both focal planes and agree well with the previously reported values. For these analyses, the Bateman equation was used to extract the half-life using literature half-lives for the daughters and granddaughters, with the 1 and 2 neutron branching ratios varied in the error analysis.

The discrete γ-ray transitions measured by DEGAi are shown in Figure 5.19. A wide range of γ-ray energies are observed, with strong intensities for both P_{1n} and P_{0n} nuclei.

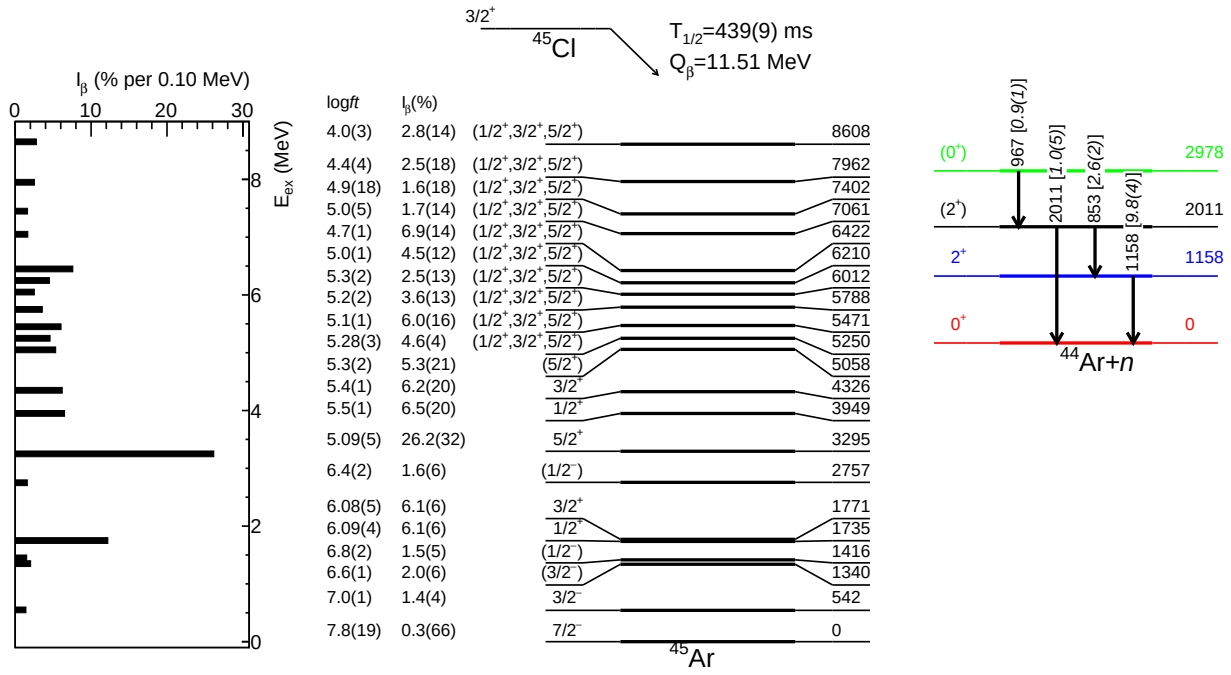

Figure 5.16: A level scheme for ^{45}Ar following the β-decay of ^{45}Cl, including states which are populated in ^{44}Ar following the neutron emission from unbound states of ^{45}Ar. Along with this, the left shows the β-feeding intensity for each measured state.

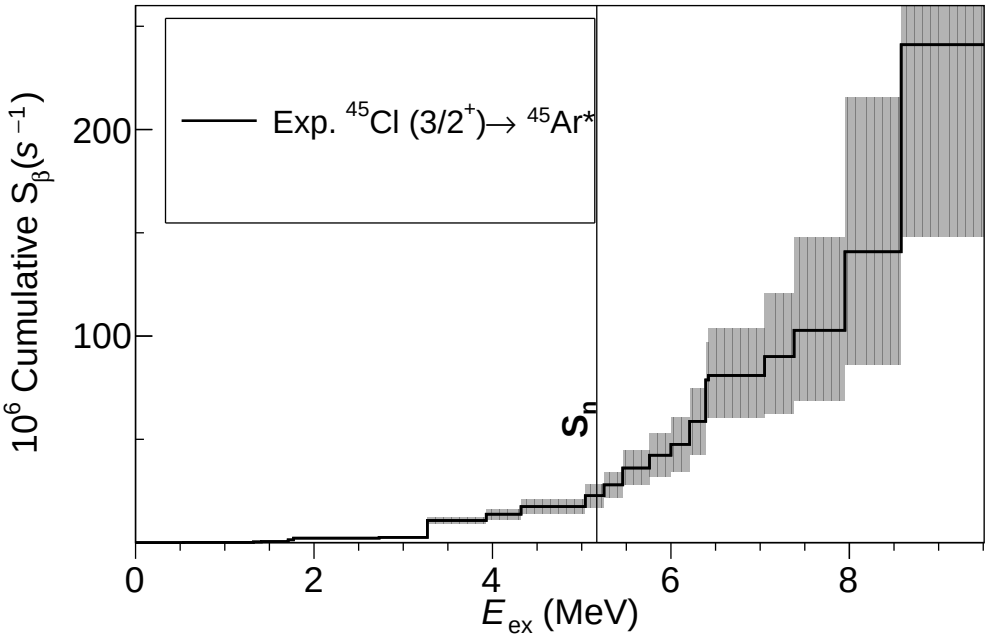

Figure 5.17: The experimentally measured cumulative β-decay strength (S_β) for ^{45}Cl.

Table 5.3: Measured half-life values for ^{46}Cl in both focal planes compared with previous literature values. The number of β-decays, N_β, in the analysis window of 500 ms since the implantation is also reported for each focal plane.

$t_{1/2}$ (ms)	Reference	N_β
216 ± 23	E21069combined FDSi FP1	84434
253 ± 64	E21069B FDSi FP2	19615
223 ± 37	Sorlin, et al. [66]	
232 ± 2	Grévy, et al. [68]	

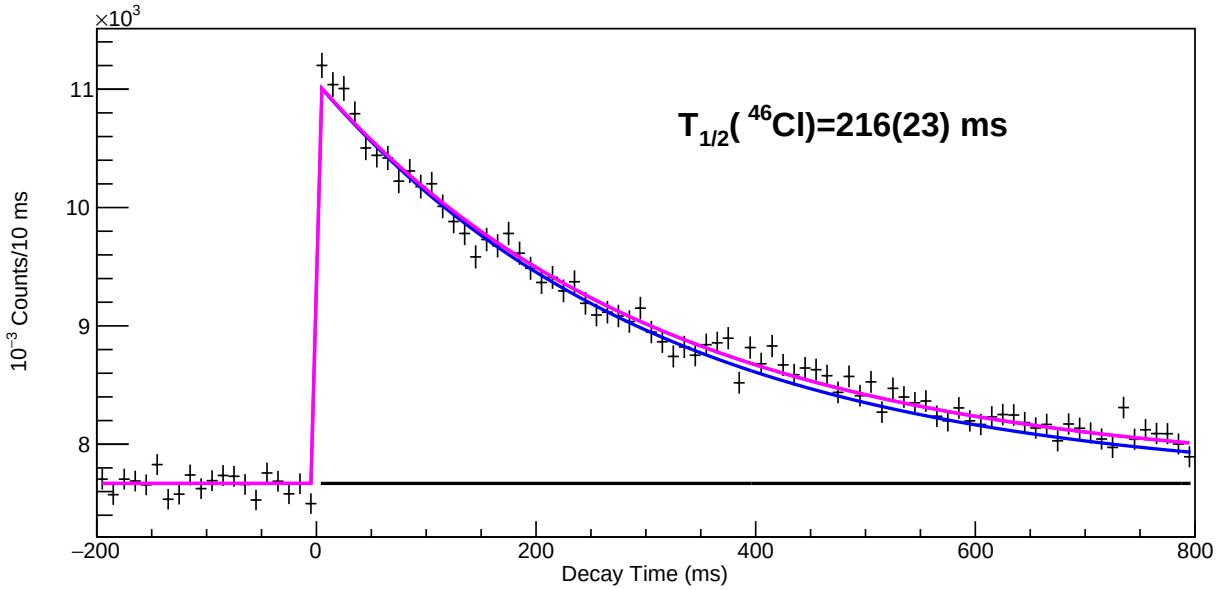

Figure 5.18: Measured decay curve for ^{46}Cl using the combined statistics from e21069a and e21069b.

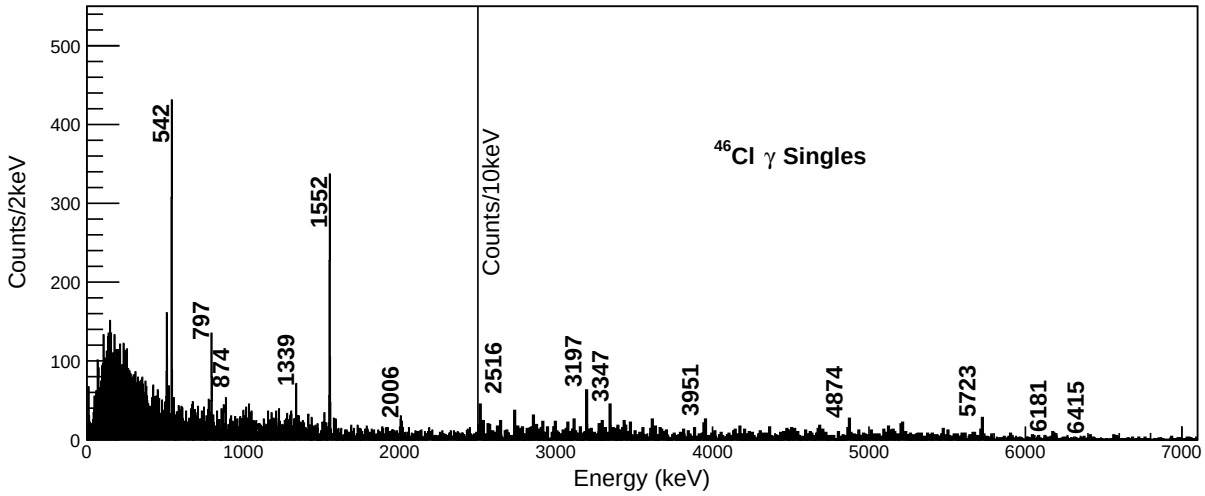

Figure 5.19: The negative-time subtracted HPGe discrete γ-ray spectrum for ^{46}Cl.

Specifically, the first excited state in ^{45}Ar is seen at 542 keV, accompanied by lines at 797 and 874 keV. These latter transitions represent the decays of negative parity $1/2^-$ or $3/2^-$ states in ^{45}Ar through the first excited state to the ground state. Due to electromagnetic selection rules, these states can also decay directly to the ground state, as highlighted by the 1339 keV line strongly shown in Figure 5.19. Due to their negative parity, these states were populated significantly less than other nearby states in the decay of ^{45}Cl, but instead, the negative parity states are favored in neutron emission from excited states in ^{46}Ar populated by GT transition from ^{46}Cl and thus are also negative parity allowing for $l = 0$ neutron emission. Alternatively, the first excited state in ^{46}Ar is at 1552 keV and is measured by the $2^+ \rightarrow 0^+$ transition shown in Figure 5.19 as the second most intense line. The previous measurement by Mrazek demonstrated that many high-lying states are fed in the decay of ^{46}Cl, where these states normally either decay through the first or second excited state with a single large energy γ-transition. In the region above 2500 keV, Figure 5.19 identifies high energy transitions, many of which were previously reported and in agreement with Mrazek. These large transitions are likely due to electromagnetic selection rules when decaying from a negative parity state populated via a GT transition, to the low-lying 2^+ state, indicating either $E1$ or $M2$ transitions. Yet, due to low statistics, $\gamma - \gamma$ coincidences were unable to identify the specific decay patterns for individual transitions.

Neutron unbound states populated in β-decay are candidates for β-delayed neutron emission. With the identification of the first excited state in prompt coincidence with the β decays of ^{46}Cl, the parent nucleus is confirmed to be a strong neutron emitter. Using the NEXTi array, neutron energies can be measured, possibly in coincidence with γ-rays, to construct the decay feeding intensities to neutron unbound states. Figure 5.20 shows the neutron time-of-flight deconvolution measured by NEXTi in singles, in coincidence with the 542 keV γ-ray, and in coincidence with the 798 keV γ-ray in parts (a), (b), and (c), respectively. Higher energy γ-transitions related to ^{45}Ar were also taken into account during the deconvolution, but the neutron-γ coincidence is not shown in the figure. Immediately, it can be seen that the numerous medium energy states, between 0.5 and 2 MeV, in ^{45}Ar leads to a wide variety of neutron energies, shown as a continuous neutron ToF spectrum. The two most prominently fed states via neutron emission are the first excited state, shown as the blue curves, and the second excited state, shown as the black curves. The other colors represent additional states to which the neutron arrives in ^{45}Ar, at a smaller frequency. This deconvolution yields a total of 6 neutron emitting quasi-resonances, which is increased from the 4 reported by Mrazek [69]. The 4 previously reported quasi-resonances are found to be in agreement with the 4 lower lying quasi-resonances measured in this work, while the other two higher-lying quasi-resonances are new.

Using the known levels measured in the first focal plane for neutron bound and unbound states, their responses in MTAS can be simulated and fit to experimental data, yielding the β-decay feeding intensities for the decay of ^{46}Cl. Figure 5.21 shows the result of the deconvolution of the MTAS spectrum. Due to gaps in the known levels and responses from MTAS, additional states were included at 7300, 8300, and 9200, all of which were input to be γ decaying states. Using single transitions from DEGAi and feeding patterns determined by MTAS, the new state at 7300 keV can instead be interpreted to be a state at 7265 keV which decays via a 3197 keV γ-ray to the 4068 keV third excited state in ^{46}Ar, demonstrating a self-consistent analysis between the first and second focal planes at FDSi.

Furthermore, by gating on the 1552 keV single γ-ray transition in the central module and looking at the total sum spectrum, shown at the top of Figure 5.22, the states fed in β-decay which de-excite through the first excited state are isolated. Once isolated, the high-lying

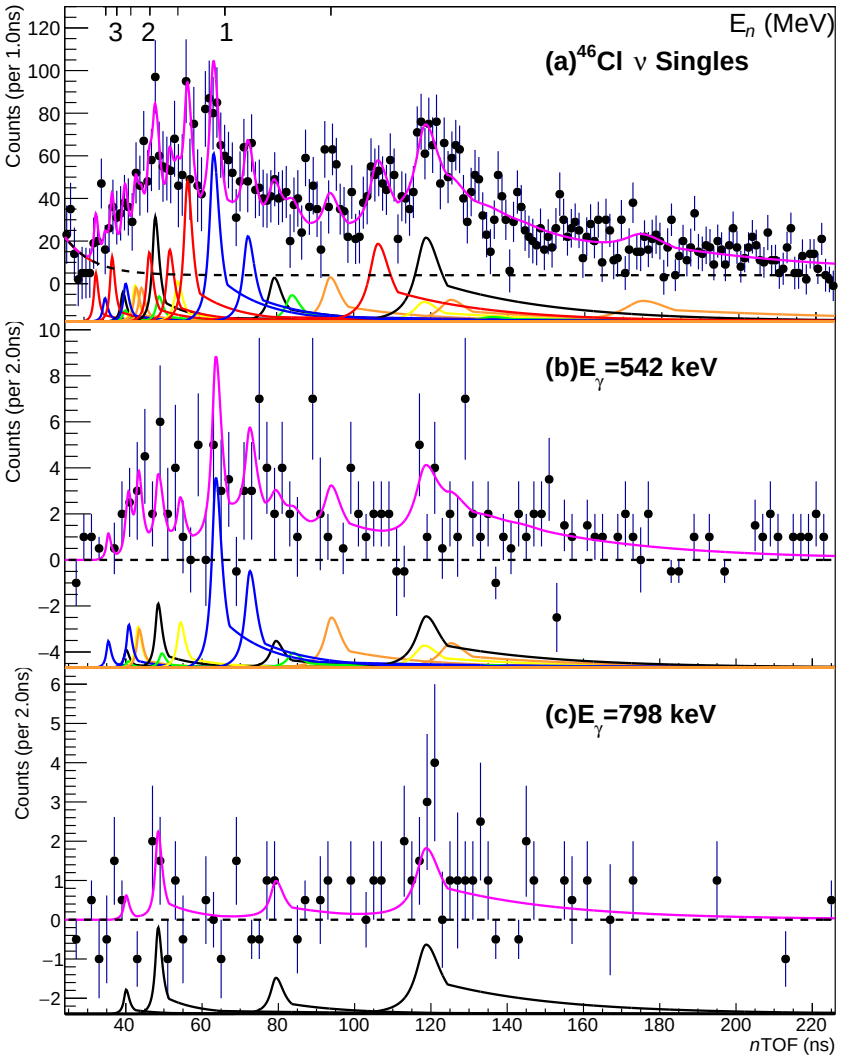

Figure 5.20: Neutron time-of-flight deconvolution from the decay of ^{46}Cl.

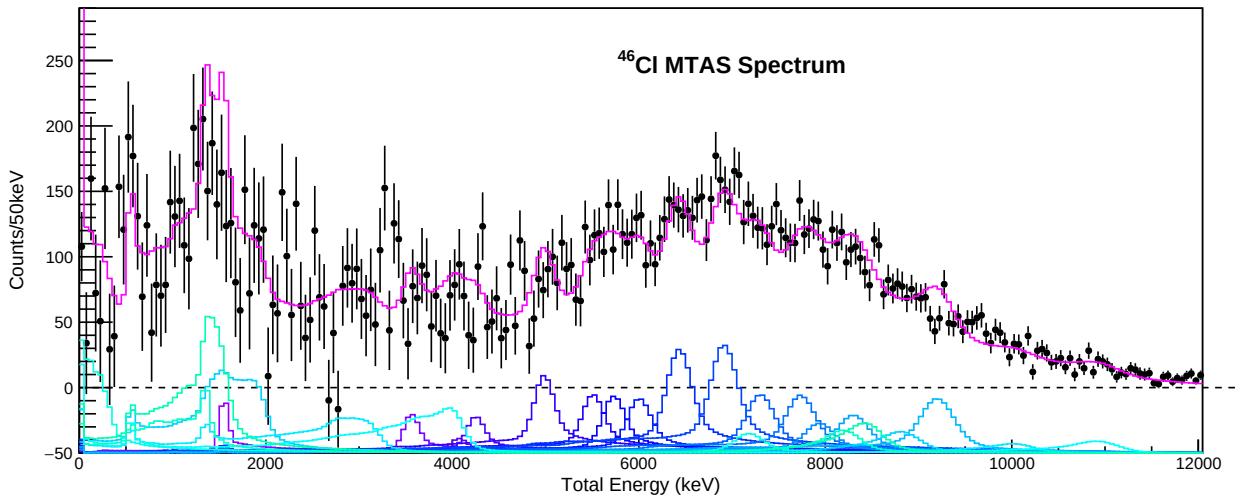

Figure 5.21: The total sum spectrum in MTAS for the decay of ^{46}Cl, where each curve represents the MTAS response to the feeding to an individual state.

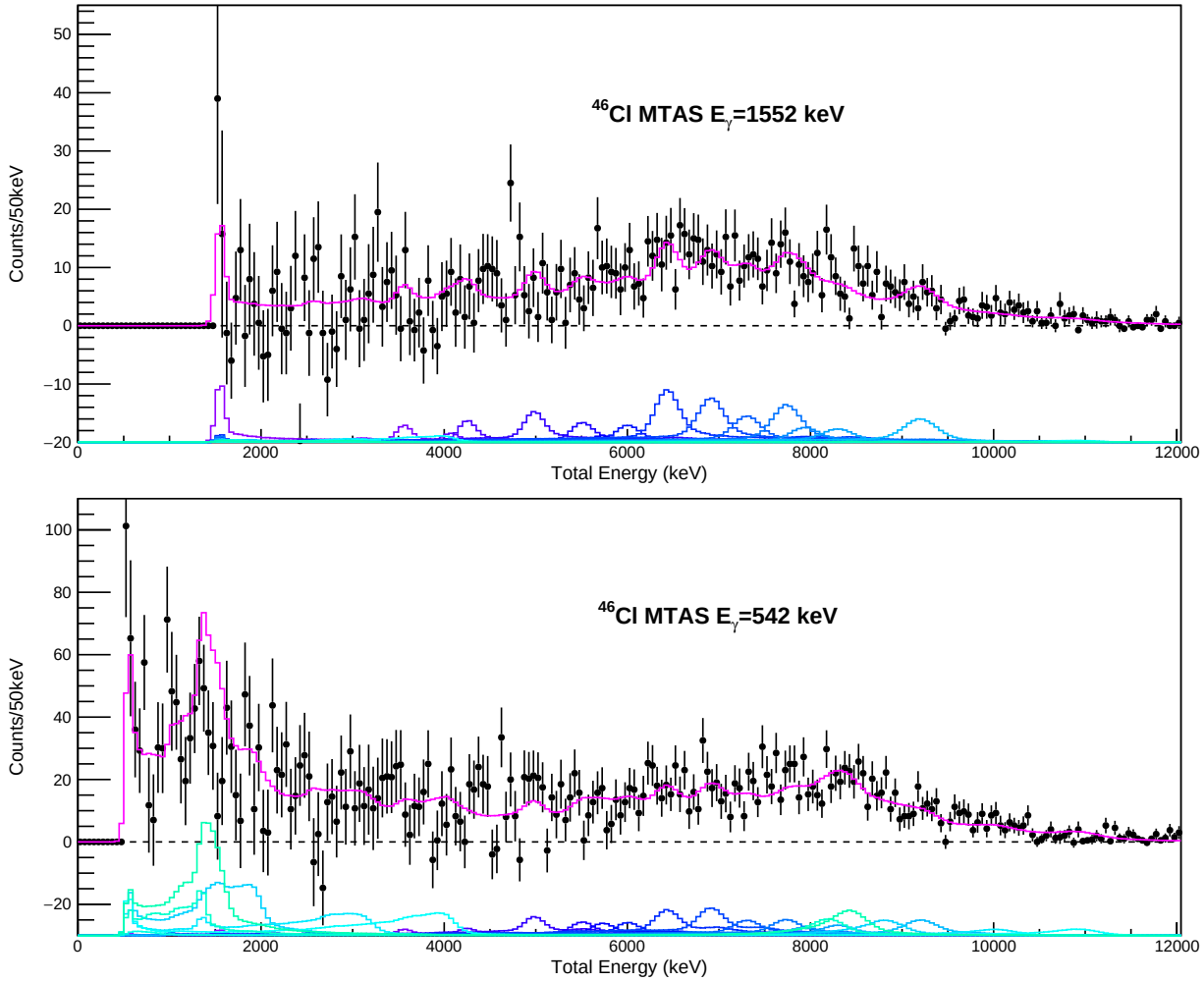

Figure 5.22: (Top) The MTAS total sum spectrum gated on 1552 keV γ-ray associated with the first excited state in ^{46}Ar measured in the central module. (Bottom) The MTAS total sum spectrum gated on 542 keV γ-ray associated with the first excited state in ^{45}Ar measured in the central module.

on the results from the first focal plane, which was able to isolate neutron unbound states, and which states in ^{45}Ar were most fed.

Combining the results from the first and second focal planes, the β-decay feeding intensities can be measured for ^{46}Cl. Figure 5.23 shows the results, including the full level scheme of ^{46}Ar and a plot on the left showing the feeding, I_β. Using the logft values for each state, the β decay strength distribution is extracted and shown as the cumulative curve from 0 to 13 MeV in Figure 5.24. The β-decay feeding is dominated by transitions to states between 4.5 and 10.5 MeV, where no individual transition has a larger feeding than the rest. This is different from what is seen in the decays of ^{44,45}Cl where there is a single lower energy state which takes most of the feeding. The result of this spread in feeding is a more continuous, slowly rising cumulating S_β up to 9.5 MeV, where the strength begins to increase more drastically.

5.4 Decay of ^{47}Cl

Previous measurements of the decay of ^{47}Cl yielded only a half-life of 101 $\pm$ 6 ms [68], as shown in Table 5.4 and Figure 5.25. This work combines data taken in both parts of experiment e21069 at FRIB to further analyze the decay of ^{47}Cl through the complete decay spectroscopy technique. Firstly, the half-life of ^{47}Cl, as measured by the work, is in good agreement with the previously reported value.

The individual γ-ray transitions, measured by DEGAi, can then be investigated, shown in Figure 5.26 where the strongest line is at 1552 keV, representing the de-excitation of the first 2^+ state in ^{46}Ar. Such a strong line indicates a large amount of β-delayed neutron emission in the decay. Above 2 MeV, transitions can be seen representing γ decays of highly excited states in ^{46}Ar to the 2^+ state following neutron emission. For these states to be populated following neutron emission, high energy states in ^{47}Ar must first be populated in β-decay. Due to the smaller phase space, these states would likely be a result of GT transitions. At lower energies, a transition can be seen at 1229 keV, previously reported by Bhattacharyya [83] and Gade [85], for the de-excitation of a $5/2^-$ state to the $3/2^-$ ground state in ^{47}Ar. Along with this, a smaller transition can be seen from a state at 1207 keV,

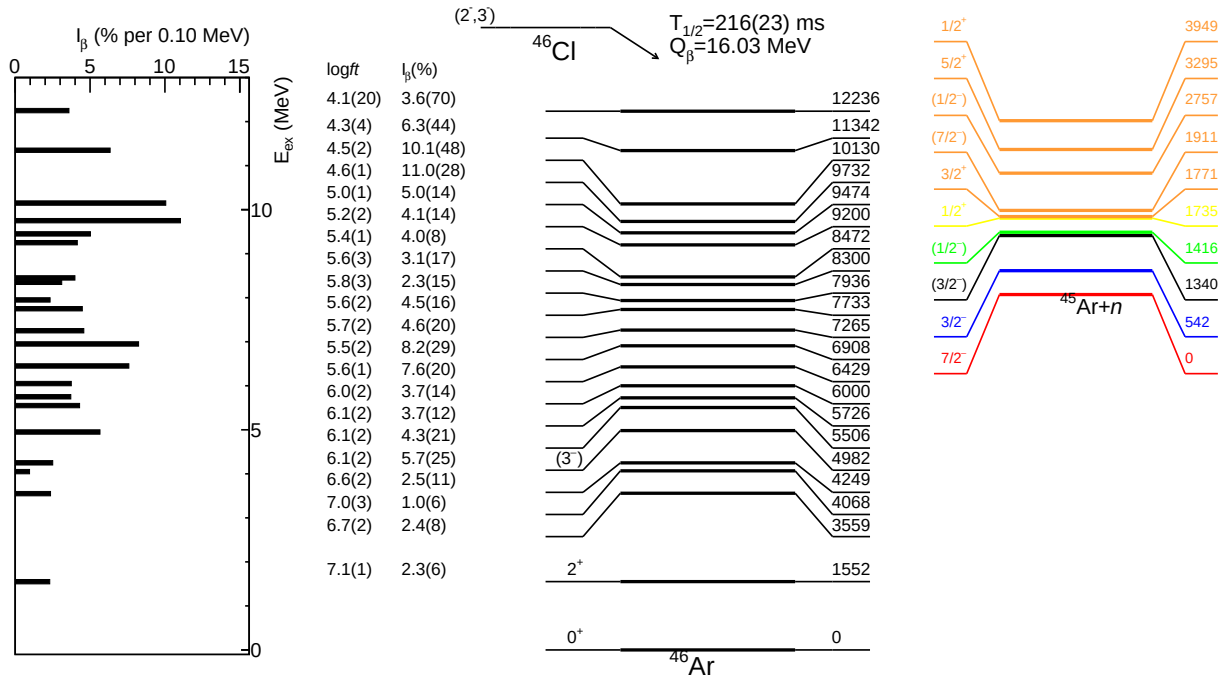

Figure 5.23: A level scheme for ^{46}Ar following the β-decay of ^{46}Cl, including states which are populated in ^{45}Ar following the neutron emission from unbound states of ^{46}Ar. Along with this, the left shows the β-feeding intensity for each measured state.

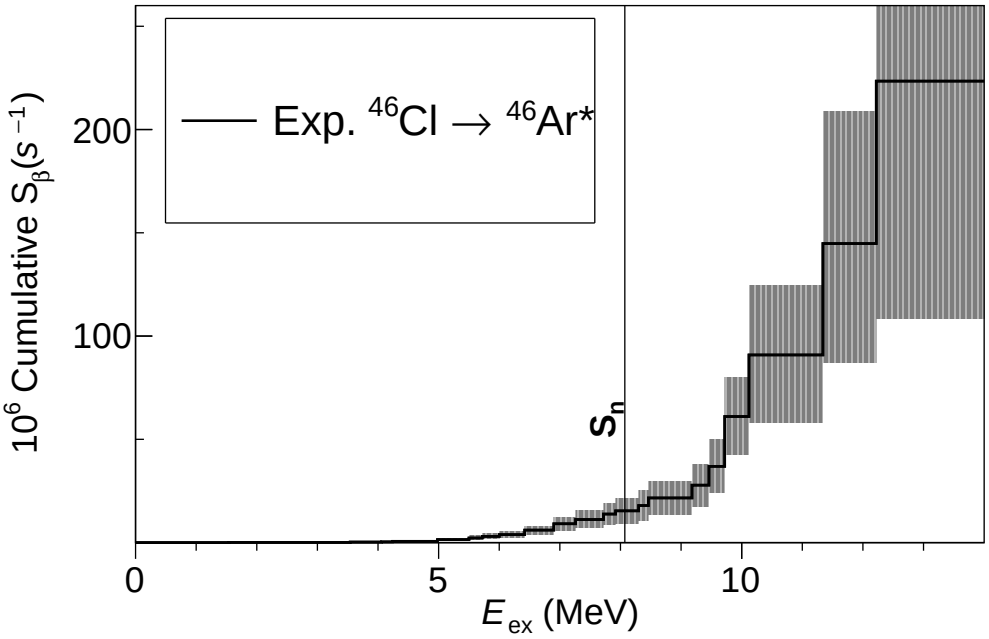

Figure 5.24: The cumulative β-decay strength distribution for ^{46}Cl, measured using both the first and second focal planes of FDSi.

Table 5.4: Measured half-life values for ^{47}Cl in both focal planes compared with previous literature values. The number of β-decays, N_β, in the analysis window of 300 ms since the implantation is also reported for each focal plane.

$t_{1/2}$ (ms)	Reference	N_β
100 ± 20	E21069combined FDSi FP1	28692
94 ± 56	E21069B FDSi FP2	7317
101 ± 6	Grévy, et al. [68]	

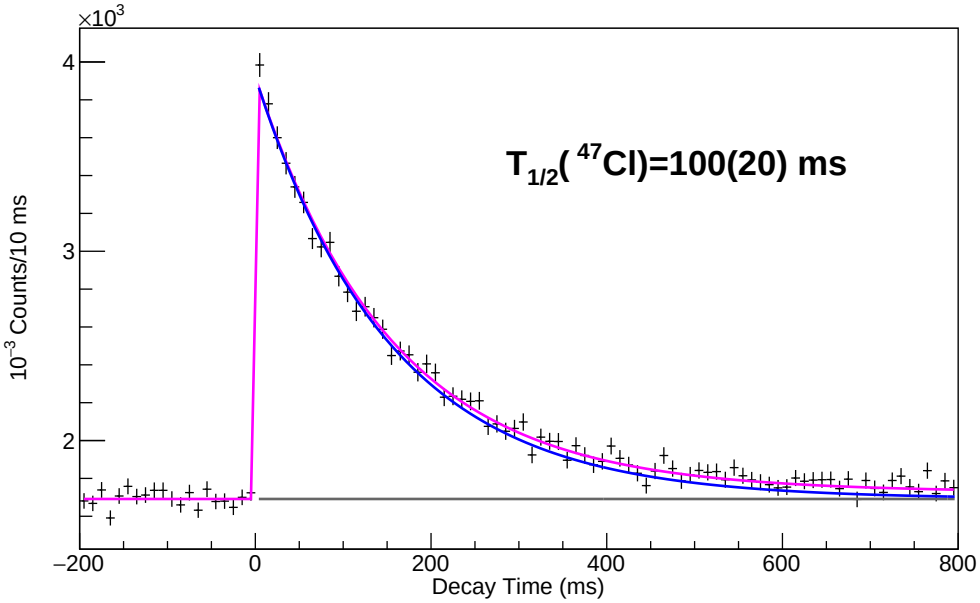

Figure 5.25: The decay curve for ^{47}Cl, where the black line represents the constant background, the blue line is the main decay and the pink line is the total fit including P_{xn} daughters and granddaugters.

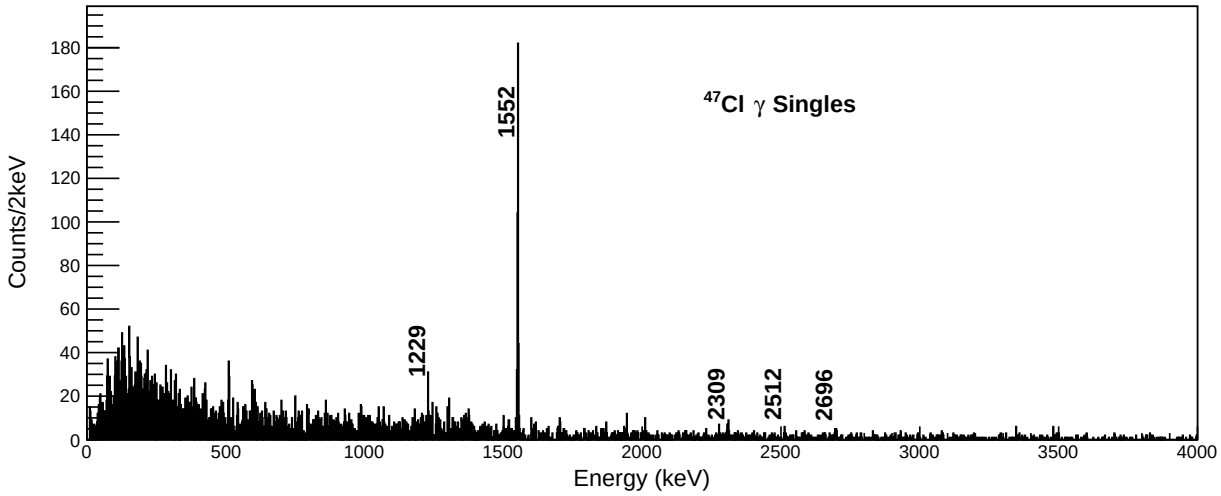

Figure 5.26: The high-resolution γ-ray spectrum corresponding to the decay of ^{47}Cl, measured with DEGAi.

postulated to be $1/2^-$ by Bhattacharyya [83]. Both of these lower-lying states would have to be populated either from higher-lying states through a γ cascade or directly from the ^{47}Cl ground state via a FF transition. This transition must be forbidden due to the positive parity $3/2^+$ ground state of ^{47}Cl feeding the two negative parity states.

As stated earlier, many decays of ^{47}Cl result in the population and de-excitation of the 1552 keV first excited state in ^{46}Ar following a neutron emission. Thus when measuring β-delayed neutron emission, neutron-γ coincidence is a necessary tool to extract levels of excited states above S_n. Figure 5.27 shows both the neutron singles spectrum (a) and $E_\gamma = 1552$ keV gated spectrum (b), where many different excited states in ^{46}Ar are fed following neutron emission. This supports the notion that GT transitions in the decay of ^{47}Cl have the ability to populate highly energetic states in ^{47}Ar. The inclusion of excited states in ^{46}Ar above the first excited state, while limited in neutron-γ coincidence statistics, was due to the observation of known γ-rays from higher-lying states in DEGAi. This allows for the reconstruction of the strength distribution to higher energies above the neutron separation energy.

Using the measured neutron energies along with the measured and known γ-decays from low-lying states, the total absorption spectrum from ^{47}Cl can be fit, as shown in Figure 5.28. From this fit, the β-decay feedings can be extracted for the lower-lying levels, predominantly fed through FF transitions. In this deconvolution, the neutron unbound states were limited

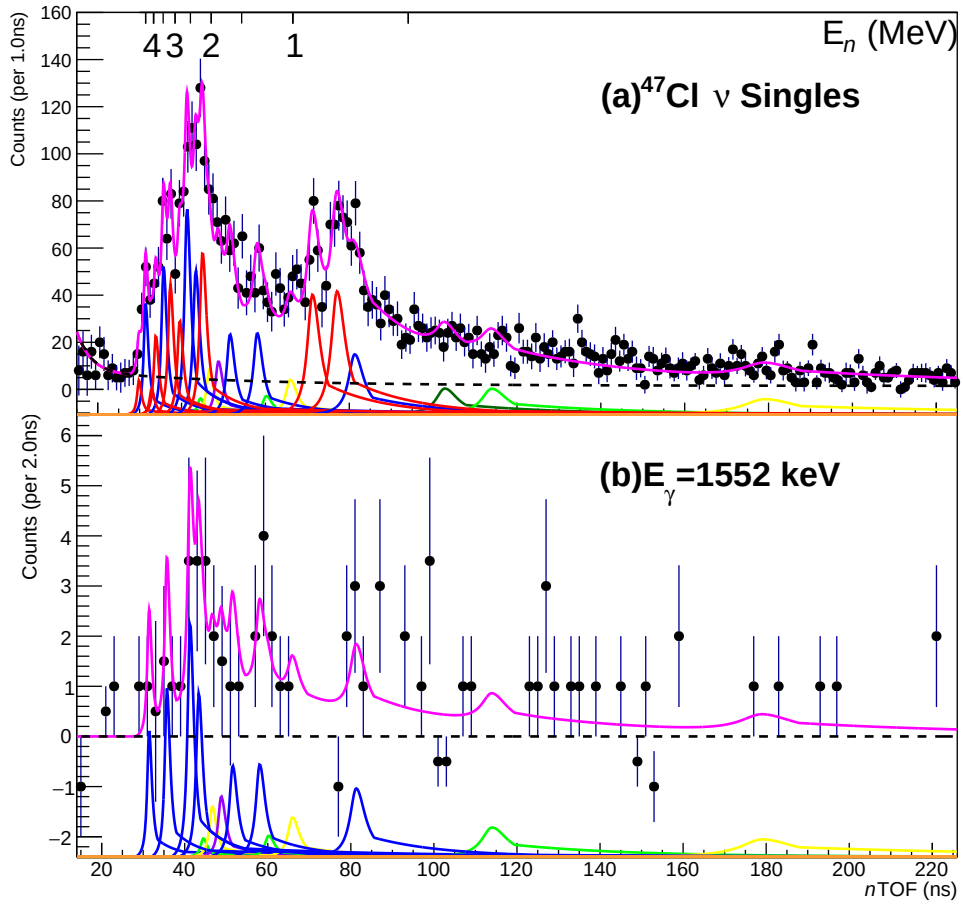

Figure 5.27: The neutron time-of-flight deconvolution from the decay of ^{47}Cl.

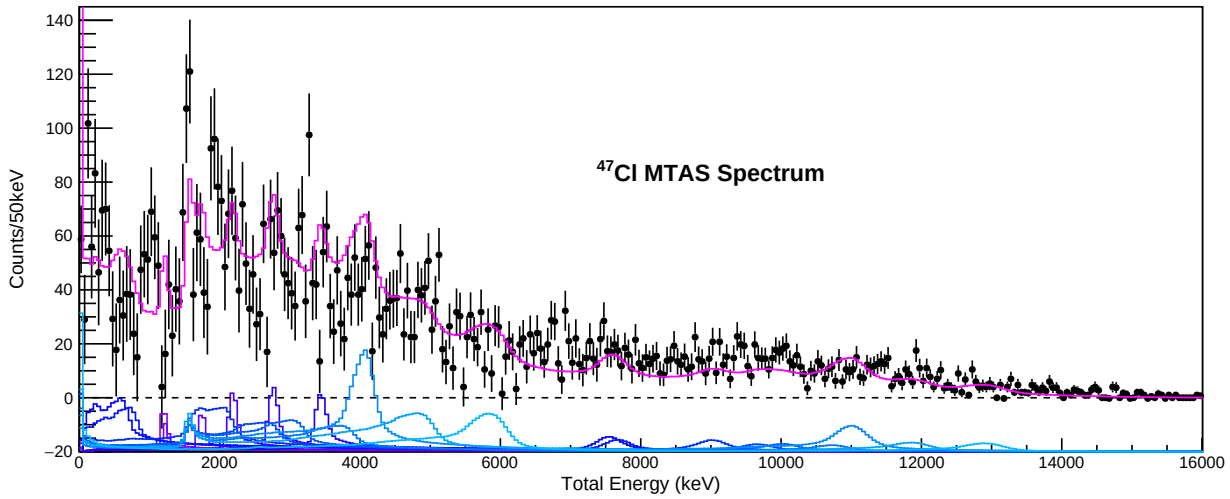

Figure 5.28: The deconvoluted total sum spectrum in MTAS for the decay of ^{47}Cl, where each curve respresents the MTAS response to the feeding to an individual state.

based on the measurements by the NEXTi array. Although the statistics are low in the MTAS spectrum, overall the agreement is good. From this, the lower-lying states can be fit unrestricted, even though the high-lying states produce structures at lower energies.

With the combined results from DEGAi, NEXTi, and MTAS, the β-feeding intensities, shown in Figure 5.29, can be extracted. Due to the low statistics, there are only 9 quasi-resonances above S_n, which take the majority of decay feeding, yielding a $P_n > 70\%$. Only a lower limit can be placed due to the limited statistics and large likelihood of two neutron emission increasing the total number of measured neutrons. The resulting β-decay strength distribution, shown in Figure 5.30, remains low up to nearly 6 MeV before increasing more rapidly. This indicated that the main strength occurs far above the neutron separation energy.

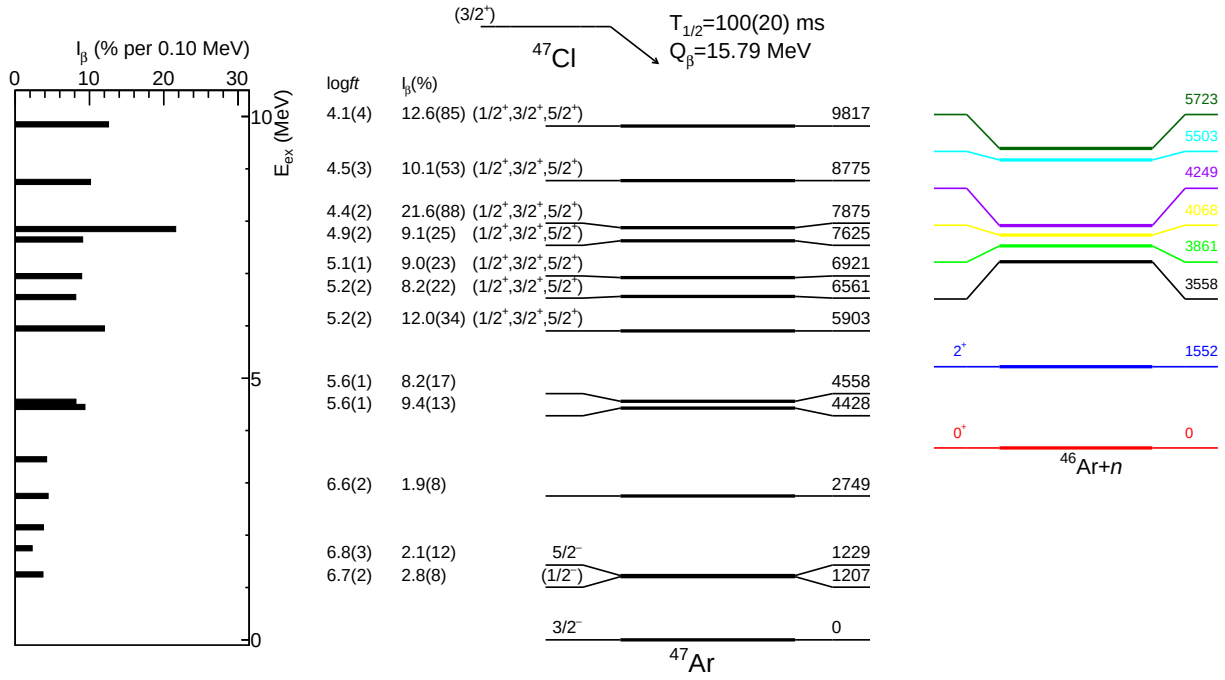

Figure 5.29: A level scheme for ^{47}Ar following the β-decay of ^{47}Cl, where limited statistics yield large errors on the feeding to individual states.

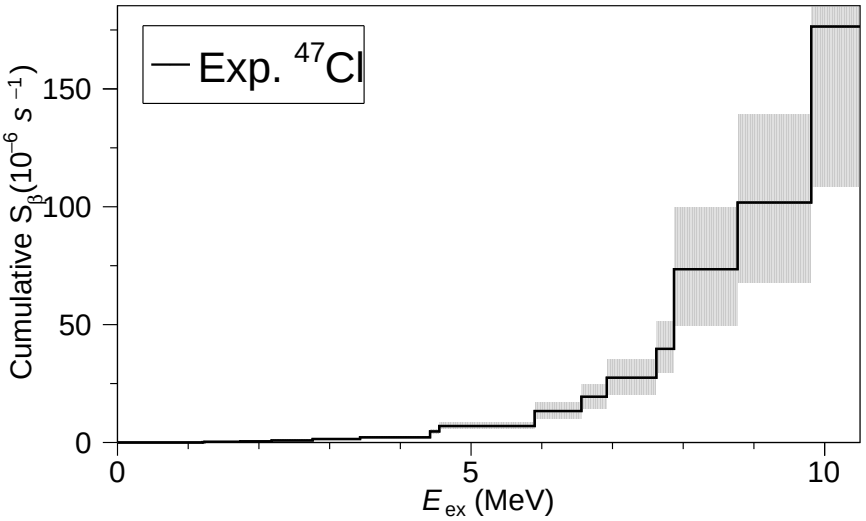

Figure 5.30: The cumulative β-decay strength distribution for ^{47}Cl, measured using both the first and second focal planes of FDSi.

Chapter 6

Discussion

Calculations of β-decay transitions in the neutron-rich $N = 28$ region rely on the inclusion of multiple major shells to properly describe the general features of decay strength distributions. With neutrons populating the pf shell and protons populating the sd shell, the SDPF-MU interaction, and more recently the SD-PF-SDG interaction [28], provide the necessary orbitals for decay calculations. This section focuses on the comparison between theoretical calculations and experimental measurements for the decay of chlorine isotopes.

6.1 Theoretical Predictions for the decay of ^{44}Cl

Beginning with the decay of ^{44}Cl, the decay strength shown at the end of section 5.1 is compared to the Gamow-Teller transitions calculated using the SD-PF-SDG interaction, shown as the red in Figure 6.1, along with GT and FF calculations from the nominal SDPF-MU (green dashed line) and modified SDPF-MU (blue solid line) interactions. Starting with the top plot in Figure 6.1, the experimental decay strength up to 6 MeV is characterized by a large step at 4.8 MeV, followed by a continuous increase above 5 MeV. Proceeding the step, the decay strength is mostly flat with small steps due to forbidden transitions, such as the decay from the 2^- ground state of ^{44}Cl to the 2^+, first excited state, in ^{44}Ar. The large step corresponds to the decay via a GT transition to one of the lowest-lying negative parity states. This specific state is an ideal test for models as it probes both the energy and decay strength to a specific state. SD-PF-SDG calculations not only under predicts the energy of the state

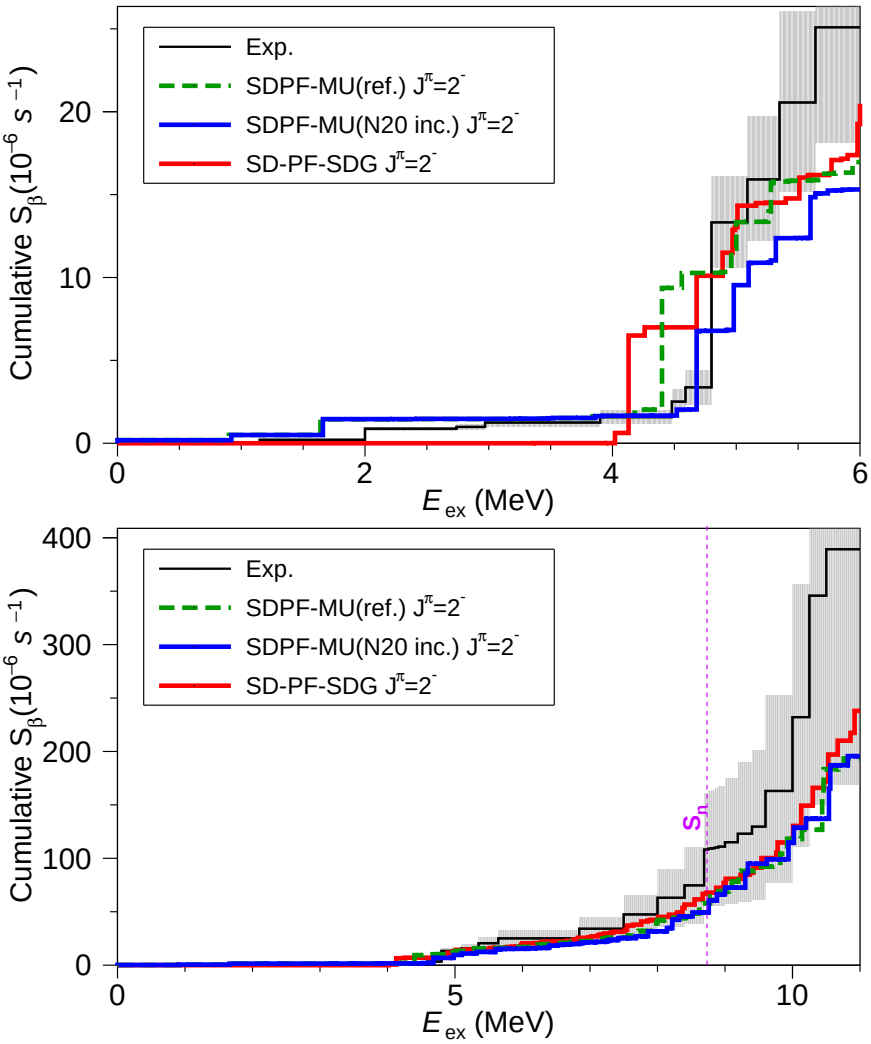

Figure 6.1: The experimental β-decay strength distribution, S_β, for ^{44}Cl (black line) compared to shell model calculations from the nominal SDPF-MU interaction (green dashed line), modified SDPF-MU interaction (solid blue line), and SD-PF-SDG interaction (GT only, red line).

and decay strength to the 1^- state. Also predicting strong decay strength to a 1^- state, the nominal SDPF-MU interaction gets closer to the measured decay energy, but also still under predicts the decay strength to the state. In an effort to replicate the correct energy of the state, the $N = 20$ shell gap was modified in the SDPF-MU interaction by a 1 MeV increase. This yielded an energy that is more consistent with the experimental value, but the decay strength is reduced, rather than increased. While the trend of a single step is produced by all calculations, the location and decay strength to the state does not match experimental data. Investigating the decay to higher lying states, shown in the bottom of Figure 6.1,

theoretical predictions somewhat under predicts the cumulative strength, but the trend of a gradually increasing strength up to 8 MeV in experimental data is well reproduced in the theoretical calculations. Then, the experimental strength grows more rapidly above 8 MeV, which is also well predicted by the calculations. This indicates that while the calculations of individual states are not precise, theoretical calculations can predict the density of states in ^{44}Ar along with the decay strength to those states.

6.2 SDPF-MU Predictions along $N = 28$

The β-decay of ^{45}Cl is important, as it can give insight into the transition from the spherical ^{48}Ca to the deformed ^{42}Si, along the $N = 28$ isotones. Similar to the decay of ^{44}Cl, the decay of ^{45}Cl experimentally has strong decay feeding to the 3.3 MeV state, known to be $5/2^+$. This state is not accessible via GT transitions from a $1/2^+$ ground state, as was originally predicted and calculated using the SD-PF-SDG interaction, shown as the red line in Figure 6.2(a). Most notably, the large interaction favors decays to lower-lying $1/2^+$ and $3/2^+$ states, as shown by the large increase in decay strength. Instead, this step in decay strength lies higher up and is slightly reduced in comparison, which is predicted by the nominal SDPF-MU interaction calculations with a $3/2^+$ ground state, shown as the green dashed line. This change in from a prediction of a $1/2^+$ ground state to the experimentally deduced $3/2^+$ ground state of ^{45}Cl is directly related to the degeneracy of the proton $d_{3/2}$ and $s_{1/2}$ orbitals. As mentioned earlier, the $d_{3/2}$ orbital is strongly affected by the filling of the neutron $f_{7/2}$ orbital, exemplified by the inversion of the $3/2^+$ and $1/2^+$ ground states in potassium isotopes. As a $N = 28$ nuclei, it can be expected that the influence of the $f_{7/2}$ neutrons would be at its maximum and would produce a $1/2^+$ ground state in ^{45}Cl. Yet experimental data rebukes this, with the ground state instead being $3/2^+$. With fewer protons in the *sd* shell, ^{45}Cl is predicted to have a much smaller gap between the proton $s_{1/2}$ and $d_{3/2}$ orbitals, as discussed earlier. Still, the assignment of a $3/2^+$ ground state by Bhattacharya [50] and reaffirmed with the decay strength can help predict the ground state for more exotic nuclei, such as ^{47}Cl, where it was originally predicted to have stiff competition between the $1/2^+$ and $3/2^+$ states, but instead should also have a $3/2^+$ ground state.

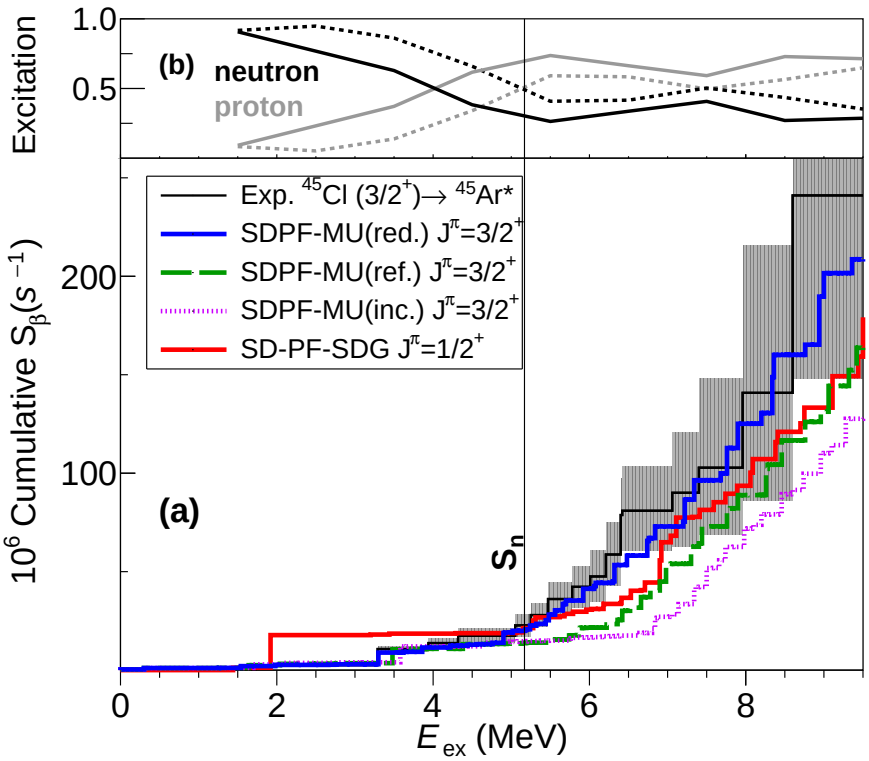

Figure 6.2: (a) A comparison of experimental S_β (black) to theoretical predictions using the SD-PF-SDG [28] (red) and SDPF-MU (blue, green, pink) interactions for the decay of ^{45}Cl. In this figure, SDPF-MU(dec.) represents calculations done with the $Z = 20$ shell gap decreased by 1 MeV (blue) and SDPF- MU(inc.) $Z = 20$ shell gap increased by 1 MeV (pink dotted), compared to the reference gap shown by SDPF-MU(ref.) (green dashed curve). (b) The number of protons (grey) and neutrons (black) excited from the sd to pf shell, as a function of energy, for states in ^{45}Ar after β decay. The solid and dashed were obtained with decreased shell gap and reference SDPF-MU interactions, respectively. See text for more details.

Above the first GT step at 3.3 MeV, the cumulative decay strength has a linear trend, steadily increasing up to the detection threshold of 8.5 MeV. The SD-PF-SDG calculations at high energies have two distinct trends with a step in the middle. First, it is predicted that the decay strength would have a slow increase, followed by a larger and more steady increase above the step near 7 MeV. While the experimental strength distribution also has a slight step above 6 MeV, it is not as distinct as the step predicted by the new interaction. This is likely due to the wrong predicted ground state of ^{45}Cl, limiting the number of states that can be populated via GT transitions. For the nominal SDPF-MU calculations with a $3/2^+$ ground state for ^{45}Cl, the strength above 6 MeV closely follows the linear trend

from the experimental data. Yet, in the experimental work, the linear cumulative strength begins closer to 5 MeV instead of above 6 MeV, creating a discrepancy between the SDPF-MU calculations and the experimental data in the region just above the neutron separation energy.

As discussed earlier in Chapter 2, GT decays for neutron-rich chlorine isotopes occur by exciting a neutron from below $N = 20$, leaving a hole, or by populating a proton above $Z = 20$, leaving the residual argon nucleus highly excited. Due to the discrepancy between the experimental cumulative strength distribution and the nominal SDPF-MU calculations, modified SDPF-MU interactions were introduced. Specifically, the size of the $Z = 20$ shell gap was targeted by changing the effective single particle energies for the proton pf orbitals by $+1$ MeV and -1MeV, shown in Figure 6.2(a) by the pink dotted curve and solid blue curve, respectively. Immediately, the reduced proton shell gap is seen to have much better agreement with the experimental distribution, both in the location and strength of the 3.3 MeV GT transition and the shape and scale of the strength distribution above 5 MeV. Moreover, to understand why the decay distribution at high energies is sensitive to πpf orbitals in ^{45}Ar, new variables were constructed by counting the number of protons (neutrons) excited across $Z(N) = 20$, weighted by S_β as a function of excitation energy. This new variable, shown in Figure 6.2(b), represents the excitation mode in the daughter relevant to β-decay predicted by the nominal and reduced $Z = 20$ shell gap SDPF-MU interactions, shown as the dashed and solid lines. In the figure, the black curves represent neutron excitations, where the decay to lower-lying GT accessible states are dominated by the creation of neutron holes in the sd shell, thus filling the proton sd orbitals. This is consistent with previous results from the neutron transfer reaction on ^{46}Ar [73]. In contrast, the proton excitation into the pf shell, shown as the grey curves, increases near S_n and prevails at higher excitation energy. Reducing the $Z = 20$ shell gap mostly impacts the high-energy decay strength, as proton excitations from the sd to pf orbitals require less energy; this allows the GT strength to shift downward in line with the experimental data.

While a 1 MeV reduction for the proton pf orbitals might seem arbitrary and just to match the experimental data, it is important to ensure that the shell model interaction can reproduce other observables in the region, along with the S_β. The reference SDPF-MU shell

model calculations reproduce the closely lying $1/2^+$ and $3/2^+$ states at low energy, with a difference of -351 keV, compared to 127(6) reported by Gade [51], even though the energy sequence is not correct, as suggested by Bhattacharya [50]. Nevertheless, when modifying the $Z = 20$ shell gap, this energy difference is nearly the same as $E(1/2^+ - 3/2^+) = -372$ keV. Experimental spectroscopic factors for ^{45}Ar from Gaudefroy [72] and Lu [73] can be compared to shell model calculations with and without a reduction of the $Z = 20$ shell gap. In the work by Gaudefroy, spectroscopic factors for the $d(^{44}\mathrm{Ar}, p)^{45}\mathrm{Ar}$ reaction are used to characterize the evolution of the $N = 28$ shell gap. SDPF-MU calculations without any modifications (referred to as the "reference" calculations) can reproduce observed spectroscopic factors from Gaudefroy, shown in blue in Figure 6.3. The spectroscopic factors reported by Lu from the $p(^{46}\mathrm{Ar}, d)^{45}\mathrm{Ar}$ reaction, values marked red in the figure, also agree with shell model calculations. Experimental lower-level energies, spins, and parities were taken from Bhattacharya [50] and used throughout the analysis. These quantities agree well with predictions from the shell model and show that the SDPF-MU interaction sufficiently tracks the evolution of the $N = 28$ shell gap towards the second island of inversion. Also, the minor changes in the low energy observables highlight that they are not affected by a change in the $Z = 20$ shell gap, thereby having little contributions from the proton fp orbitals, further underscoring the need for β-decay measurements to probe the higher lying states created through the excitation of protons into the fp shell.

While the reduction of the $Z = 20$ shell gap is thoroughly tested in this work and with the results presented above, it can also be important to compare how observables change when modifying the N=28 shell gap. As shown in the right of Figure 6.3, changes to the N=28 shell gap significantly affect the location of excited states in ^{45}Ar and can change the spectroscopic values for states. One can also observe the effects of changing the $N = 28$ shell gap on the β-decay strength distribution. Figure 6.4 shows the comparison of the experimental S_β with the SDPF-MU calculations of the reference interaction, reduced $Z = 20$ interaction, and the newly calculated reduced and increased $N = 28$ interactions. While there is a noticeable but small change to the strength at high excitation energies, the most significant changes to the distribution occur at low energies, as shown in the lower portion of the figure. The interaction with a reduced $N = 28$ shell gap forces the decay strength to much lower

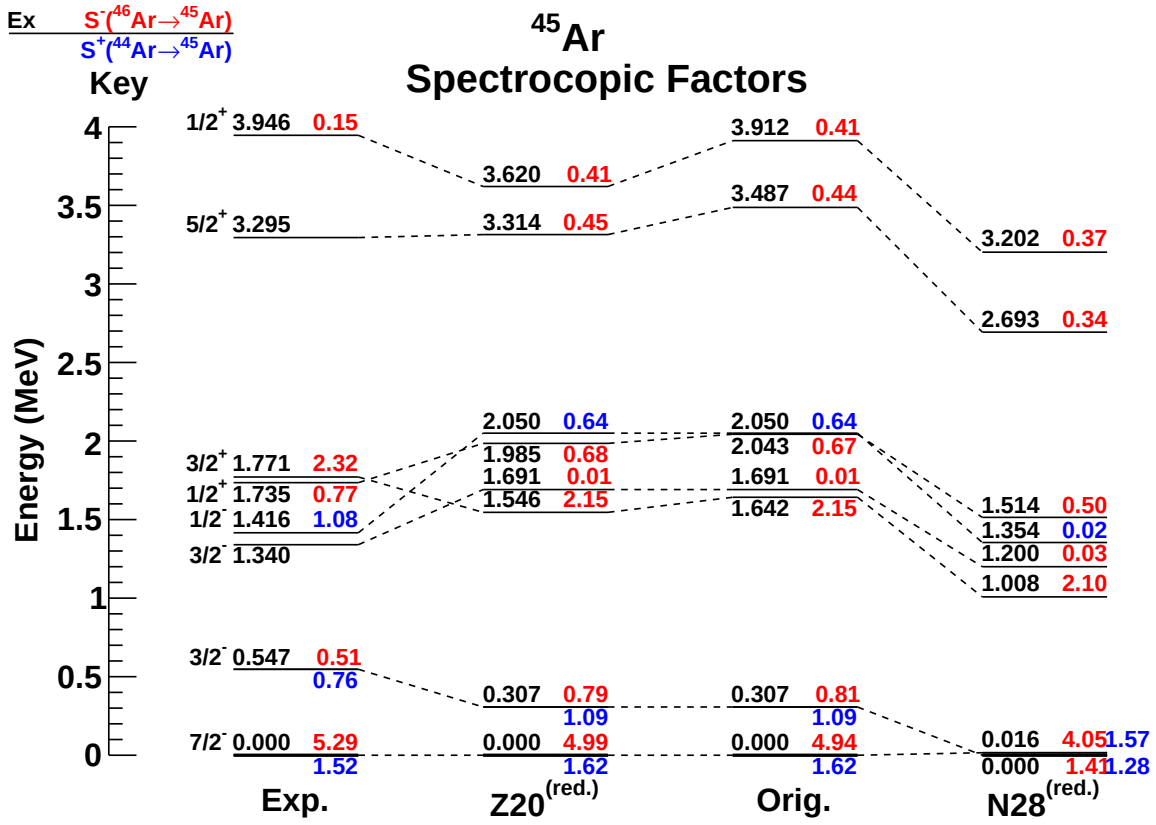

Figure 6.3: A comparison of experimental spectroscopic factors from Refs. [72, 73] compared to reference and modified SDPF-MU predictions. The change in spectroscopic factors between the reference and reduced $Z = 20$ interactions is negligible compared to the effect of reducing the $N = 28$ shell gap.

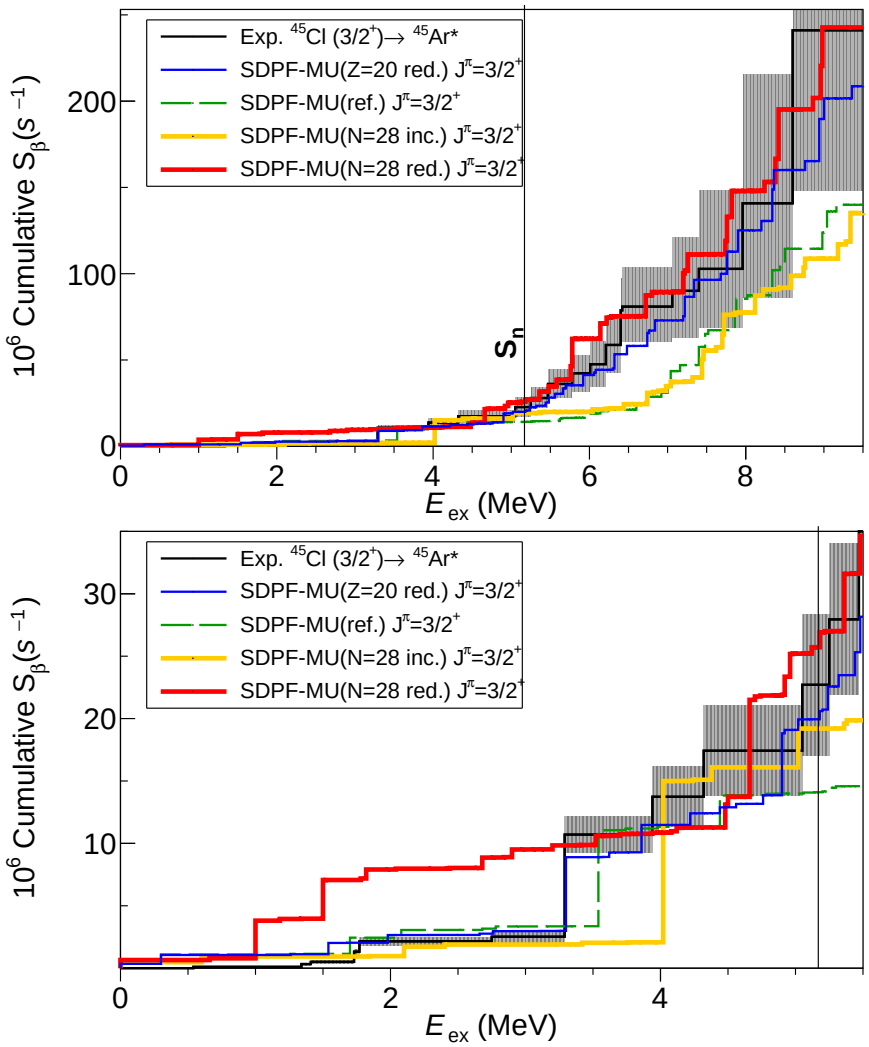

Figure 6.4: Comparing the effect on the cumulative S_β distribution for ^{45}Cl due to the modification of the $N = 28$ shell gap in the SDPF-MU interaction. The red (yellow) curve represents the reduced (increased) $N = 28$ modified SDPF-MU predictions.

excitation energies. In contrast, the increased $N = 28$ shell gap interaction keeps the strength small at low energies, then sharply increases above 4 MeV, neither of which represents the experimental data. In turn, the agreement between the reference SDPF-MU predictions and the experimental S_β exemplifies the accuracy with which the SDPF-MU interaction captures the evolution of the $N = 28$ shell gap halfway towards the island of inversion.

6.3 β Decay Predictions for $N > 28$ Chlorine Isotopes

The β-decay of ^{46}Cl can be complicated due to the odd-odd nature between protons and neutrons which creates multiple different starting points for transitions. With an unpaired proton occupying the $d_{3/2}$ orbital and an unpaired neutron in the $p_{3/2}$ orbital, it is expected that the ground state for ^{47}Cl will be either $0^-, 1^-, 2^-$, or 3^-. This creates a wide variety of different states that can be populated via either FF or GT transitions, but selection rules force FF transitions to populate positive parity states, such as those previously measured at lower energies, while GT transitions must populate negative parity states. Resultantly, as with lighter chlorine isotopes, the GT transitions feed high-lying states in ^{46}Ar. While previous measurements have focused on assessing the first 2^+ state in ^{46}Ar, only Riley investigates a negative parity state [81]. This state, observed at 4982 keV and postulated to have $J^\pi = 3^-$, can become important for constraining the ground state of ^{46}Cl. Looking back at the β-decay feeding for ^{46}Cl, this work measured the feeding intensity to the 3^- state to be 5.7(25)%. Due to GT selection rules, this would imply that the ground state of ^{46}Cl is either 2^- or 3^-.

Furthermore, the β-decay strength distributions can also provide insight into the ground state of ^{46}Cl, along with the shell structure impacted by the decay. In the top of Figure 6.5, the decay strength to low-lying states can be seen, where there is a slight experimental strength to the 2^+ state at 1552 keV. This state can be easily populated from a $1^-, 2^-$, or 3^- ground state through a FF transition, where the theoretical strengths, predicted by the SDPF-MU interaction, all reproduce some strength. The 2^- produces the largest amount of strength, and is in the best agreement with the experimental distribution. Continuing above 5 MeV, the strength distribution predictions for the 1^- and 2^- ground states begin to diverge, slightly, from the other calculations and the experimental distribution, where the blue and green curves step above the others. This discrepancy is short-lived, with the experimental distribution catching up by 8 MeV, and eventually growing larger than all predictions near 10 MeV. While these discrepancies can hold clues into the evolution of shell structure, the inability to determine the ground state for ^{46}Cl forces in-conclusions for how the orbitals transform. Overall, the SDPF-MU interaction does well to reproduce the energy and strength to the first excited state, but as GT transitions become more prominent, slight

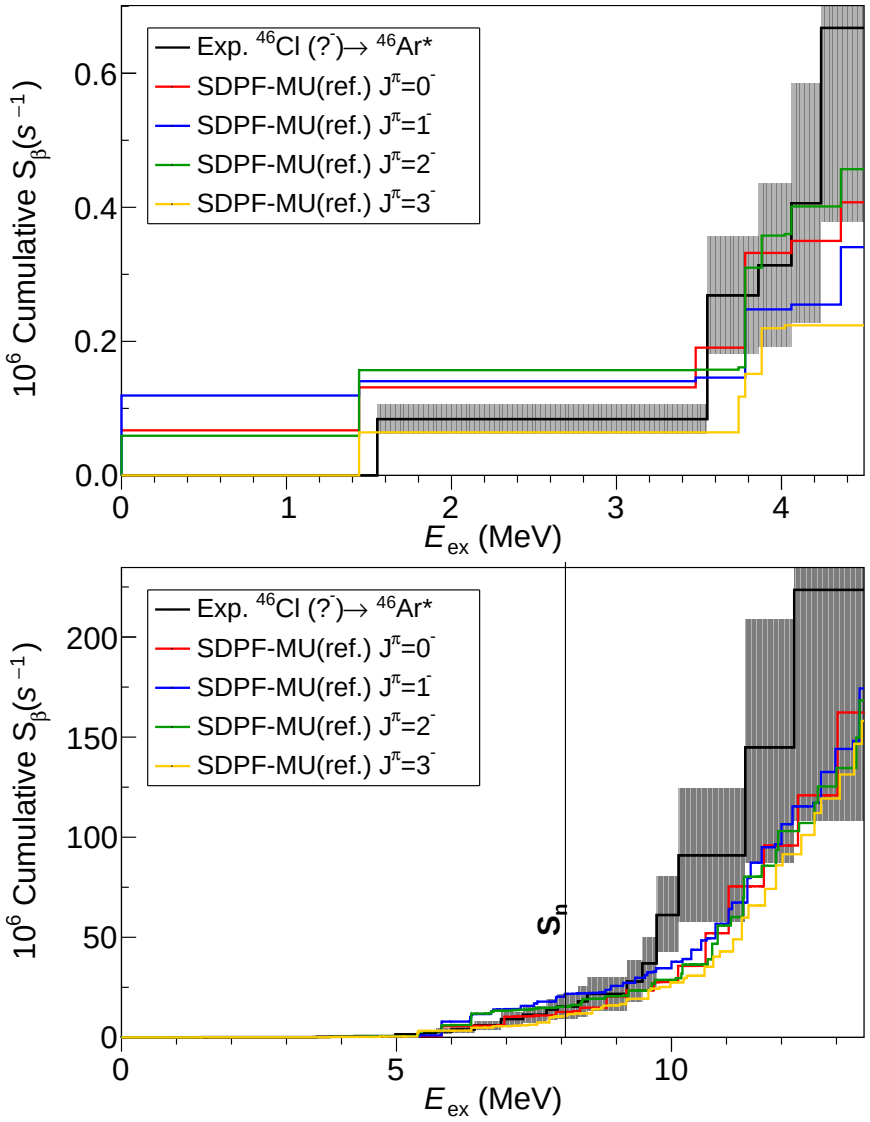

Figure 6.5: Comparing the experimental cumulative S_β distribution for ^{46}Cl (black) with predictions from the SDPF-MU interaction using different possible ground states ^{46}Cl.

discrepancies occur, forcing the need for a higher statistics measurement to better probe the theoretical model.

The decay of ^{47}Cl might be thought to be similar to the decay of ^{45}Cl due to the likely, $3/2^+$ ground state and odd-even nature, but instead, it behaves more like its $N > 28$ neighbor ^{46}Cl, such that both distributions do not have a distinct low-energy feeding. Instead, both distributions have a gradual slope at low energies followed by a steeper portion at higher energies. Nevertheless, the experimental distribution agrees better with the $3/2^+$ ground state decay calculations from both the SDPF-MU and SD-PF-SDG interactions than those

using a $1/2^+$ ground state, as shown in Figure 6.6. The agreement is most notable in the 4-5 MeV range, where the $1/2^+$ ground state yields a step in the region, which is not seen experimentally. Instead, the $3/2^+$ decay produces a cumulative strength distribution with smaller steps and a more gradual increase when pushing to higher excitation energies. At higher energies, the cumulative strength is slightly larger than predicted from the decay of the $3/2^+$ ground state and somewhat agrees better with the $1/2^+$ ground state decay, but both are within error from this measurement.

With the firm establishment of a $3/2^+$ ground state for ^{45}Cl, the competition between the $1/2^+$ and $3/2^+$ states for the ground state of ^{47}Cl is expected to wane due to an increase in separation between the $d_{3/2}$ and $s_{1/2}$ orbitals when filling the neutron $p_{3/2}$ orbitals in the $N > 28$ region, depicted earlier in Figure 2.3. This measurement agrees with the extrapolation of a $3/2^+$ ground state, but the relative difference between the $3/2^+$ and $1/2^+$ low-lying states in ^{47}Cl is not accessible in this measurement.Due to the limited statistics and likely interference from two neutron emission, a future, high statistics, re-measurement is needed to investigate the fine details of the strength distribution, especially at high excitation energies in ^{47}Ar.

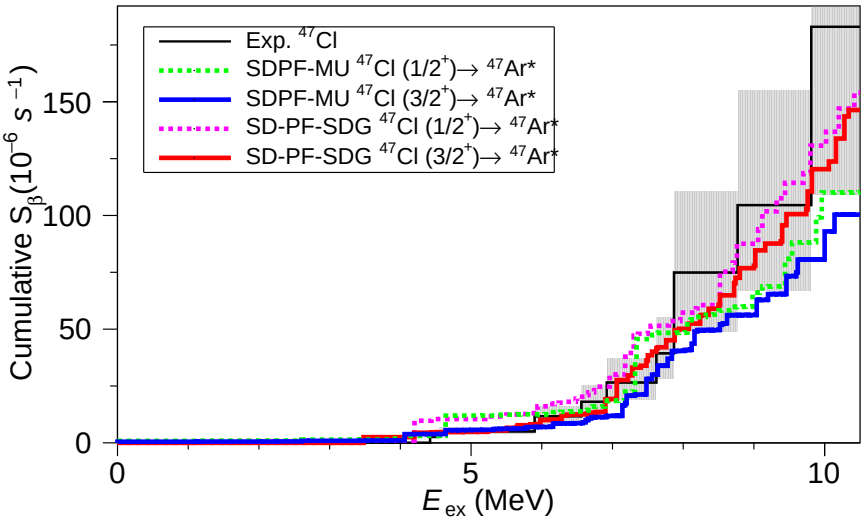

Figure 6.6: The cumulative S_β for the decay of ^{47}Cl, with the experimental measurement, shown as the black curve, compared to theoretical predictions using both $1/2^+$ and $3/2^+$ ground states, shown by the dashed and solid lines respectively. Predictions are shown from both the SDPF-MU, dashed green and solid blue lines, and SD-PD-SDG, dashed pink and solid red lines, interactions.

Chapter 7

Conclusion

The advancement of rare isotope beam facilities, such as the Facility for Rare Isotope Beams (FRIB), has enabled complex and detailed measurements of exotic nuclei to be made already at the early stages of this facility. This was achieved by the use of the FRIB Decay Station Initiator (FDSi) and its two-focal plane detection system, which was used to investigate neutron-rich nuclei in early FRIB experiments. This work focuses on complete decay spectroscopy measurements of Chlorine isotopes near $N = 28$, where high-resolution γ-ray and neutron detection were combined with total absorption spectroscopy to measure the β decay feeding patterns across wide excitation-energy ranges in respective Q_β windows. This work builds upon the first measurement of its kind in this region, Ref. [123], by studying more nuclei and comparing them with theoretical predictions. The complete decay spectroscopy technique, exemplified by FDSi, can then be implemented to study nuclei further from stability.

Discrete γ-ray spectroscopy in this work was performed with the Decay Germanium Array Initiator (DEGAi), while neutron time-of-flight spectroscopy utilized NEXTi to measure neutron energies and decay feedings to neutron unbound states. In the second focal plane, the Modular Total Absorption Spectrometer (MTAS) measured the complete decay feeding intensities, building upon the measurements in the first focal plane by DEGAi for bound states and NEXTi for neutron unbound states. The complementary two focal plane system proved pivotal, as MTAS measured low energy neutrons below the NEXTi threshold, while

the discrete spectroscopy of NEXTi allowed for necessary constraints when deconvoluting the total absorption spectra.

When compared to large-scale shell model (LSSM) calculations, the experimental strength distributions overall agree well, with caveats. Notably, a large step in the strength distribution for the decay of ^{44}Cl, corresponding to feeding to a state near 4.8 MeV, is not well reproduced by theoretical predictions. The calculations instead predict lower strength to a similar state, which also has a slightly lower energy. A larger disagreement is found in the decay of ^{45}Cl, where a reduced $Z = 20$ shell gap is needed to reproduce the experimental strength distribution, especially at neutron unbound excitations.

Transitioning to more exotic decays, lower statistics limited the ability to confidently distinguish between the decays of different predictions for the ground state of ^{46}Cl. On the other hand, the predicted ground state of $3/2^+$ for ^{47}Cl yields predictions that agree with experimental strength distribution, while the $1/2^+$ ground state predictions disagree. Although the statistics are limited, both of these nuclei indicate how remeasuring them with high statistics would be beneficial. First, in the decay of ^{46}Cl there are indications of neutron-γ competition, where high-lying, neutron unbound, states appear to cascade through the 1552 keV 2^+ state. This would be a remarkable result, as neutron-γ competition has not been predicted for this region. Still to confirm this a high statistics measurement would need to be run, with an extensive amount of statistics in both the first and second focal planes. A measurement of this kind would also likely be able to determine the ground state of ^{46}Cl which is currently unknown. Secondly, ^{47}Cl is a strong neutron emitter, with a high probability of two-neutron emission. The neutron spectra of two neutron emitters are known to be highly dependent on the level density of both the first and second emitters [124], thus high lying levels in both ^{47}Ar and ^{46}Ar can be studied in a single decay measurement while probing our current understanding of two neutron emission.

Overall, this work proves the ability to utilize both focal planes of FDSi for a complete spectroscopy measurement. Through similar implementations, nuclei all over the neutron-rich side of the chart of nuclides can be extensively studied, pushing the knowledge of decay to the limits of nuclear stability. In the transition to heavier or more neutron-rich nuclei, it will be beneficial to include new detector technologies, such as OGS [125, 126] and NEXT [127,

128, 129] neutron detectors, for higher resolution neutron energies along with low thresholds and pulse shape discrimination capabilities. This will greatly help reduce of background when measuring β-delayed neutron emission, especially when accompanied by next-generation γ-ray detectors for neutron-γ coincidence.

Bibliography

[1] FRIB, *Frib decay station initiator*, https://fds.ornl.gov/initiator/ (2022), accessed on 10-6-2023. 2

[2] M. Karny, K. Rykaczewski, A. Fijałkowska, B. Rasco, M. Wolińska-Cichocka, R. Grzywacz, K. Goetz, D. Miller, and E. Zganjar, Nuclear Instruments and Methods in Physics Research Section A: Accelerators, Spectrometers, Detectors and Associated Equipment **836**, 83 (2016), ISSN 0168-9002, URL https://www.sciencedirect.com/science/article/pii/S0168900216308646. 2, 33

[3] W. M. Elsasser, Journal de Physique et le Radium **5**, 389 (1934). 3

[4] W. M. Elsasser, Journal de Physique et le Radium **5**, 635 (1934). 3

[5] D. J. Rowe and J. L. Wood, *Fundamentals of Nuclear Models* (World Scientific, 2010), ISBN 978-981-256-956-1. 3

[6] T. Otsuka, A. Gade, O. Sorlin, T. Suzuki, and Y. Utsuno, Rev. Mod. Phys. **92**, 015002 (2020), URL https://link.aps.org/doi/10.1103/RevModPhys.92.015002. 3, 14

[7] M. G. Mayer, Phys. Rev. **75**, 1969 (1949), URL https://link.aps.org/doi/10.1103/PhysRev.75.1969. 3

[8] O. Haxel, J. H. D. Jensen, and H. E. Suess, Phys. Rev. **75**, 1766 (1949), URL https://link.aps.org/doi/10.1103/PhysRev.75.1766.2. 3

[9] J. Chen, Nucl. Data Sheets **179** (2022). 3

[10] A. N. Bohr and B. R. Mottelson, Mat Fys Medd Ban Vid Selsk **27**, 1 (1953), URL https://cds.cern.ch/record/213298/files/p1.pdf. 4, 7

[11] S. G. Nilsson, Mat Fys Medd Ban Vid Selsk **29**, 1 (1955), URL https://cds.cern.ch/record/212345?ln=en. 4, 5

[12] D. T. Tran, H. J. Ong, G. Hagen, T. D. Morris, N. Aoi, T. Suzuki, Y. Kanada-En'yo, L. S. Geng, S. Terashima, I. Tanihata, et al., Nature Communications **9**, 1594 (2018). 5

[13] P. Baumann, A. Huck, G. Klotz, A. Knipper, G. Walter, G. Marguier, H. Ravn, C. Richard-Serre, A. Poves, and J. Retamosa, Physics Letters B **228**, 458 (1989), ISSN 0370-2693, URL https://www.sciencedirect.com/science/article/pii/037026938990974X. 5

[14] A. Ozawa, T. Kobayashi, T. Suzuki, K. Yoshida, and I. Tanihata, Phys. Rev. Lett. **84**, 5493 (2000), URL https://link.aps.org/doi/10.1103/PhysRevLett.84.5493. 5

[15] P. Möller, A. Sierk, T. Ichikawa, and H. Sagawa, Atomic Data and Nuclear Data Tables **109-110**, 1 (2016), ISSN 0092-640X, URL https://www.sciencedirect.com/science/article/pii/S0092640X1600005X. ix, 5, 6, 14

[16] D. Cline, T. Czosnyka, A. Hayes, P. Napiorkowski, N. Warr, and C. Wu, *GOSIA USER MANUAL FOR SIMULATION AND ANALYSIS OF COULOMB EXCITATION EXPERIMENTS* (2012). 7

[17] J. Srebrny, T. Czosnyka, C. Droste, S. Rohoziński, L. Próchniak, K. Zając, K. Pomorski, D. Cline, C. Wu, A. Bäcklin, et al., Nuclear Physics A **766**, 25 (2006), ISSN 0375-9474, URL https://www.sciencedirect.com/science/article/pii/S0375947405012029. 7

[18] E. Rutherford, The London, Edinburgh, and Dublin Philosophical Magazine and Journal of Science **47**, 109 (1899), URL https://api.semanticscholar.org/CorpusID:124589655. 7

[19] E. Fermi, Zeitschrift für Physik **88**, 161 (1934). 7, 10

[20] V. Zelevinsky and A. Volya, *Physics of Atomic Nuclei* (Wiley-VCH, Weinheim, Germany, 2017). 7, 9

[21] E. C. Simpson, *Colourful nuclide chart*, `https://people.physics.anu.edu.au/~ecs103/chart/` (2023), accessed: 2024-5-10. ix, 8

[22] J. Suhonen, *From Nucleons to Nucleus* (Springer Berlin, Heidelberg, 2007), ISBN 978-3-540-48859-0. 9, 10

[23] C. Duke, P. Hansen, O. Nielsen, and G. Rudstam, Nuclear Physics A **151**, 609 (1970), ISSN 0375-9474, URL `http://www.sciencedirect.com/science/article/pii/0375947470904008`. 10

[24] I. Borzov, Nuclear Physics A **777**, 645 (2006), ISSN 0375-9474, special Issue on Nuclear Astrophysics, URL `https://www.sciencedirect.com/science/article/pii/S0375947405008511`. 10

[25] T. Kawano, P. Möller, and W. B. Wilson, Phys. Rev. C **78**, 054601 (2008), URL `https://link.aps.org/doi/10.1103/PhysRevC.78.054601`. 11

[26] F. Sarazin, H. Savajols, W. Mittig, F. Nowacki, N. A. Orr, Z. Ren, P. Roussel-Chomaz, G. Auger, D. Baiborodin, A. V. Belozyorov, et al., Phys. Rev. Lett. **84**, 5062 (2000), URL `https://link.aps.org/doi/10.1103/PhysRevLett.84.5062`. 13, 15

[27] Y. Utsuno, T. Otsuka, B. A. Brown, M. Honma, T. Mizusaki, and N. Shimizu, Phys. Rev. C **86**, 051301(R) (2012), URL `https://link.aps.org/doi/10.1103/PhysRevC.86.051301`. 14, 15, 16, 20

[28] S. Yoshida, Y. Utsuno, N. Shimizu, and T. Otsuka, Phys. Rev. C **97**, 054321 (2018), URL `https://link.aps.org/doi/10.1103/PhysRevC.97.054321`. xv, 14, 80, 83

[29] C. Thibault, R. Klapisch, C. Rigaud, A. M. Poskanzer, R. Prieels, L. Lessard, and W. Reisdorf, Phys. Rev. C **12**, 644 (1975), URL `https://link.aps.org/doi/10.1103/PhysRevC.12.644`. 15

[30] C. Détraz, D. Guillemaud, G. Huber, R. Klapisch, M. Langevin, F. Naulin, C. Thibault, L. C. Carraz, and F. Touchard, Phys. Rev. C **19**, 164 (1979), URL https://link.aps.org/doi/10.1103/PhysRevC.19.164. 15

[31] A. Watt, R. P. Singhal, M. H. Storm, and R. R. Whitehead, Journal of Physics G: Nuclear Physics **7**, L145 (1981), URL https://dx.doi.org/10.1088/0305-4616/7/7/004. 15

[32] A. Poves and J. Retamosa, Physics Letters B **184**, 311 (1987), ISSN 0370-2693, URL https://www.sciencedirect.com/science/article/pii/0370269387901717. 15

[33] E. K. Warburton, J. A. Becker, and B. A. Brown, Phys. Rev. C **41**, 1147 (1990), URL https://link.aps.org/doi/10.1103/PhysRevC.41.1147. 15

[34] B. V. Pritychenko, T. Glasmacher, B. A. Brown, P. D. Cottle, R. W. Ibbotson, K. W. Kemper, L. A. Riley, and H. Scheit, Phys. Rev. C **63**, 011305(R) (2000), URL https://link.aps.org/doi/10.1103/PhysRevC.63.011305. 15

[35] M. Belleguic, F. Azaiez, Z. Dombrádi, D. Sohler, M. J. Lopez-Jimenez, T. Otsuka, M. G. Saint-Laurent, O. Sorlin, M. Stanoiu, Y. Utsuno, et al., Phys. Rev. C **72**, 054316 (2005), URL https://link.aps.org/doi/10.1103/PhysRevC.72.054316. 15

[36] A. Chaudhuri, C. Andreoiu, T. Brunner, U. Chowdhury, S. Ettenauer, A. T. Gallant, G. Gwinner, A. A. Kwiatkowski, A. Lennarz, D. Lunney, et al., Phys. Rev. C **88**, 054317 (2013), URL https://link.aps.org/doi/10.1103/PhysRevC.88.054317. 15

[37] L. Gaudefroy, O. Sorlin, D. Beaumel, Y. Blumenfeld, Z. Dombrádi, S. Fortier, S. Franchoo, M. Gélin, J. Gibelin, S. Grévy, et al., Phys. Rev. Lett. **97**, 092501 (2006), URL https://link.aps.org/doi/10.1103/PhysRevLett.97.092501. 15, 23, 24

[38] B. Bastin, S. Grévy, D. Sohler, O. Sorlin, Z. Dombrádi, N. L. Achouri, J. C. Angélique, F. Azaiez, D. Baiborodin, R. Borcea, et al., Phys. Rev. Lett. **99**, 022503 (2007), URL https://link.aps.org/doi/10.1103/PhysRevLett.99.022503. 15

[39] T. Otsuka, T. Suzuki, M. Honma, Y. Utsuno, N. Tsunoda, K. Tsukiyama, and M. Hjorth-Jensen, Phys. Rev. Lett. **104**, 012501 (2010), URL https://link.aps.org/doi/10.1103/PhysRevLett.104.012501. 15

[40] P.-G. Reinhard and E. Otten, Nuclear Physics A **420**, 173 (1984), ISSN 0375-9474, URL https://www.sciencedirect.com/science/article/pii/0375947484904378. 15

[41] J. L. Yntema and G. R. Satchler, Phys. Rev. **134**, B976 (1964), URL https://link.aps.org/doi/10.1103/PhysRev.134.B976. 17

[42] R. Bansal and J. French, Physics Letters **11**, 145 (1964), ISSN 0031-9163, URL https://www.sciencedirect.com/science/article/pii/0031916364906481. 17

[43] P. Doll, G. Wagner, K. Knöpfle, and G. Mairle, Nuclear Physics A **263**, 210 (1976), ISSN 0375-9474, URL https://www.sciencedirect.com/science/article/pii/037594747690169X. 17

[44] J. L. Yntema, Phys. Rev. C **4**, 1621 (1971), URL https://link.aps.org/doi/10.1103/PhysRevC.4.1621. 17

[45] F. Pellegrini, Phys. Rev. C **19**, 2412 (1979), URL https://link.aps.org/doi/10.1103/PhysRevC.19.2412. 17

[46] T. Otsuka, T. Suzuki, R. Fujimoto, H. Grawe, and Y. Akaishi, Phys. Rev. Lett. **95**, 232502 (2005), URL https://link.aps.org/doi/10.1103/PhysRevLett.95.232502. 17

[47] T. Otsuka, R. Fujimoto, Y. Utsuno, B. A. Brown, M. Honma, and T. Mizusaki, Phys. Rev. Lett. **87**, 082502 (2001), URL https://link.aps.org/doi/10.1103/PhysRevLett.87.082502. 17

[48] J. Papuga, M. L. Bissell, K. Kreim, K. Blaum, B. A. Brown, M. De Rydt, R. F. Garcia Ruiz, H. Heylen, M. Kowalska, R. Neugart, et al., Phys. Rev. Lett. **110**, 172503 (2013), URL https://link.aps.org/doi/10.1103/PhysRevLett.110.172503. 17

[49] J. Papuga, M. L. Bissell, K. Kreim, C. Barbieri, K. Blaum, M. De Rydt, T. Duguet, R. F. Garcia Ruiz, H. Heylen, M. Kowalska, et al., Phys. Rev. C **90**, 034321 (2014), URL https://link.aps.org/doi/10.1103/PhysRevC.90.034321. 17

[50] S. Bhattacharya, V. Tripathi, S. L. Tabor, A. Volya, P. C. Bender, C. Benetti, M. P. Carpenter, J. J. Carroll, A. Chester, C. J. Chiara, et al., Phys. Rev. C **108**, 024312 (2023), URL https://link.aps.org/doi/10.1103/PhysRevC.108.024312. 19, 23, 57, 59, 82, 85

[51] A. Gade, B. A. Brown, D. Bazin, C. M. Campbell, J. A. Church, D. C. Dinca, J. Enders, T. Glasmacher, M. Horoi, Z. Hu, et al., Phys. Rev. C **74**, 034322 (2006), URL https://link.aps.org/doi/10.1103/PhysRevC.74.034322. 19, 85

[52] D. F. Measday and T. J. Stocki, Phys. Rev. C **73**, 045501 (2006), URL https://link.aps.org/doi/10.1103/PhysRevC.73.045501. 19

[53] A. Huck, G. Klotz, A. Knipper, C. Miehé, G. Walter, and C. Richard-Serre, Phys. Rev. C **21**, 712 (1980), URL https://link.aps.org/doi/10.1103/PhysRevC.21.712. 19

[54] L. Weissman, O. Arnd, U. Bergmann, A. Brown, R. Catherall, J. Cederkall, I. Dillmann, O. Hallmann, L. Fraile, S. Franchoo, et al., Phys. Rev. C **70**, 024304 (2004), URL https://link.aps.org/doi/10.1103/PhysRevC.70.024304. 19

[55] R. Broda, J. Wrzesiński, A. Gadea, N. Mărginean, B. Fornal, L. Corradi, A. M. Stefanini, W. Królas, T. Pawłat, B. Szpak, et al., Phys. Rev. C **82**, 034319 (2010), URL https://link.aps.org/doi/10.1103/PhysRevC.82.034319. 19

[56] e. a. Sun, Y.L., Physics Letters B **802**, 135215 (2020), ISSN 0370-2693, URL https://www.sciencedirect.com/science/article/pii/S0370269320300198. 19

[57] B. D. Linh, A. Corsi, A. Gillibert, A. Obertelli, P. Doornenbal, C. Barbieri, S. Chen, L. X. Chung, T. Duguet, M. Gómez-Ramos, et al., Phys. Rev. C **104**, 044331 (2021), URL https://link.aps.org/doi/10.1103/PhysRevC.104.044331. 19

[58] X. Liang, R. Chapman, F. Haas, K.-M. Spohr, P. Bednarczyk, S. Campbell, P. Dagnall, M. Davison, G. de Angelis, G. Duchêne, et al., Phys. Rev. C **66**, 037301 (2002), URL https://link.aps.org/doi/10.1103/PhysRevC.66.037301. 19

[59] O. Sorlin, Z. Dombrádi, D. Sohler, F. Azaiez, J. Timár, Y. E. Penionzhkevich, F. Amorini, D. Baiborodin, A. Bauchet, F. Becker, et al., Eur. Phys. J. A **22**, 173 (2004). 19

[60] J. Ollier, R. Chapman, X. Liang, M. Labiche, K.-M. Spohr, M. Davison, G. de Angelis, M. Axiotis, T. Kröll, D. R. Napoli, et al., Phys. Rev. C **67**, 024302 (2003), URL https://link.aps.org/doi/10.1103/PhysRevC.67.024302. 19

[61] S. Szilner, L. Corradi, F. Haas, G. Pollarolo, L. Angus, S. Beghini, M. Bouhelal, R. Chapman, E. Caurier, S. Courtin, et al., Phys. Rev. C **87**, 054322 (2013), URL https://link.aps.org/doi/10.1103/PhysRevC.87.054322. 19

[62] J. A. Winger, H. H. Yousif, W. C. Ma, V. Ravikumar, W. Lui, S. K. Phillips, R. B. Piercey, P. F. Mantica, B. Pritychenko, R. M. Ronningen, et al., AIP Conference Proceedings **455**, 606 (1998), ISSN 0094-243X, URL https://doi.org/10.1063/1.57265. 19, 53, 59

[63] B. A. Brown and B. H. Wildenthal, Annu. Rev. Nucl. Part. Sci. **38**, 29 (1988). 20

[64] M. Honma, T. Otsuka, and T. Mizusaki, RIKEN Accel. Prog. Rep. **41**, 32 (2008). 20

[65] O. Sorlin, D. Guillemaud-Mueller, A. C. Mueller, V. Borrel, S. Dogny, F. Pougheon, K.-L. Kratz, H. Gabelmann, B. Pfeiffer, A. Wöhr, et al., Phys. Rev. C **47**, 2941 (1993), URL https://link.aps.org/doi/10.1103/PhysRevC.47.2941. 21

[66] O. Sorlin, D. Guillemaud-Mueller, R. Anne, L. Axelsson, D. Bazin, W. Böhmer, V. Borrel, Y. Jading, H. Keller, K.-L. Kratz, et al., Nuclear Physics A **583**, 763 (1995), ISSN 0375-9474, URL https://www.sciencedirect.com/science/article/pii/037594749400755C. 21, 53, 59, 65, 67

[67] S. Grévy, J. Mrazek, J. Angélique, P. Baumann, C. Borcea, A. Buta, G. Canchel, W. Catford, S. Courtin, J. Daugas, et al., Nuclear Physics A **722**, C424 (2003), ISSN 0375-9474, URL https://www.sciencedirect.com/science/article/pii/S0375947403014015. 21

[68] S. Grévy, J. Angélique, P. Baumann, C. Borcea, A. Buta, G. Canchel, W. Catford, S. Courtin, J. Daugas, F. de Oliveira, et al., Physics Letters B **594**, 252 (2004), ISSN 0370-2693, URL https://www.sciencedirect.com/science/article/pii/S0370269304007981. 21, 67, 73, 75

[69] J. Mrázek, S. Grévy, S. Iulian, A. Buta, F. Negoita, J. Angélique, P. Baumann, C. Borcea, G. Canchel, W. Catford, et al., Nuclear Physics A **734**, E65 (2004), ISSN 0375-9474, proceedings of the Eighth International Conference on Nucleus-Nucleus Collisions (NN2003), URL https://www.sciencedirect.com/science/article/pii/S037594740400257X. 21, 23, 53, 65, 69

[70] Z. Dombrádi, D. Sohler, O. Sorlin, F. Azaiez, F. Nowacki, M. Stanoiu, Y.-E. Penionzhkevich, J. Timár, F. Amorini, D. Baiborodin, et al., Nuclear Physics A **727**, 195 (2003), ISSN 0375-9474, URL https://www.sciencedirect.com/science/article/pii/S0375947403016889. 22, 23

[71] A. Gade, D. Bazin, C. A. Bertulani, B. A. Brown, C. M. Campbell, J. A. Church, D. C. Dinca, J. Enders, T. Glasmacher, P. G. Hansen, et al., Phys. Rev. C **71**, 051301(R) (2005), URL https://link.aps.org/doi/10.1103/PhysRevC.71.051301. 22

[72] L. Gaudefroy, O. Sorlin, F. Nowacki, D. Beaumel, Y. Blumenfeld, Z. Dombrádi, S. Fortier, S. Franchoo, S. Grévy, F. Hammache, et al., Phys. Rev. C **78**, 034307 (2008), URL https://link.aps.org/doi/10.1103/PhysRevC.78.034307. xv, 22, 85, 86

[73] F. Lu, J. Lee, M. B. Tsang, D. Bazin, D. Coupland, V. Henzl, D. Henzlova, M. Kilburn, W. G. Lynch, A. M. Rogers, et al., Phys. Rev. C **88**, 017604 (2013), URL https://link.aps.org/doi/10.1103/PhysRevC.88.017604. xv, 23, 84, 85, 86

[74] W. Mayer, K. E. Rehm, H. J. Körner, W. Mayer, E. Müller, I. Oelrich, H. J. Scheerer, R. E. Segel, P. Sperr, and W. Wagner, Phys. Rev. C **22**, 2449 (1980), URL https://link.aps.org/doi/10.1103/PhysRevC.22.2449. 23

[75] H. Scheit, T. Glasmacher, B. A. Brown, J. A. Brown, P. D. Cottle, P. G. Hansen, R. Harkewicz, M. Hellström, R. W. Ibbotson, J. K. Jewell, et al., Phys. Rev. Lett. **77**, 3967 (1996), URL https://link.aps.org/doi/10.1103/PhysRevLett.77.3967. 23

[76] B. Fornal, R. Broda, W. Królas, T. Pawlat, J. Wrzesiński, D. Bazzacco, S. Lunardi, C. Rossi Alvarez, G. Viesti, G. de Angelis, et al., Eur. Phys. J. A **7**, 147 (2000), URL https://doi.org/epja/v7/p147(epja172). 23

[77] D. Mengoni, J. J. Valiente-Dobón, E. Farnea, A. Gadea, A. Dewald, A. Latina, and the CLARA-PRISMA Collaboration, Eur. Phys. J. A **42**, 387 (2009), URL https://doi.org/10.1140/epja/i2008-10775-2. 23

[78] A. Gade, D. Bazin, C. M. Campbell, J. A. Church, D. C. Dinca, J. Enders, T. Glasmacher, Z. Hu, K. W. Kemper, W. F. Mueller, et al., Phys. Rev. C **68**, 014302 (2003), URL https://link.aps.org/doi/10.1103/PhysRevC.68.014302. 23

[79] S. Calinescu, L. Cáceres, S. Grévy, O. Sorlin, Z. Dombrádi, M. Stanoiu, R. Astabatyan, C. Borcea, R. Borcea, M. Bowry, et al., Phys. Rev. C **93**, 044333 (2016), URL https://link.aps.org/doi/10.1103/PhysRevC.93.044333. 23

[80] D. Mengoni, J. J. Valiente-Dobón, A. Gadea, S. Lunardi, S. M. Lenzi, R. Broda, A. Dewald, T. Pissulla, L. J. Angus, S. Aydin, et al., Phys. Rev. C **82**, 024308 (2010), URL https://link.aps.org/doi/10.1103/PhysRevC.82.024308. 23

[81] L. A. Riley, M. A. Abdelqader, D. Bazin, M. J. Bojazi, B. A. Brown, C. M. Campbell, J. A. Church, P. D. Cottle, D. C. Dinca, J. Enders, et al., Phys. Rev. C **72**, 024311 (2005), URL https://link.aps.org/doi/10.1103/PhysRevC.72.024311. 23, 88

[82] K. Nowak, K. Wimmer, S. Hellgartner, D. Mücher, V. Bildstein, J. Diriken, J. Elseviers, L. P. Gaffney, R. Gernhäuser, J. Iwanicki, et al., Phys. Rev. C **93**, 044335 (2016), URL https://link.aps.org/doi/10.1103/PhysRevC.93.044335. 23, 24

[83] S. Bhattacharyya, M. Rejmund, A. Navin, E. Caurier, F. Nowacki, A. Poves, R. Chapman, D. O'Donnell, M. Gelin, A. Hodsdon, et al., Phys. Rev. Lett. **101**, 032501 (2008), URL https://link.aps.org/doi/10.1103/PhysRevLett.101.032501. 24, 73, 76

[84] R. Winkler, A. Gade, T. Baugher, D. Bazin, B. A. Brown, T. Glasmacher, G. F. Grinyer, R. Meharchand, S. McDaniel, A. Ratkiewicz, et al., Phys. Rev. Lett. **108**, 182501 (2012), URL https://link.aps.org/doi/10.1103/PhysRevLett.108.182501. 24

[85] A. Gade, J. A. Tostevin, V. Bader, T. Baugher, D. Bazin, J. S. Berryman, B. A. Brown, C. A. Diget, T. Glasmacher, D. J. Hartley, et al., Phys. Rev. C **93**, 054315 (2016), URL https://link.aps.org/doi/10.1103/PhysRevC.93.054315. 24, 25, 73

[86] J. Wei, D. Arenius, N. Bultman, F. Casagrande, C. Compton, K. Davidson, J. DeKamp, B. Drewyor, K. Elliott, A. Facco, et al. (2013), URL https://www.osti.gov/biblio/1992484. 27

[87] M. Hausmann, *The facility for rare isotope beams: The latest doe np user facility coming online*, https://indico.physics.lbl.gov/event/1945/attachments/3369/4430/FRIB_LBNLInstrumentationColloq_20220427_M_Hausmann.pdf (2022), date Accessed: May 10, 2024. x, 28

[88] F. Pellemoine, W. Mittig, M. Avilov, D. Ippel, J. Lenz, J. Oliva, I. Silverman, D. Youchison, and T. Xu, Nuclear Instruments and Methods in Physics Research Section A: Accelerators, Spectrometers, Detectors and Associated Equipment **655**, 3 (2011), ISSN 0168-9002, proceedings of the 25th World Conference of the International Nuclear Target Development Society, URL https://www.sciencedirect.com/science/article/pii/S0168900211011211. 27

[89] M. Hausmann, A. Aaron, A. Amthor, M. Avilov, L. Bandura, R. Bennett, G. Bollen, T. Borden, T. Burgess, S. Chouhan, et al., Nuclear Instruments and Methods in Physics Research Section B: Beam Interactions with Materials and Atoms **317**,

349 (2013), ISSN 0168-583X, xVIth International Conference on ElectroMagnetic Isotope Separators and Techniques Related to their Applications, December 27, 2012 at Matsue, Japan, URL https://www.sciencedirect.com/science/article/pii/S0168583X13007210. 27

[90] M. Portillo, M. Hausmann, and S. Chouhan, Nuclear Instruments and Methods in Physics Research Section B: Beam Interactions with Materials and Atoms **376**, 150 (2016), ISSN 0168-583X, proceedings of the XVIIth International Conference on Electromagnetic Isotope Separators and Related Topics (EMIS2015), Grand Rapids, MI, U.S.A., 11-15 May 2015, URL https://www.sciencedirect.com/science/article/pii/S0168583X16000860. 27, 28

[91] N. Fukuda, T. Kubo, T. Ohnishi, N. Inabe, H. Takeda, D. Kameda, and H. Suzuki, Nuclear Instruments and Methods in Physics Research Section B: Beam Interactions with Materials and Atoms **317**, 323 (2013), ISSN 0168-583X, xVIth International Conference on ElectroMagnetic Isotope Separators and Techniques Related to their Applications, December 2?7, 2012 at Matsue, Japan, URL https://www.sciencedirect.com/science/article/pii/S0168583X13009890. 29

[92] Y. Xiao, S. Go, R. Grzywacz, R. Orlandi, A. N. Andreyev, M. Asai, M. A. Bentley, G. de Angelis, C. J. Gross, P. Hausladen, et al., Phys. Rev. C **100**, 034315 (2019), URL https://link.aps.org/doi/10.1103/PhysRevC.100.034315. 30

[93] Advatech, *Yso(ce) - yttrium orthosilicate (ce) scintillator crystal*, https://www.advatech-uk.co.uk/yso_ce.html (2024), accessed: 2024-1-20. 30

[94] R. Yokoyama, M. Singh, R. Grzywacz, A. Keeler, T. King, J. Agramunt, N. Brewer, S. Go, J. Heideman, J. Liu, et al., Nuclear Instruments and Methods in Physics Research Section A: Accelerators, Spectrometers, Detectors and Associated Equipment **937**, 93 (2019), ISSN 0168-9002, URL https://www.sciencedirect.com/science/article/pii/S0168900219306424. 30

[95] Hamamatsu Photonics, *Hamamatsu photon is our business*, https://www.hamamatsu.com/ (2024), accessed: 202341-19. 30, 33

[96] Vertilon, *Vertilon*, https://vertilon.com (2024), accessed: 2024-01-26. 30, 34

[97] Norland Prouducts Inc., *Norland uv curing adhesives*, https://www.norlandprod.com/UVdefault.html (2024), accessed: 2024-1-26. 31

[98] G. F. Knoll, *Radiation Detection and Measurement* (John Wiley & Sons Inc, 2000), ISBN 978-0471073383. 32, 37

[99] B. Crider, C. Prokop, S. Liddick, H. Albers, M. Alshudifat, A. Ayangeakaa, M. Carpenter, J. Carroll, J. Chen, C. Chiara, et al., Nuclear Instruments and Methods in Physics Research Section A: Accelerators, Spectrometers, Detectors and Associated Equipment **1055**, 168525 (2023), ISSN 0168-9002, URL https://www.sciencedirect.com/science/article/pii/S0168900223005156. 32

[100] K. Smith, T. Baugher, S. Burcher, A. Carter, J. Cizewski, K. Chipps, M. Febbraro, R. Grzywacz, K. Jones, S. Munoz, et al., Nuclear Instruments and Methods in Physics Research Section B: Beam Interactions with Materials and Atoms **414**, 190 (2018), ISSN 0168-583X, URL https://www.sciencedirect.com/science/article/pii/S0168583X17307036. 32

[101] S. Paulauskas, M. Madurga, R. Grzywacz, D. Miller, S. Padgett, and H. Tan, Nuclear Instruments and Methods in Physics Research Section A: Accelerators, Spectrometers, Detectors and Associated Equipment **737**, 22 (2014), ISSN 0168-9002, URL https://www.sciencedirect.com/science/article/pii/S0168900213015672. 32

[102] W. Peters, S. Ilyushkin, M. Madurga, C. Matei, S. Paulauskas, R. Grzywacz, D. Bardayan, C. Brune, J. Allen, J. Allen, et al., Nuclear Instruments and Methods in Physics Research Section A: Accelerators, Spectrometers, Detectors and Associated Equipment **836**, 122 (2016), ISSN 0168-9002, URL https://www.sciencedirect.com/science/article/pii/S0168900216308816. 32

[103] Eljen Technology, *General purpose ej-200, ej-204, ej-208, ej-212*, https://eljentechnology.com/products/plastic-scintillators/ej-200-ej-204-ej-208-ej-212 (2024), accessed: 2024-1-19. 32

[104] M. Karny, A. Fijałkowska, R. Grzywacz, B. Rasco, K. Rykaczewski, and M. Stepaniuk, Nuclear Instruments and Methods in Physics Research Section B: Beam Interactions with Materials and Atoms **463**, 390 (2020), ISSN 0168-583X, URL https://www.sciencedirect.com/science/article/pii/S0168583X19302290. 33

[105] Semiconductor Components Industries, LLC, *Silicon photomultipliers (sipm) — array j*, https://www.onsemi.com/products/sensors/photodetectors-sipm-spad/silicon-photomultipliers-sipm/arrayj (2023), accessed: 2023-04-11, URL https://www.onsemi.com/products/sensors/photodetectors-sipm-spad/silicon-photomultipliers-sipm/arrayj. 33

[106] D. Bazin, D. Guerreau, R. Anne, D. Guillemaud-Mueller, A. Mueller, and M. Saint-Laurent, Nuclear Physics A **515**, 349 (1990), ISSN 0375-9474, URL https://www.sciencedirect.com/science/article/pii/037594749090372S. 36

[107] O. Tarasov, D. Bazin, M. Hausmann, M. Kuchera, P. Ostroumov, M. Portillo, B. Sherrill, K. Tarasova, and T. Zhang, Nuclear Instruments and Methods in Physics Research Section B: Beam Interactions with Materials and Atoms **541**, 4 (2023), ISSN 0168-583X, URL https://www.sciencedirect.com/science/article/pii/S0168583X23001775. 37

[108] Y. Koba, H. Iwamoto, K. Kiyohara, T. Nagasaki, G. Wakabayashi, Y. Uozumi, and N. Matsufuji, Progress in NUCLEAR SCIENCE and TECHNOLOGY **1**, 218 (2011). 37

[109] J. F. Ziegler, M. Ziegler, and J. Biersack, Nuclear Instruments and Methods in Physics Research Section B: Beam Interactions with Materials and Atoms **268**, 1818 (2010), ISSN 0168-583X, 19th International Conference on Ion Beam Analysis, URL https://www.sciencedirect.com/science/article/pii/S0168583X10001862. 38

[110] e. a. B. Kreider, to be published. 39

[111] J. Cetnar, Annals of Nuclear Energy **33**, 640 (2006), ISSN 0306-4549, URL https://www.sciencedirect.com/science/article/pii/S0306454906000284. 39

[112] T. J. Gray, J. M. Allmond, Z. Xu, T. T. King, R. S. Lubna, H. L. Crawford, V. Tripathi, B. P. Crider, R. Grzywacz, S. N. Liddick, et al., Phys. Rev. Lett. **130**, 242501 (2023), URL https://link.aps.org/doi/10.1103/PhysRevLett.130.242501. 41

[113] H. L. Crawford, R. V. F. Janssens, P. F. Mantica, J. S. Berryman, R. Broda, M. P. Carpenter, N. Cieplicka, B. Fornal, G. F. Grinyer, N. Hoteling, et al., Phys. Rev. C **82**, 014311 (2010), URL https://link.aps.org/doi/10.1103/PhysRevC.82.014311. 41

[114] C. R. Thornsberry, Phd thesis, University of Tennessee, Knoxville (2018). 42, 47

[115] S. Agostinelli, J. Allison, K. Amako, J. Apostolakis, H. Araujo, P. Arce, M. Asai, D. Axen, S. Banerjee, G. Barrand, et al., Nuclear Instruments and Methods in Physics Research Section A: Accelerators, Spectrometers, Detectors and Associated Equipment **506**, 250 (2003), ISSN 0168-9002, URL https://www.sciencedirect.com/science/article/pii/S0168900203013688. 43, 47

[116] P. Shuai, B. C. Rasco, K. P. Rykaczewski, A. Fijałkowska, M. Karny, M. Wolińska-Cichocka, R. K. Grzywacz, C. J. Gross, D. W. Stracener, E. F. Zganjar, et al., Phys. Rev. C **105**, 054312 (2022), URL https://link.aps.org/doi/10.1103/PhysRevC.105.054312. 45, 46

[117] F. Perrot, F. Maréchal, C. Jollet, P. Dessagne, J.-C. Angélique, G. Ban, P. Baumann, F. Benrachi, U. Bergmann, C. Borcea, et al., Phys. Rev. C **74**, 014313 (2006), URL https://link.aps.org/doi/10.1103/PhysRevC.74.014313. 49

[118] J. Heideman, Phd thesis, University of Tennessee, Knoxville (2021). 50

[119] Z. Y. Xu, M. Madurga, R. Grzywacz, T. T. King, A. Algora, A. N. Andreyev, J. Benito, T. Berry, M. J. G. Borge, C. Costache, et al., Phys. Rev. C **108**, 014314 (2023), URL https://link.aps.org/doi/10.1103/PhysRevC.108.014314. 50

[120] Z. Y. Xu, R. Grzywacz, A. Gottardo, M. Madurga, I. M. Alonso, A. N. Andreyev, G. Benzoni, M. J. G. Borge, T. Cap, C. Costache, et al., Phys. Rev. Lett. **133**, 042501 (2024), URL https://link.aps.org/doi/10.1103/PhysRevLett.133.042501. 50

[121] J. A. Winger, N. p. (2016), URL https://doi.org/10.2172/1248341. 53, 56

[122] M. Wang, W. Huang, F. Kondev, G. Audi, and S. Naimi, Chinese Physics C **45**, 030003 (2021), URL https://doi.org/10.1088/1674-1137/abddaf. 54

[123] I. Cox, Z. Y. Xu, R. Grzywacz, W.-J. Ong, B. C. Rasco, N. Kitamura, D. Hoskins, S. Neupane, T. J. Ruland, J. M. Allmond, et al., Phys. Rev. Lett. **132**, 152503 (2024), URL https://link.aps.org/doi/10.1103/PhysRevLett.132.152503. 65, 91

[124] R. Yokoyama, R. Grzywacz, B. C. Rasco, N. Brewer, K. P. Rykaczewski, I. Dillmann, J. L. Tain, S. Nishimura, D. S. Ahn, A. Algora, et al., Phys. Rev. C **108**, 064307 (2023), URL https://link.aps.org/doi/10.1103/PhysRevC.108.064307. 92

[125] W. K. Warburton, J. S. Carlson, and P. L. Feng, Nuclear Instruments and Methods in Physics Research Section A: Accelerators, Spectrometers, Detectors and Associated Equipment **1018**, 165778 (2021), ISSN 0168-9002, URL https://www.sciencedirect.com/science/article/pii/S0168900221007634. 92

[126] Blueshift Optics, LLC, *Organic glass scintillator*, https://blueshiftoptics.com/org-glass-scintillator (2022), accessed: 2024-8-19. 92

[127] J. Heideman, D. Pérez-Loureiro, R. Grzywacz, C. Thornsberry, J. Chan, L. Heilbronn, S. Neupane, K. Schmitt, M. Rajabali, A. Engelhardt, et al., Nuclear Instruments and Methods in Physics Research Section A: Accelerators, Spectrometers, Detectors and Associated Equipment **946**, 162528 (2019), ISSN 0168-9002, URL https://www.sciencedirect.com/science/article/pii/S0168900219310617. 92

[128] S. Neupane, J. Heideman, R. Grzywacz, J. Hooker, K. Jones, N. Kitamura, C. Thornsberry, L. Heilbronn, M. Rajabali, Y. Alberty-Jones, et al., Nuclear Instruments and Methods in Physics Research Section A: Accelerators, Spectrometers, Detectors and Associated Equipment **1020**, 165881 (2021), ISSN 0168-9002, URL https://www.sciencedirect.com/science/article/pii/S0168900221008640. 93

[129] S. Neupane, J. Heideman, R. Grzywacz, M. Cooper, J. Hooker, K. L. Jones, T. T. King, N. Kitamura, M. Madurga, K. Siegl, et al., Phys. Rev. C **106**, 044320 (2022), URL https://link.aps.org/doi/10.1103/PhysRevC.106.044320. 93

Vita

Ian Cox was March 1998 in Jonesboro, Tennessee. Throughout his childhood, Ian was always playing sports from baseball in the summer to football in the fall followed by basketball in the winter. With an aptitude for high-school mathematics and calculus, physics became a natural choice for a college major at the University of Tennessee, Knoxville, where his skills could be applied towards a Bachelor of Science degree. Ian participated in an internship at his grandfather's business working with radioactive sources which led to his love of nuclear physics followed by his graduate studies in the experimental low-energy nuclear physics group led by Dr. Robert Grzywacz at the University of Tennessee, Knoxville.

While working towards his Doctoral degree, Ian traveled all of the world for experiments, conferences, and leisure. After an overseas engagement in 2022, Ian married Delaney in July of 2023. As a family, they have enjoyed numerous trips together, while also exploiting the outstanding athletic programs in Knoxville to enjoy their weekends.